MAGNETOELECTRIC EFFECTS IN MANGANITES

By

HYOUNG JEEN JEEN

A DISSERTATION PRESENTED TO THE GRADUATE SCHOOL
OF THE UNIVERSITY OF FLORIDA IN PARTIAL FULFILLMENT
OF THE REQUIREMENTS FOR THE DEGREE OF
DOCTOR OF PHILOSOPHY

UNIVERSITY OF FLORIDA

2011

© 2011 Hyoung Jeen Jeen

To my family

ACKNOWLEDGMENTS

After I started my graduate school in University of Florida (UF), I have a lot of chances to get helps and advices from many people. I feel like I have lots of debts from UF. I think the best way to pay back these helps is to spread my knowledge and idea to anybody, who wants to learn.

I greatly appreciated my advisor, Dr. Amlan Biswas. He is the advisor not only for my research but also for my life. I also appreciated to committee members: Dr. Arthur F. Hebard, Dr. Alan Dorsey, Dr. Yoonseok Lee, and Dr. David Norton. Dr. Hebard always encourages me to work creatively in manganite research. He is willing to answer all my questions and sometimes gave me some questions for me to answers. Dr. Alan Dorsey is willing to keep himself as committee member. He is always eager to discuss with me, even if his schedule is busy. Dr. Yoonseok Lee is the mentor, even if he was not my degree committee before 2008. He has clearly answered to all my questions on any topic. He sometimes does not hesitate to point out my bad habits/attitudes, so I can fix those. Dr. David Norton's encouragement, especially in a professional conference, made me confident.

I appreciated my former committee members: Dr. Hagen, Dr. Long, and Dr. Petkova. I am grateful to staffs in Physics department: Darelene for all the paper works and advices, Greg and John for constant supply of Liquid Helium, Charles and Bob for great help in lab teaching, Tim for well maintaining our New Physics Building, Marc for machine shop work, and Pam for all the paper works. I also thanks to Laurie, Billie, and Janet. I also thanks to my lab mates, basement friends, all other friends I met in Gainesville. I thank you to staffs (Dr. Craciun, Dr. Bourne, Dr. Siebein, and Bill Lewis) in major analytical instrumentation center and nanoscience institute for medical and engineering technology, UF. I also appreciated to Dr. Sang-Wook Cheong (Rutgers) and Dr. Ho-Nyung Lee (Oak Ridge National Lab) about their advices on managnite research.

Among my college professors, I specially thank to Dr. Kyung-Soo Yi, Dr. Yunchul Chung, Dr. Ho-Soon Yang, and Dr. Jai-Seok Ahn to their constant advices.

This research has been supported from NSF DMR-0804452. I am also grateful for graduate study abroad program from Korean science and engineering foundation (KRF-2005-215-C00043) and graduate student council travel grants and college of liberal arts and sciences and physics department travel awards.

TABLE OF CONTENTS

page

ACKNOWLEDGMENTS 4

LIST OF TABLES 8

LIST OF FIGURES 9

ABSTRACT 11

CHAPTER

1 INTRODUCTION 13

1.1 General Introduction 13
1.2 Magnetoelectric Effects 14
1.3 Basics of Manganites 15
1.3.1 Structure of Manganites 15
1.3.2 Electronic Configuration of Mn Ions 16
1.4 Hole Doped manganites 18
1.4.1 Transport Mechanism in Mixed Valence Manganites. 18
1.4.2 Phase Coexistence in Hole Doped Manganites and (La, Pr, Ca)MnO_3 (LPCMO) 19
1.5 Multiferroism and $BiMnO_3$ (BMO) 21

2 EXPERIMENTAL METHODS 24

2.1 Thin Film Growth 24
2.1.1 Substrate Surface Treatment 24
2.1.2 Pulsed Laser Deposition 25
2.2 Transport Measurements 27
2.2.1 Constant Current Sourced Measurements 27
2.2.2 Constant Voltage Sourced Measurements 29
2.3 Magnetization Measurements 30
2.4 Surface and Structural Property Measurements 31

3 EFFECTS OF OXYGEN PRESSURE ON PHYSICAL PROPERTIES OF LPCMO THIN FILMS 33

3.1 Experimental Details 34
3.2 Results and Discussion 35
3.2.1 LPCMO on Untreated $NdGaO_3$ (NGO) 35
3.2.2 LPCMO on Treated NGO 39
3.3 Summary 40

4 SINGLE DOMAIN TO MULTI-DOMAIN TRANSITION DUE TO IN-PLANE MAGNETIC ANISOTROPY IN PHASE SEPARATED LPCMO THIN FILMS 42

4.1 Experimental Details 43
4.2 Results and Discussion 45
4.2.1 Structure and Transport 45
4.2.2 Magnetic Properties 47
4.2.3 Variation of Coercive Field with Temperature 49
4.2.4 Strain Induced Magnetic Anisotropy 54
4.3 Summary 58

5 ANISOTROPIC TRANSPORT IN LPCMO THIN FILMS 60

5.1 LPCMO (y = 0.6) Thin Films 61
5.2 Electric Field Induced Anisotropic Transport 64
5.3 Effects of Electric Fields and Strains on Magnetotransport 69
5.3.1 Current Effects on Magnetotransport 72
5.3.2 Strain Effects on Magnetotransport 73
5.4 Summary 76

6 OPTIMIZATION OF BMO THIN FILMS AND PHYSICAL CHARACTERIZATION 77

6.1 Optimization of BMO 78
6.2 Structural Study 86
6.3 Magnetoelectric Effects 89
6.4 Summary 90

7 CONCLUSION AND FUTURE WORK 92

REFERENCES 94

BIOGRAPHICAL SKETCH 101

LIST OF TABLES

Table page

2-1 Oxide substrates 24

2-2 Film growth condition of manganite thin films 27

5-1 Ideal composition and ratio of LPCMO 63

5-2 Composition of LPCMO at the middle of the thin films 63

5-3 Composition of LPCMO near the interface 64

LIST OF FIGURES

Figure page

1-1 Perovskite structure . . . 16

1-2 Energy diagram of a manganese ion in MnO_6 octahedra . . . 17

1-3 Trends of $\rho(T)$ in LPCMO with varying Pr contents . . . 19

1-4 Ferroelectricity due to empty d-shell . . . 22

2-1 Atomic force microscopy (AFM) images of treated substrates . . . 25

2-2 PLD set-up and plumes . . . 26

2-3 Schematic diagrams of transport measurements . . . 28

2-4 Magnetoelectric effect measurement set-up. . . . 31

3-1 AFM images of LPCMO thin films on untreated substrates . . . 34

3-2 $\rho(T)$, Max. TCR, and T_P of LPCMO thin films on untreated substrates . . . 35

3-3 $M(H)$ of LPCMO thin films on untreated substrates . . . 37

3-4 XRD patterns of LPCMO thin films on untreated substrates and NGO. . . . 37

3-5 Activation energy of LPCMO thin films . . . 38

3-6 AFM images of LPCMO thin films on treated substrates . . . 39

3-7 $\rho(T)$, Max. TCR, and T_P of LPCMO thin films on treated substrates . . . 40

4-1 $\rho(T)$ and AFM images of LPCMO thin films . . . 46

4-2 XRD results of LPCMO thin films . . . 47

4-3 $M(T)$ of LPCMO thin films . . . 48

4-4 In-plane ZFC magnetization hysteresis loops of LPCMO thin film on SLGO . . . 49

4-5 In-plane ZFC magnetization hysteresis loops of LPCMO thin film on NGO . . . 51

4-6 $H_c(T)$ and M_r(T) of LPCMO thin films . . . 52

4-7 $M(H)$ of the LPCMO thin film on NGO and atomic structure of NGO . . . 53

4-8 $M(H)$ with H along hard axis, $H_a(T)$, $H_c(T)$, and $K_u(T)$ of LPCMO thin films on NGO . . . 56

4-9 Angle dependent $H_c(T)$ and $H_c^{-1}(cos(\theta))$ of LPCMO thin film on NGO . . . 57

5-1 SEM image of LPCMO and TEM image of LPCMO (300 $\times$ . . . 61

5-2 TEM image of LPCMO (600 $\times$), SAD of LPCMO and NGO, and FFT of LPCMO 62
5-3 EDX and XRR of LPCMO 63
5-4 Proposed models for CER effect 65
5-5 Optical microscopy image of LPCMO and sequential transport measurements setup 66
5-6 Zero field R(T) in cross structure and CER effects 67
5-7 Isothermal R(t) measurements 69
5-8 Isothermal sequential R(V) measurements 70
5-9 Zero field R(T) of LPCMO and schematic diagrams of different MR 71
5-10 Current effects on magnetotransport and MER 72
5-11 R(H) in three different magnetic field directions at 60 K 73
5-12 dR/dT of R(T) under 8 T and three different AMR as a function of temperature . 74
6-1 The monoclinic unit cell of $BiMnO_3$ along (111) and (20$\bar{3}$) directions 79
6-2 $\theta - 2\theta$ diffraction of BMO thin films on STO grown in different oxygen pressure or different temperature 80
6-3 $\theta - 2\theta$ diffraction of BMO thin films on STO in different cooling rate 81
6-4 M(T) of BMO thin films 82
6-5 M(H) of BMO thin films 83
6-6 Ferroelectricity of a $BiMnO_3$ thin film on $SrTiO_3$ 85
6-7 $\theta - 2\theta$ diffraction pattern and GIXD of a BMO thin film on STO. Inset: ω scan of (111) BMO peak. 87
6-8 (a) Pole figure of $\{211\}$ STO and $\{110\}$ BMO (b) Reciprocal space map of the BMO thin film on STO. 88
6-9 X-ray reflectivity of BMO thin films on SLGO and STO. Inset: An AFM image of the BMO on SLGO. 89
6-10 $\theta - 2\theta$ and GIXD of BMO thin films on STO and SLGO. ϕ-scan of the BMO film and SLGO 89
6-11 M(T), R(T), and magnetoelectric effects of BMO on STO 91

Abstract of Dissertation Presented to the Graduate School
of the University of Florida in Partial Fulfillment of the
Requirements for the Degree of Doctor of Philosophy

MAGNETOELECTRIC EFFECTS IN MANGANITES

By

Hyoung Jeen Jeen

August 2011

Chair: Amlan Biswas
Major: Physics

Research on manganites has been conducted for more than half century. Recent discoveries of colossal responses to external fields such as colossal magnetoresistance effects and correlation among spin, orbital, and lattice in phase separated manganites and multiferroic manganites have motivated me to understand these materials. The main purpose of this dissertation is to understand magnetoelectric effects in phase separated $(La_{1-y}Pr_y)_{1-x}Ca_xMnO_3$ (LPCMO) thin films and multiferroic $BiMnO_3$ (BMO) thin films. First, high quality phase separated manganite thin films have been successfully grown. To grow the high quality manganite thin films, extensive effort was devoted to fine tuning of oxygen pressure, temperature, and laser fluence during film growth. As-grown films were characterized with various ex-situ techniques: magnetization measurements, transport measurements, x-ray diffraction, atomic force microscopy, and/or transmission electron microscopy to remove the effects of impurities and unwanted strains except substrate induced strain. Second, three major results were obtained in high quality phase separated LPCMO thin films. These results are based on the dynamic nature of phases in LPCMO. 1) LPCMO thin films showed single domain to multi-domain transition during cooling. This transition can be tuned by substrate stress induced in-plane magnetic anisotropy. 2) Evidence for the origin of colossal electroresistance (CER) effect has been observed. The CER is triggered by dielectrophoresis, or movements of ferromagnetic metallic (FMM) phase, which is manifested in anisotropic

transport properties in microfabricated LPCMO cross structures. This fluidic nature of the FMM phase in LPCMO under high electric fields lead to exotic magnetoelectric effects. 3) Electric field effects on magnetotransport properties have been observed. This phenomena can also be tuned by the combined effect of substrate strain and current flow. This combined effect of electric and magnetic fields and strain at the interface of LPCMO suggest new ways to control magnetism (magnetotransport) with electric fields. Third, impurity-free and epitaxial BMO thin films were grown. These films showed ferromagnetism and ferroelectricity at low temperature. Magnetoelectric effects are discussed, especially magnetization change due to electric fields.

CHAPTER 1
INTRODUCTION

1.1 General Introduction

Perovskite type manganese oxides (manganites) have induced renewed interests for the last two decades due to their colossal responses to external fields such as colossal magneto-resistance (CMR), colossal electro-resistance (CER), photo-induced metal-insulator transition, and colossal piezo-resistance (CPR) effects. [1–5] These responses are related to the correlation among lattice, spin, and orbitals. This correlation creates multiple ground states, *viz.* ferromagnetic insulator, ferromagnetic metal, antiferromagnetic charge ordered insulator, and paramagnetic insulator as a function of chemical doping, temperature, magnetic fields, electric fields, and strain fields. Currently, the origin of these colossal behaviors has been explained by phase competition (or phase separation) among different phases with similar free energies [6]. In other words, control of phases with external variables makes it possible to tune/modify the colossal behaviors. This point attracts scientists to try to understand and make use of these properties for possible device applications, e.g. bolometers, a resistive memory, and a magnetic memory [7, 8].

Recently, another aspect in manganites, multiferroism in manganites, has been highlighted due to the resurgence of interest in magnetoelectric effects, where magnetic (electric) polarization is controlled by electric (magnetic) fields [9–11]. This resurgence is not surprising, since we take advantage of magnetism and electricity in our everyday life. For example, computer hard drives use giant magneto-resistance effect, where electronic transport across ferromagnetic (FM) metal/ non-magnetic metal/ FM metal trilayers depends on relative magnetization directions of FM layers. Also, ferroelectric random access memory makes use of ferroelectric polarization to create non-volatile states. However, these devices can only perform binary operations, since just two degrees of freedom exist. If the ferromagnetism in a material can be controlled not only

by magnetic fields but also by electric fields, that material can produce four different states [12]. This property will be advantageous to minimize device size and increase degrees of integration. It has been predicted that the magnetoelectric coupling will depend on both magnetic and electric susceptibilities [9]. Thus, a strong candidate for such magnetoelectric effect is a material that is both ferromagnetic and ferroelectric material, which is a type of multiferroics [13, 14].

In this dissertation, two manganites, *viz.* phase separated $(La_{1-y}Pr_y)_{0.67}Ca_{0.33}MnO_3$ and multiferroic $BiMnO_3$, were investigated to find magnetoelectric effects. In the following sections, magnetoelectric effects, basics of manganites, phase separation, and multiferroism are described.

1.2 Magnetoelectric Effects

Magnetoelectric effect is defined as magnetization (electric polarization) change by electric (magnetic) fields. This effect can be derived from derivation of the free energy of materials. Free energy of a material can be expanded as a function of electric field (E) and magnetic field (H) [9, 15].

$$F(E,H) = \frac{\epsilon_0\epsilon_{ij}}{2}E_iE_j + \frac{\mu_0\mu_{ij}}{2}H_iH_j + \alpha_{ij}E_iH_j + \cdots, \tag{1–1}$$

$$P_i(E,H) = P_i^S + \epsilon_0\epsilon_{ij}E_j + \alpha_{ij}H_j + \cdots, \tag{1–2}$$

$$M_i(E,H) = M_i^S + \mu_0\mu_{ij}E_j + \alpha_{ij}H_j + \cdots, \tag{1–3}$$

First derivative of this free energy (F) to electric field (E) is the electric polarization (P_i). Its zeroth order term is the spontaneous polarization, which is commonly found in ferroelectric materials. Between the two first order terms, one, where the polarization is linearly dependent on the magnetic field, is called the linear magnetoelectric effect. In the first derivative of the free energy to magnetic field (H), the term, where the magnetic polarization (M_i) is linearly dependent on the electric field, is also called the magnetoelectric effect term. The constant (α) is called as linear magnetoelectric

coupling constant [9]. It is noted that higher order magnetoelectric effects exist. However, in this dissertation magnetoelectric effect will refer to the term, α. Since magnetoelectric effect is limited by magnetic and electric susceptibilities, it is expected that simultaneously ferromagnetic and ferroelectric materials will be the best option to get the maximal magnetoelectric effects [9]. However, the magnetoelectric effect in multiferroic materials is not very large. It was only reported small magnetodielectric effect in bulk $BiMnO_3$ [16]. Different origins in ferroelectricity and ferromagnetism would reduce the magnetoelectric coupling [17].

Here, exotic magnetoelectric effects in phase separated manganites will be introduced, which is related to change in their dielectric constant near the metal-insulator transition [9] and/or control of magnetic phases by electric field. The word 'exotic' means it does not includes magnetoelectric coupling in the usual sense as described earlier, even if it is manifested from magnetization changes under high electric fields in some system. For example, this effect is related to the electric field induced insulator to metal transition (colossal electroresistance), since manganite is a system, where charge, spin, and lattice are correlated [2]. Possible magnetoelectric effects in phase separated LPCMO thin film were investigated which could also reveal the origin of colossal electroresistance effects.

1.3 Basics of Manganites

1.3.1 Structure of Manganites

The manganites have the chemical formula ABO_3, where the A site is usually occupied by rare earth ions like Lanthanum (La), Praseodymium (Pr), and Neodymium (Nd) and the B site is occupied by a Manganese ion (Mn). The compound usually forms in the perovskite structure (Figure 1-1). When the A-site cation becomes small e.g. for the cation Yttrium (Y), manganites can have a different crystal structure, e.g. a hexagonal structure. In perovskite structure, rare earth ions are at the center of cube, Mn ions are at the corner of the cube, and oxygen ions are located in between Mn ions.

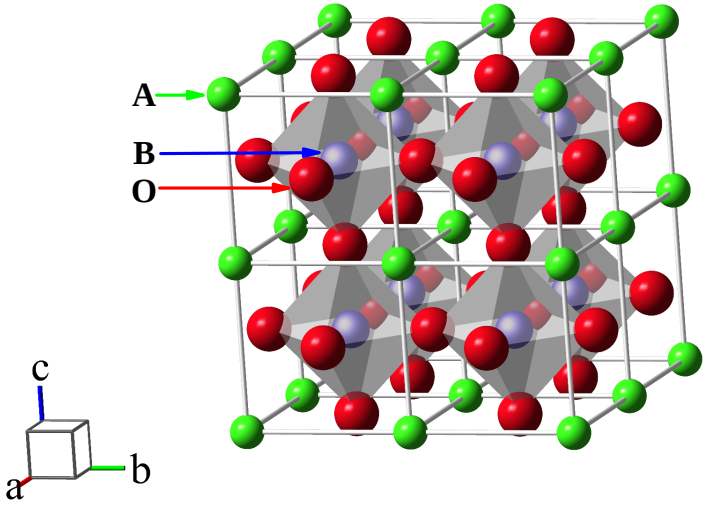

Figure 1-1. Perovskite structure [18]

These Mn ions are surrounded by six oxygen ions forming an MnO_6 octahedron. This means electronic energy levels of Mn ions are also governed by coulomb interaction from oxygen ions, which is known as the crystal field effect.

1.3.2 Electronic Configuration of Mn Ions

When an Mn ion is in free space, the energy of 3d orbitals are degenerate. However, when the Mn ion is surrounded by six oxygen ions (two in each axis), these oxygens provide a crystal field so that the d-orbitals will be split into two energy levels: t_{2g} level consists of three d-orbitals (d_{xy}, d_{yz}, and d_{zx}), which have low overlap with 2p orbitals of oxygen, while e_g level consist of two d-orbitals ($d_{x^2-y^2}$ and $d_{3z^2-r^2}$) which have higher energy than the t_{2g} orbitals due to higher overlap with the oxygen 2p orbitals. This effect is known as crystal field splitting (Figure 1-2). When Mn ions have valency of 3+, by Hund rule one electron is in e_g level while three electrons are in the t_{2g} level with same spin direction. Jahn-Teller effect takes place in the octahedron to minimize energy by distorting the octahedron. This distortion causes more energy splitting in both e_g and t_{2g} levels. If the elongation is along the z-axis, an electron in e_g level will be in $d_{3z^2-r^2}$ rather than $d_{x^2-y^2}$ due to less coulomb interaction from oxygen ions. Degrees of

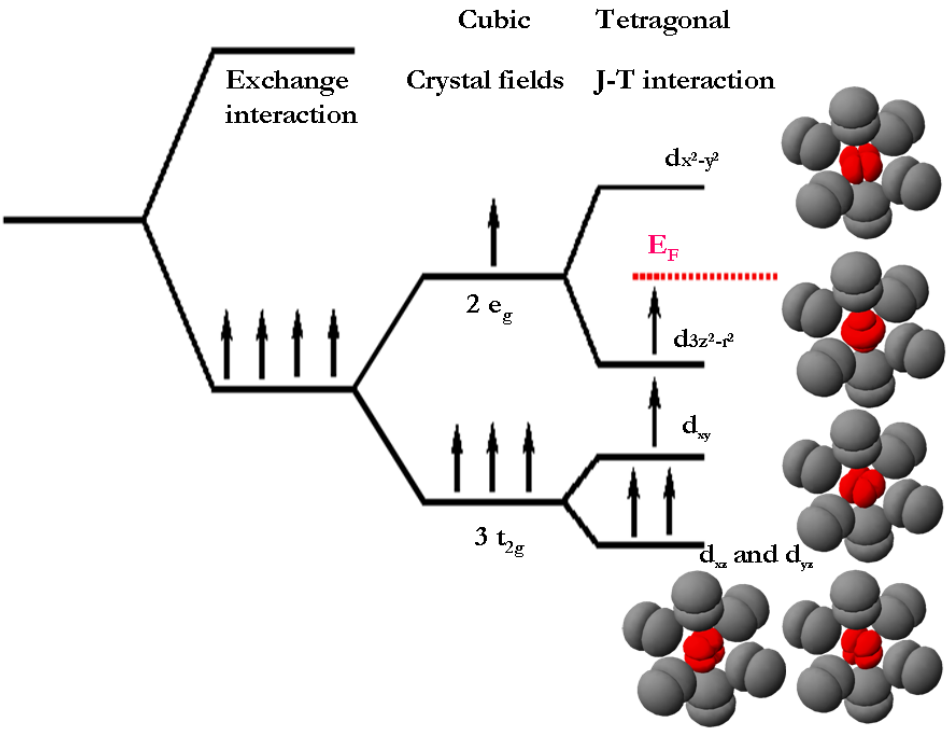

Figure 1-2. Energy diagram of a manganese ion in MnO_6 octahedra. Manganese orbital is red, and oxygen orbitals are grey.

Jahn-Teller distortion can be controlled by size of A site cation and chemical doping in the ideal case of defect-free samples.

When A-site is doped with divalent ions such as calcium, strontium, or barium, valency of Mn ions are in between 3+ and 4+. Lots of interesting phenomena have been observed due to this variation in valency of the Mn-ions. For example, even though its parent compounds, $LaMnO_3$ and $CaMnO_3$ are A-type and G-type antiferromagnetic insulators, $La_{1-x}Ca_xMnO_3$ in certain doping level shows metallic behavior and ferromagnetism at low temperature [19]. To explain this transport phenomena in hole doped manganites, two microscopic mechanisms will be introduced, *viz.* double exchange interaction at low temperature and polaron formation at high temperature.

1.4 Hole Doped manganites

1.4.1 Transport Mechanism in Mixed Valence Manganites.

Transport property and magnetic property in hole-doped manganites are closely related. Double exchange interaction can qualitatively explain transport property of hole-dope manganites. This interaction is the hopping of e_g electrons in manganites to empty e_g orbital via oxygen ions. A transferred electron should have the same spin direction as the t_{2g} electrons in Mn^{4+}, since empty e_g orbital states are strongly governed by t_{2g} electrons by Hund's coupling. Spin alignment and transfer mechanism mean that ferromagnetic and metallic behaviors come together. Following equation, proposed by Zener, explains increase of conductivity (σ), when temperature (T) is lower than a Curie temperature (T_C) [20, 21].

$$\sigma \approx \frac{xe^2}{ah}\frac{T_C}{T}, \tag{1–4}$$

where a is a lattice constant, x is hole concentration, and h is Planck's constant. Double exchange mechanism initially explains lots of puzzles of CMR behavior and low temperature conduction phenomena. However, high temperature resistance behavior, especially above magnetic Curie temperature, cannot be explained solely by double exchange mechanism.

Another important effect is the electron-phonon coupling or polaron formation. A polaron is defined as combination of the electron and its strain field in an insulator [22]. Localization of charge carriers occurs due to Jahn-Teller distortin of Mn3+ sites in mixed valence manganites [21]. Polaron formation explains the high temperature resistivity of mixed valence manganites, to a certain extent. Two polaron models are usually used for explaining high temperature behavior in manganites. The small polaron model shows following relation in resistivity (ρ) as a function of temperature (T), $\rho(T)$.

$$\rho(T) \propto T^{\alpha} Exp\left[\frac{E_A}{k_B T}\right], \tag{1–5}$$

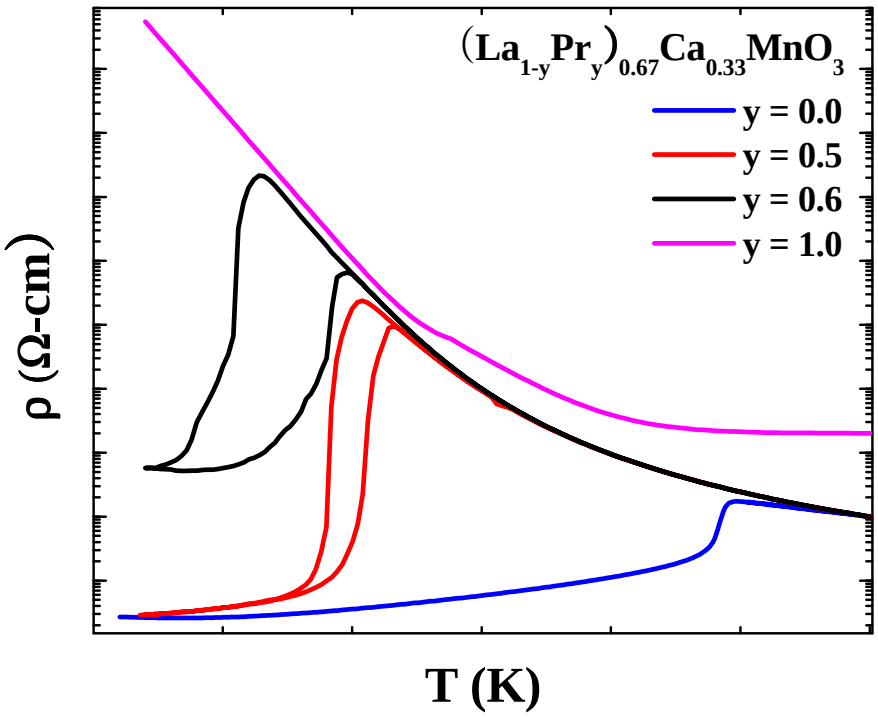

Figure 1-3. Schematic plot of resistivity as a function of temperature in LPCMO with different Pr contents.

where E_A is an activation energy, and k_B is Boltzmann's constant. The model predicts α = 1 for an adiabatic case in which charge carrier motion is faster than motion of lattice and α = 1.5 for a non-adiabatic case. The high temperature behavior of mixed valence manganites are generally well explained by this small polaron model [21, 23]. Another proposed model is the variable range hopping, which predicts ρ is proportional to $Exp\left[(\frac{1}{T})^{0.25}\right]$ in transport measurements [24].

1.4.2 Phase Coexistence in Hole Doped Manganites and (La, Pr, Ca)MnO_3 (LPCMO)

The optimally doped manganites usually show metal-insulator transition (MIT) with/without external fields. The MIT behavior has been interpreted as a result of electronic, magnetic, and possibly structural phase evolution. Coexistence of different phases has been observed with various techniques near MIT region and below MIT temperature. [8, 25–27]. Theoretically, it has been shown that quenched disorder and

long-range strain fields can create nano- or micro-meter scale phase separation [6, 28, 29]. Electronic phase competition such as competition between double exchange interaction and polaron formation in the long range coulomb repulsion can explain nano-meter-sized phase separation [30]. This idea has been re-considered after discovery of micro-meter scale phase separation in phase separated manganites, (La, Pr, Ca)MnO_3 system. As alternatives, a combination of quenched disorder and strain field due to difference in structure between insulator and metal provides a reasonable theoretical basis for such micrometer scale phase separation.

LPCMO is derived from $La_{0.67}Ca_{0.33}MnO_3$ (LCMO) and $Pr_{0.67}Ca_{0.33}MnO_3$ (PCMO). LCMO exhibits ferromagnetism and metallic behavior below about 250 K, while PCMO shows antiferromagnetism and insulating behavior, since Pr ion in the A-site creates more pronounced Jahn-Teller distortion. Additionally, PCMO shows charge ordering among Mn3+ and Mn4+ ions below about 200 K. LPCMO can be thought as a combination of these two compounds. For a certain ratio between La and Pr ions, even below insulator-metal transition, insulating phases and ferromagnetic metallic phase coexist (Figure 1-3). Coexistence was verified by different measurements such as dark field transmission electron microscopy, magnetic force microscopy (MFM), transport measurement, magnetization measurement, and recently Lorentz microscopy. [25–27] The possibility of chemical inhomogeneity has been ruled out by composition analysis and depinned magnetic region in MFM images. MFM results support percolative transport resulting in insulator-metal transition, since they showed growing magnetic regions during the insulator-metal transition. The MFM results are strong evidence of spatial correlation between metallic phase and ferromagnetic phase. Recently, detailed magnetic domain structure has been revealed by Lorentz microscopy. In narrow temperature range, single ferromagnetic domains break down to multi-domain ferromagnetic regions. This microscopic result has recently been confirmed by macroscopic magnetization measurements as part of this thesis work [8].

1.5 Multiferroism and $BiMnO_3$ (BMO)

Multiferroism was initially described as coexistence of multiple ferroic properties, *viz.* ferroelectricity, ferromagnetism, and ferroelastisity. A representative multiferroic material is $BiMnO_3$ (BMO). Currently, the definition of multiferroism includes antiferromagnetism, since some manganites, e.g. $YMnO_3$, $InMnO_3$, $TbMn_2O_5$, and $BiFeO_3$ (BFO) showed antiferromagnetism but (tunable) ferroelectricity under magnetic fields and thus a magnetoelectric effect. These multiferroic materials can be classified in terms of origin of ferroelectricity, since all the magnetic ordering originates from superexchange interaction [17, 31]. The first type of materials are ones in which ferroelectricity originates from A-site cation, i.e. BFO has lone pair electrons in Bi ions. Another type of materials are ones in which ferroelectricity is induced by magnetic frustration, e.g. spiral magnetic ordering and collinear spin ordering. This is called as improper ferroelectricity, since this is induced by more complex lattice distortion and/or some other ordering which mentioned above [17]. In the first type of materials the lone pair of the A-site cation distorts the crystal structure and results in a non-centrosymmetric structure thus breaking inversion symmetry and allowing ferroelectricity to exist. Among these materials, finding ferromagnetic and ferroelectric oxides is difficult, since ferromagnetism and ferroelectricity are mutually exclusive. Ferromagnetism in transition metal oxides requires partially filled d-electrons, since strong Hund coupling aligns electron spins in its own d-shell. The type of superexchange interaction determines long range magnetic orders, *viz.* antiferromagnetism or ferromagnetism. However, in transition metal oxides, e.g. $BaTiO_3$ and $PbTiO_3$, mechanism of ferroelectricity requires empty d-shell in B-site cations. The empty d-shell spontaneously makes covalent bonds with electron pairs of an oxygen atom, namely p-d hybridization [22] (Figure 1-4). This creates cooperative atomic displacements [15]. However, this hybridization could not happen in the system with partially filled d-shell of B-site cations due to coulomb repulsion between electrons. These requirements seem to indicate that coexistence of magnetic ordering and

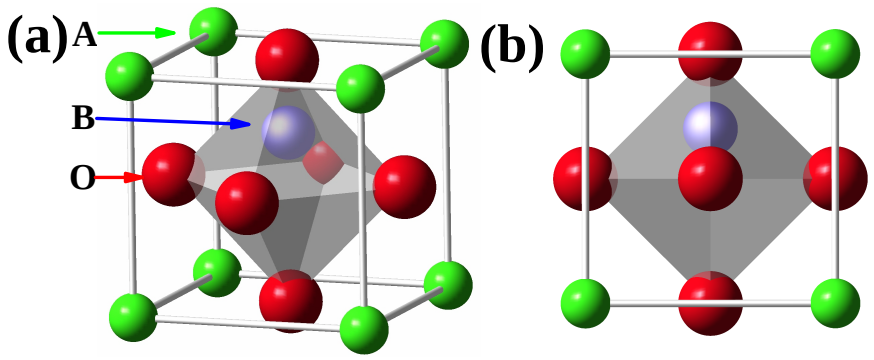

Figure 1-4. (a) Ferroelectricity due to empty d-shell in B-site cation (b) its projection [18].

ferroelectricity is not possible. However, there are very few multiferroic materials such as $BiMnO_3$ [32].

$BiMnO_3$ is predicted to have ferromagnetism below 105 K and ferroelectricity below 450 K [33]. The origin of ferroelectricity has been believed as lone-pair in Bi ions, while the origin of ferromagnetism is due to superexchange interactions among Mn ions. Recent experimental and theoretical results indicated centrosymmetry of $BiMnO_3$ crystal structure even in low temperature[34, 35]. Instead, it has been claimed that ferroelectricity in $BiMnO_3$ can be induced by peculiar orbital ordering. This orbital ordering creates long range antiferromagnetic (AFM) interactions [36–38]. This AFM interaction tends to break inversion symmetry. Experimentally and theoretically, this AFM interaction can be stabilized by oxygen content, defects, substrate strains, and pressure [36, 39–41]. One of the reasons contributing to this controversy is the difficulty of synthesizing BMO either in bulk or thin film form. BMO is a meta-stable phase, so its growth requires high pressure synthesis. Also, Bi ion is volatile, so it's easy to create cation vacancy. It is also reported that oxygen stochiometry is critical to explain ferromagnetism in bulk BMO. Rao *et al.* proposed that oxygen deficient samples are more ferromagnetic, while stochiometric BMO has antiferromagnetic transition temperature at around 30 K [39]. However, Belik *et al.* proposed it is hard to make oxygen deficient BMO sample. They showed that, when BMO is oxygen rich,

antiferromagnetism is induced [42]. BMO thin films have been studied extensively by several research groups, since the development of thin film deposition techniques makes it possible to stabilized the desired chemical phase via substrate strain [43]. For a decade, researchers used compressive substrate strain and Bismuth rich target to stabilize BMO phase. However, very few groups have successfully demonstrated ferromagnetism and ferroelectricity in BMO. Compared to bulk BMO research, research on physical properties of BMO thin films is in very early stage.

This dissertation is organized as follows: in Chapter 2, experimental techniques are introduced. Growth of high quality and epitaxial LPCMO thin films is discussed in Chapter 3. Chapter 4 describes the observation of single domain to multidomain transition in LPCMO thin films due to substrate stress induced in-plane magnetoanisotropy. Anisotropic (magneto)transport properties in LPCMO to capture the origin of CER effects and magnetoelectric effects are described in Chapter 5. Chapter 6 outlines the growth of impurity-free and epitaxial BMO thin films and their magnetoelectric effects. Conclusion and future work are given in Chapter 7.

CHAPTER 2
EXPERIMENTAL METHODS

2.1 Thin Film Growth

2.1.1 Substrate Surface Treatment

For thin film growth, four different epi-polished oxide substrates have been used, *viz.* (110) $NdGaO_3$ (NGO), (001) $SrTiO_3$ (STO), (001) $LaAlO_3$ (LAO), and (001) $SrLaGaO_4$ (SLGO) from CrysTec Gmbh (Table 2-1). NGO and SLGO substrates are grown by Czochralski method, while STO grown by Verneuill method. LAO substrates are grown by both methods. STO and NGO substrates were thermally and chemically treated to get atomic terraces. The advantages of getting atomic terraces are in providing a singly terminated surface and making it simpler to understand kinetics of thin film growth. It is noted that commercially available substrates are usually cut with small angle to surface normal. This miscut angle creates mixed surface termination of each substrate such as SrO and TiO_2 on an STO substrate.

Table 2-1. Oxide substrates

Substrate	Crystal structure	Direction	Lattice parameters (Å)
$NdGaO_3$ (110)	Orthorhombic	(110)	3.863
		$(1\bar{1}0)$	3.863
		(001)	3.854
$SrTiO_3$ (001)	Cubic	(001)	3.905
$SrLaGaO_3$ (100)	Tetragonal	(100) and (010)	3.842
		(001)	12.680

Here, treatment methods for NGO and STO substrates will be briefly introduced. These methods are based on published results [44–46]. First, NGO substrates were sonicated in acetone and ethanol for 5 minutes each. Then, NGO substrates were thermally treated in air for 30 minutes at 950°C. The temperature was ramped up at 10°C/min, while temperature was ramped down gradually to 550°C at 12°C/min and then allowed to cool down to room temperature after switching off the furnace.

Second, STO substrates were sonicated in ethanol for 5 minutes and in acetone for 5 minutes. STO substrates were soaked in deionized water at 55 - 70°C for 30 minutes

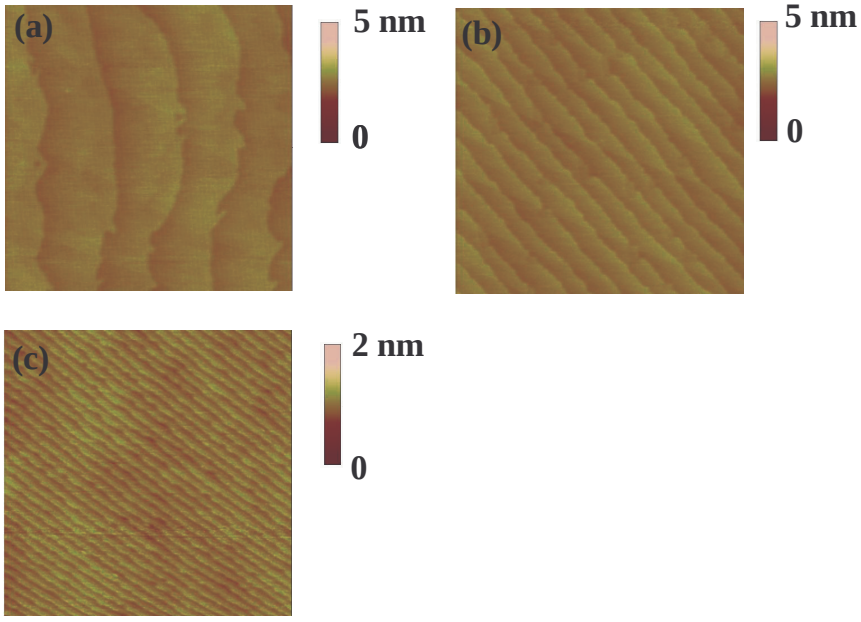

Figure 2-1. Atomic force microscopy images of treated substrates: (a) $NdGaO_3$, (b) $SrTiO_3$, and (c) $LaAlO_3$

in an ultrasonic bath to hydroxylate topmost SrO layer to $Sr(OH)_2$ [47]. Subsequently, these STO substrates were sonicated in mixture of hydrochloric acid (HCl) and nitric acid (HNO_3) (ratio: 3:1) for 12 minutes. After this chemical etching, these substrates were immediately soaked in deionized water for 30 seconds and dried with compressed air to stop chemical etching. Then, these substrates were thermally treated at 1000 - 1050°C for 30 minutes in air. These treated NGO and STO substrates consistently showed wide terraces and unit-cell height of steps (Figure 2-1). LAO and SLGO substrates were also treated. LAO was etched in hydrochloric acid for 5 min and treated for 30 minutes in 900°C. It showed local terraces and unit-cell height of steps. SLGO substrates were directly thermally treated at 840°C, since SLGO reacts with water. AFM image indicated rougher surface with no terraces and steps.

2.1.2 Pulsed Laser Deposition

Manganite thin films were grown using pulsed laser deposition (PLD) technique. The PLD technique has been used extensively for two decades owning to ease of

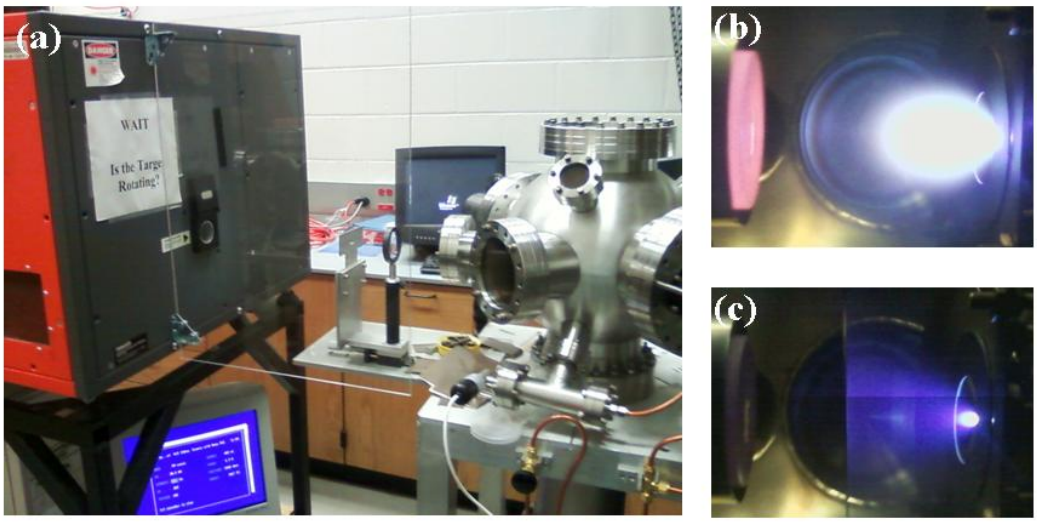

Figure 2-2. (a) Pulsed Laser deposition set-up, (b) Plume of LPCMO, (c) Plume of $BiMnO_3$.

handling and low cost of maintenance. It is well suited for growing multicomponent films like cuprate superconductors and manganites, since it is a non-equilibrium process [48]. Recently, atomic level control of deposition in PLD has created new avenue to study interface physics, e.g. interface conduction and interface superconductivity in between two insulators.

A PLD system uses a short laser pulse (about 25 ns for KrF laser) to vaporize the surface of polycrystalline target materials, and the resultant forward directed plume transports target components to a heated substrate without loss of stoichiometry in various gas environments (Figure 2-2). A KrF 248 nm pulsed laser was used and the deposition takes place in a high vacuum (HV) chamber which includes a carousel of 6 targets allowing growth of multi-layers without exposure of the sample to air. The control variables are substrate temperature, O_2 partial pressure, laser fluence, pulse repetition rate, and target-substrate distance. We varied the substrate temperature, O_2 partial pressure, and laser fluence for the optimization process. Optimization of thin film growth conditions has been completed for the following compositions: $(La_{1-y}Pr_y)_{0.67}Ca_{0.33}MnO_3$ (LPCMO) (y = 0.5 and 0.6), $La_{0.67}Sr_{0.33}MnO_3$, $La_{0.67}Ca_{0.33}MnO_3$, and $BiMnO_3$ (Table

2-2). Repetition rate was 5 Hz, and growth rates are 30 Å/min for $BiMnO_3$ and 25 Å/min for other manganite films. Atomic force microscopy, transport measurements, magnetization measurements, x-ray diffraction, and transmission electron microscopy have been conducted to confirm the optimization process.

Table 2-2. Film growth condition of manganite thin films

Composition	Substrate	Temperature (C°)	O_2 Partial pressure (mTorr)	Laser fluence (J/cm^2)
LPCMO (y = 0.5)	(110) $NdGaO_3$	780	150	0.5
LPCMO (y = 0.6)	(110) $NdGaO_3$	780	130	0.5
$La_{0.67}Ca_{0.33}MnO_3$	(110) $NdGaO_3$	780	200	0.5
$La_{0.67}Sr_{0.33}MnO_3$	(001) $SrTiO_3$	700	40	0.5
$BiMnO_3$	(001) $SrTiO_3$	634	35	1.2

2.2 Transport Measurements

Transport measurements were performed in an American Magnetics, Inc. (AMI) 9 tesla superconducting magnet system with Janis SuperVaritemp variable temperature insert. The temperature can be varied from 1.5 K to 300 K and a Lakeshore 332 temperature controller was used for temperature control. The magnetic field is controlled by an AMI 420 power supply programmer and model 4Q05100PS four-quadrant power supply. Two different types of transport measurements have been employed to measure resistance of manganite thin films.

2.2.1 Constant Current Sourced Measurements

Current source measurements utilize a Keithley 2000 voltmeter and a Keithley 220 current source (Figure 2-3 (a)). Thin film samples were cut to have dimensions of about 1 mm by 5 mm. Four equally distant indium dots were soldered along the longer side. These dots were connected to four pin connectors through gold wires. Four pin connectors were connected to the control panel with copper wires. Determination of resistance, based on the Ohm's law, can be made by measuring voltage drop across the inner two indium dots. In some cases, dc polarity reversal method has been employed to remove offset and thermoelectric voltages [49]. The scheme is to flip the current

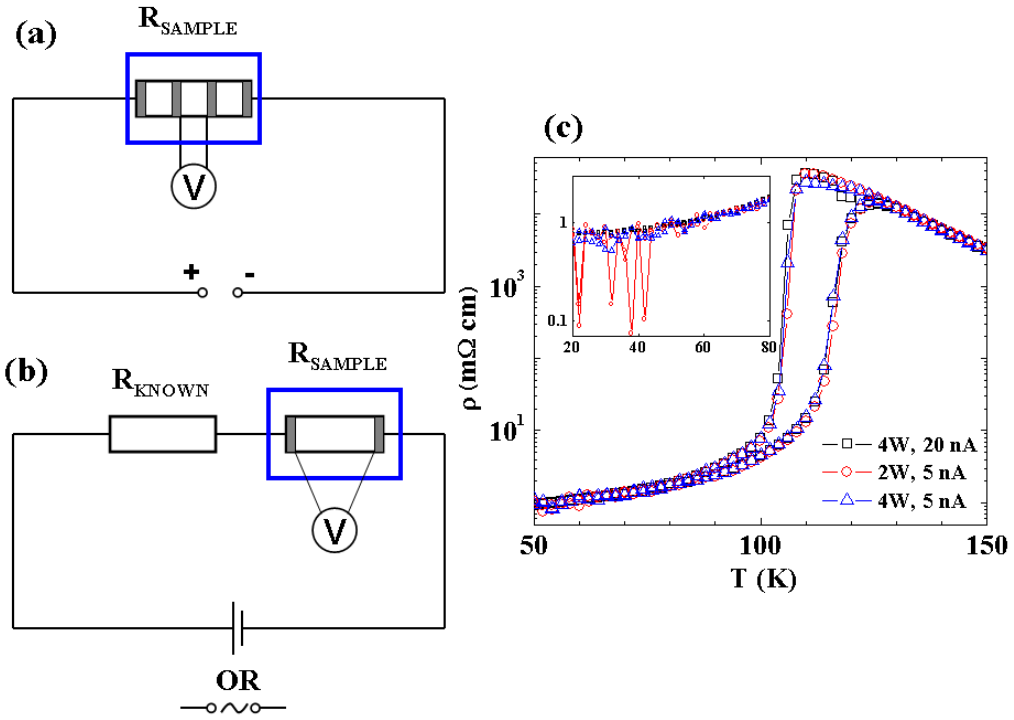

Figure 2-3. Schematic diagrams of transport measurement set-up for (a) current sourced four probe method and (b) voltage sourced two probe method. (c) Resistivity as a function of temperature of LPCMO (y = 0.5) taken by constant current sourced measurements.

direction in a specific manner, *viz.* positive, negative, and positive.

$$V_{1,+} = V_{sample} + V_{t,const}, \tag{2–1}$$

$$V_{2,-} = -V_{sample} + V_{t,const} + V_{t,linear}, \tag{2–2}$$

$$V_{3,+} = V_{sample} + V_{t,const} + 2V_{t,linear}, \tag{2–3}$$

$$V_{sample} = \frac{V_{1,+} - 2V_{2,-} + V_{3,+}}{4}, \tag{2–4}$$

$$R_{sample} = \frac{V_{sample}}{I_{applied}}, \tag{2–5}$$

where $V_{1,+}$, $V_{2,-}$, and $V_{3,+}$ are measured voltages, V_{sample} is a voltage across the sample, $V_{t,const}$ is a constant thermoelectric voltage, $V_{t,linear}$ is a linearly varying

thermoelectric voltage as a function of time, $I_{current}$ is an applied current, and R_{sample} is the sample resistance.

From the equations above, resistance of the sample can be determined. The dc polarity method is useful to observe pure resistance state of manganite thin films, since current is always off unless measurements are executed. This will allow minimization of electric field effects [3]. We checked effects of contact resistance on resistance of samples. We measured resistance of a LPCMO (y = 0.5) thin film on NGO substrate by two wire sensing and four wire sensing (Figure 2-3 (c)). Overall we could not find noticeable effects of contact resistances. However, in low temperature region (below 60 K), we observed resistivity gets noisy in two wire sensing and even four wire sensing in low current (5 nA). This noisy behavior can be resolved to use the higher current (I = 20 nA), since detection voltage gets larger.

2.2.2 Constant Voltage Sourced Measurements

Voltage sourced transport measurements have been done by putting a known resistor in series with a thin film sample (Figure 2-3 (b)) [50]. This method is suitable for measuring the resistance of highly resistive materials, once the sample resistance is higher than 100 MΩ and comparable to the input impedance of the voltmeter. A known series resistor of 1 MΩ at room temperature has been used. The voltage drop across the sample can then be calculated by subtracting the applied voltage from the measured voltage across the known resistor. The current in this series circuit can be calculated by dividing the measured voltage by known resistance value (1.001 MΩ). From these two calculated values, resistance of the sample can be calculated. This measurement makes it possible to measure resistances up to 100 GΩ. Also, this method can prevent possible current burst [2]. For dc measurements, we used Keithley 2400 source meter as voltage source and Keithley 2000 voltmeter for voltage sensing. For ac measurements, an SR-830 lock-in amplifier is used both as a voltage source and voltage sensor. A 100 kΩ as standard resistor has been used. It is noted that we used

low frequency ac voltage (about 5.6 Hz and less than 1 V_{rms}) to avoid capacitive effects and possible interference in simultaneous measurements with dc source. We select source frequency at the lowest temperature, which maximizes in-phase component of voltage sensing, since we are interested in resistance measurements.

2.3 Magnetization Measurements

Magnetic property measurements were done using a Quantum Design 5 T superconducting quantum interference device (SQUID). Magnetic field can be applied up to 5 T, and the temperature can be varied from 2 K to 300 K. Silver paints, used to attach the substrate to the PLD chamber heater, was removed after deposition from the backside of the thin films by grinding on sandpaper, then sonicated in ethanol. It is noted that we used plastic tweezers to avoid possible background signals in the SQUID magnetometer due to sample contamination. It has been observed that grinding with stainless steel tweezers creates significant magnetic signals. The sample is mounted on the inside of a straw and secured by additional inner straws. Typical magnetization measurements are magnetization as a function of temperature (M(T)) in fixed applied field and magnetization as a function of magnetic fields at fixed temperatures (M(H)). All the measurements can be programmed in the MultiVu software from Quantum Design.

Magnetoelectric measurements and magnetization change in electric fields have been measured using an electric field probe, which provides electrical connection points, so that voltage can be applied from a Keithley 2400 (Figure 2-4). To apply electric field, two methods have been used. First, two copper wires were soldered on two sides of thin films. The total electric field across the thin films is low such as $\approx$ 0.1 kV/cm, when 50 V is applied and the separation of two connections is $\approx$ 0.5 cm (typical size of thin films). Second, interdigital electrodes with alternating separation between 10 μm and 80 μm were used in order to apply higher electric fields. The electrode pattern was made with photolithography process in Nano Research Facilities, University of Florida. Deposition of 50-nm-thick Au-Pd alloys was done in the Major Analytical Instrumentation

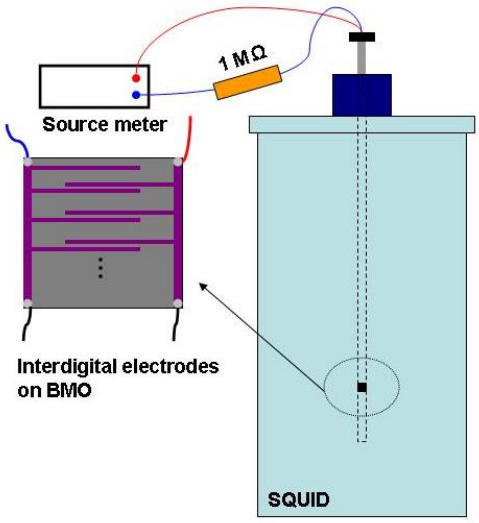

Figure 2-4. Schematic diagram of magnetoelectric effect measurement setup. 50-nm-thick Pd-Au interdigital electrodes used on a 60-nm-thick $BiMnO_3$ thin film.

Center (MAIC), University of Florida. After deposition, an entire film was sonicated in acetone for lift-off process. As a final step, two copper wires were soldered with indium to the electric field probe. Twenty six (26) pairs of 20 μm spacing and 27 pairs of 90 μm spacing were made. The expected electric fields are 25 kV/cm for 20 μm spacing and -5.55 kV/cm for 90 μm spacing for 50 V.

2.4 Surface and Structural Property Measurements

Surface morphology of various manganites is studied using a Digital Instrument multimode scanning probe microscope (SPM) with an extender module. Surface morphology was imaged with non-contact atomic force microscopy (AFM) mode. This SPM also provides other imaging modes such as contact AFM for imaging surface morphology, Kelvin force microscopy for measuring surface potential, and electric force microscopy for measure relative surface potential. Maximum scan size is 15 μm $\times$ 15 μm. For studying the interface between LPCMO (y = 0.6) and NGO, we used dual beam focused ion beam (FIB) milling and high resolution transmission electron microscopy

(HRTEM) in MAIC. The TEM sample of a LPCMO thin film was acquired as a result of FIB training by Dr. Gerald Bourne. The HRTEM was conducted by Dr. Kerry Siebein.

For structural study and phase identification, conventional θ-2θ x-ray diffraction (XRD) has been employed. Philips APD 3720 in MAIC has been used. This is a powder XRD, but with precise mounting, it is possible to scan the lattice parameter along surface normal. Also, it is suitable for identifying chemical phases of deposited materials. This instrument has been extensively used for the optimization of growth condition of $BiMnO_3$ thin films, since Bi ions near to the surface can escape during the cooling process. Additionally, high resolution x-ray diffraction of $BiMnO_3$ thin films was conducted by Dr. Valentin Craiciun in MAIC.

CHAPTER 3
EFFECTS OF OXYGEN PRESSURE ON PHYSICAL PROPERTIES OF LPCMO THIN FILMS

Manganites have shown colossal responses to external fields, since their structure, transport, and magnetism are closely related [1, 6, 25]. Thin flims of manganites exhibit unique properties associated with substrate induced strains [51–53]. Two directions of research in manganite thin films have been pursued. One is to get close to the physical properties of bulk materials [54]. Lots of efforts to reproduce bulk physical properties in manganite thin films have been made by post annealing in an oxygen rich environment or by growing films in highly energetic, reducing conditions [55, 56]. Another direction is to discover physical properties unique to in thin films and not found in bulk forms of the same compounds, *viz.* anisotropic transport, substrate induced metal-insulator transition, in-plane magnetic anisotropy, and insulator-metal transition in manganite superlattices [51, 53, 57, 58]. These unique properties require fine optimization of thin film growth conditions, so that we can only explore intrinsic properties from interrelation among structure, transport, and magnetism in manganites. Thus, the creation of atomically flat, epitaxial, and stoichiometric manganite thin films is an essential step to search for such unique physical properties.

We show that atomically flat, epitaxial, and stoichiometric $(La_{0.5}Pr_{0.5})_{0.67}Ca_{0.33}MnO_3$ (LPCMO) thin films on (110) $NdGaO_3$ (NGO) substrates can be optimized with fine control of oxygen pressure without conventional post-annealing. This optimization was confirmed by various physical property measurements, *viz.* surface, transport, structural, and magnetic measurements. The LPCMO thin films, grown under optimal oxygen pressure, have shown atomic steps, the highest maximum temperature coefficient of resistivity (max. TCR) and peak temperature (T_P), and ferromagnetic state at low temperatures. We propose that oxygen pressure affects the valency of Mn ion due to oxygen vacancy, cation vacancy, and creation/reduction of grain boundaries [55, 59, 60].

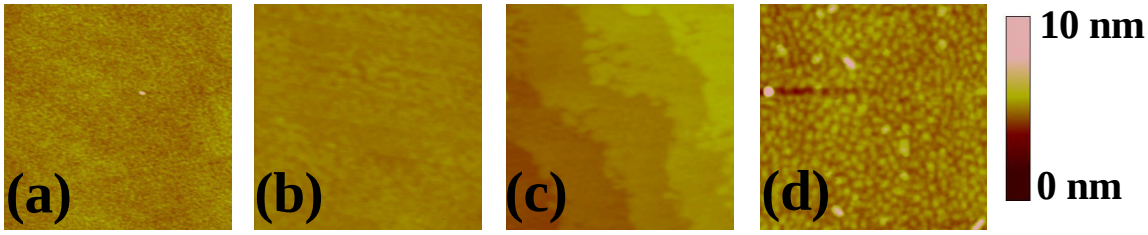

Figure 3-1. 1 μm $\times$ 1 μm AFM images of LPCMO thin films on as-received NGO substrates grown under (a) 100 mTorr, (b) 125 mTorr, (c) 150 mTorr, and (d) 175 mTorr.

3.1 Experimental Details

LPCMO thin films were grown on two different substrates, *viz.* as-received epi-polished (110) NGO substrates from CrysTec and subsequently thermally treated (110) NGO substrates. The detailed procedure can be found at section 2.1.1. Digital Instruments Multimode scanning probe microscope was used to study the surface morphology of the films in the tapping mode. Atomic force microscope (AFM) images of the treated substrates consistently showed atomic steps (about 0.4 nm) and low miscut angles (about 0.05°). We deposited LPCMO thin films using pulsed laser deposition (KrF, λ = 248 nm). The substrate temperature was 780°C, and laser fluence was kept at 0.5 J/cm^2, while oxygen pressure was purposely varied in each deposition from 75 mTorr to 200 mTorr. The thickness of the thin films was kept at 30 nm by controlling the deposition time, unless specified otherwise. During cool-down at 20°C/min, the oxygen pressure was kept at 440 Torr. Transport measurements were performed in a helium cryostat equipped with a Janis variable temperature insert. DC polarity reversal method was used with four probe wiring and low current (5 nA) to minimize current effect on manganites thin films [3]. Additionally, magnetization measurement and $\theta - 2\theta$ x-ray diffraction (XRD) were performed using a Quantum design 5 T SQUID magnetometer in B20, NPB and Philips APD 3720 in MAIC, University of Florida.

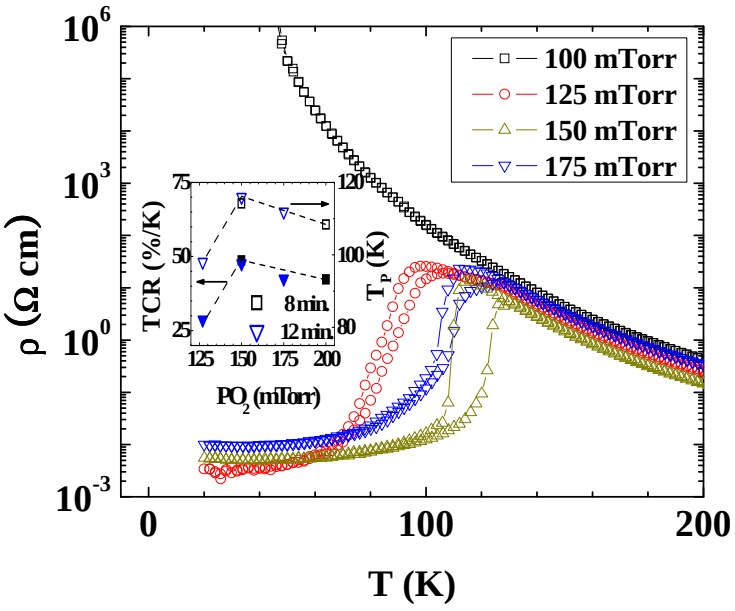

Figure 3-2. Resistivity as a function of temperature ($\rho(T)$) of the LPCMO thin films. Inset: Max. TCR and T_P as a function of oxygen pressure (PO_2). All dotted lines are guided for eyes.

3.2 Results and Discussion

3.2.1 LPCMO on Untreated $NdGaO_3$ (NGO)

In LPCMO thin films grown under different oxygen pressures, we observed differences in surface morphology (Figure 3-1 (a) - (d)). We observed very smooth surfaces with r.m.s. roughness of 0.5 nm in films grown under 100 mTorr or lower oxygen pressures. However, we could not find any characteristic features like islands or steps. Increasing oxygen pressure to 150 mTorr, we found atomic steps due to step flow growth mode in LPCMO films. Its step height (about 0.4 nm) is close to the height of an LPCMO unit cell. In 175 mTorr or higher oxygen pressures, thin films followed a 2D island growth mode. The r.m.s. roughness is still less than 0.5 nm. These films are different from LPCMO thin films showing 3D islands growth mode, which were grown under high laser fluence (1.0 ± 0.2 J/cm^2) and oxygen pressure (420 mTorr) with good transport properties [5]. In the oxygen pressure ranges we investigated, interlayer mass transport of LPCMO was well executed, since the r.m.s. roughness of all samples was

about the unit cell height of LPCMO [61]. The surface morphologies in these films were correlated with transport properties. The films with atomic steps showed the highest max. TCR and T_P. Max. TCR and T_P were lower in thin films which were grown under oxygen pressures diverging from the optimal oxygen pressure (150 mTorr). Both max. TCR and T_P have dome shaped features about the optimal oxygen pressure (Inset of Figure 3-2). When the oxygen pressure was below 100 mTorr during deposition, the grown films show insulating behavior down to the lowest temperature we measured. These trends indicate a change of the Mn4+/Mn3+ ratio [59]. The dome shaped features in max. TCR and T_P as a function of oxygen pressure can be explained by a change in the valency of Mn ion, since a similar change in valency has been observed in other hole doped manganites at around optimal doping of divalent cations [62]. For example, $La_{1-x}Ca_xMnO_3$ has its highest magnetic T_C at x = 3/8 with a dome shaped phase boundary [19]. Around the optimal doping, dome shaped phase boundary was achieved by doping with divalent Ca ion, which controls the valency of Mn ion. In our case, this change in the valency caused by varying oxygen content may create the dome shape of max. TCR and T_P about the optimal oxygen pressure. At less than 150 mTorr, the average valency of the Mn ion is towards 3+ from 3.67+ due to oxygen vacancy. However at higher than 150 mTorr, the valency of Mn ion is shifted toward 4+ due to cation vacancy rather than oxygen abundance, since oxygen rich manganites are hard to grow [59, 60]. This cation vacancy results from cation off-stoichiometry, i.e. change of ratio between Mn ion and other heavy cations (La and Pr ions) [56, 63]. If this originated from change of ratio between La ion and Pr ion, monotonic shift of T_P would be observed rather than dome shape T_P [25]. Also, grain boundary effect should be included to explain low max. TCR, low T_P, and higher resistivity at low temperature of the film grown in oxygen rich condition, since this film shows granular morphology (Figure 3-1 (d)) [64].

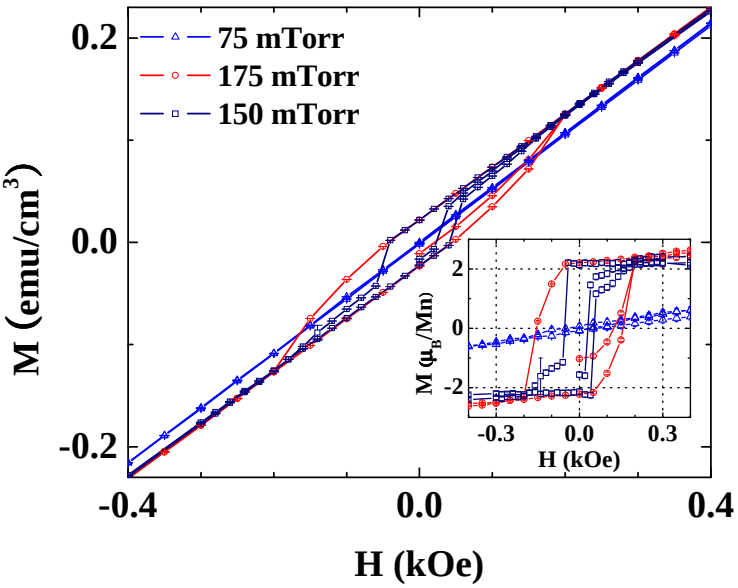

Figure 3-3. Magnetic moments (film and substrate) as a function of magnetic field, along [$1\bar{1}0$] direction of NGO, of LPCMO thin films on as-received NGO substrates. Inset: their magnetization hysteresis loops of the LPCMO thin films.

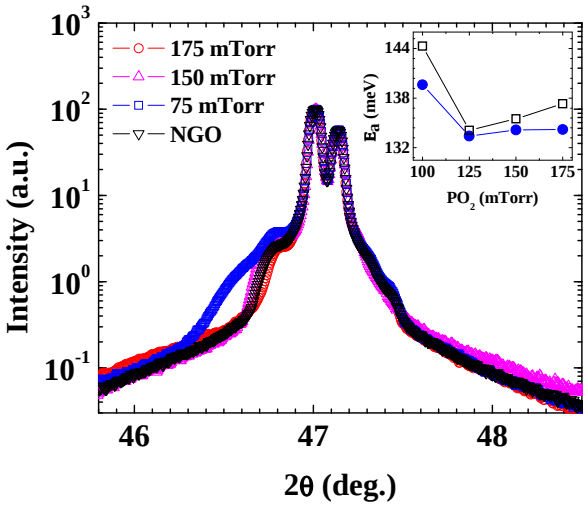

Figure 3-4. $\theta - 2\theta$ x-ray diffraction patterns of the LPCMO thin films on untreated substrates and a NGO substrate, Inset shows activation energies of LPCMO thin films on as-received NGO substrate (open square) and on treated NGO substrate (filled circle).

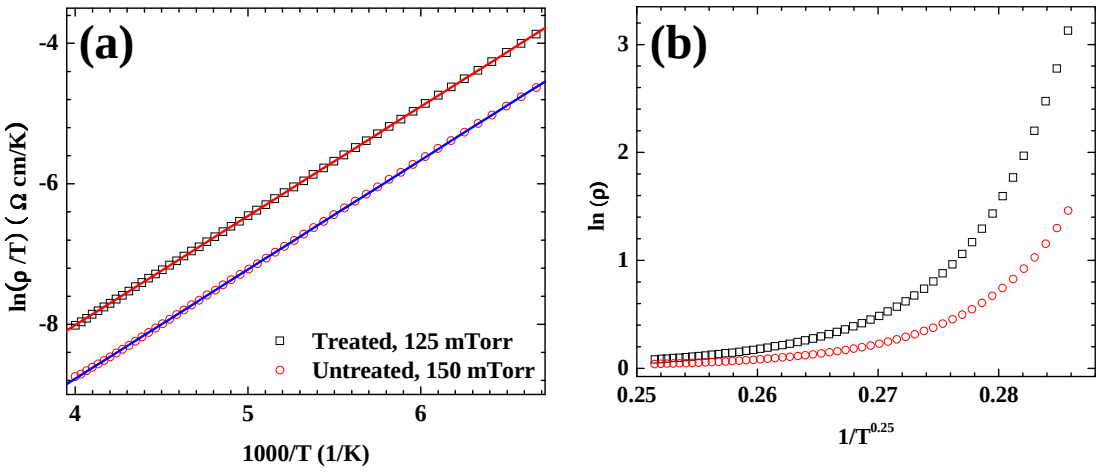

Figure 3-5. (a) ln(ρ/T) as a function of 1000/T of LPCMO thin films and fitting with adiabatic small polaron model. (b) ln(ρ) as a function of $T^{-0.25}$ to check the relevance of the variable range hopping model in the LPCMO thin films.

We performed XRD measurements and magnetization measurements at 50 K, since increase of lattice constant and reduction of magnetization are typically seen in oxygen deficient but optimally doped manganites [59, 60]. We observed pronounced reduction of remnant magnetization and disappearance of magnetic hysteresis in the film grown under 75 mTorr, after subtracting paramagnetic NGO signals by linear fitting (Figure 3-3) [8]. Also, we observed a diffuse and broad XRD peaks in the same film, while the XRD patterns of LPCMO thin films either with atomic steps or 2D islands were overlapped with the NGO substrate, since NGO substrate is nearly lattice matched to LPCMO (Figure 3-4). It was reported that oxygen deficient manganite films lower the valency of Mn ion toward 3+, so that the double exchange mechanism is hampered [59]. We also calculated activation energies of LPCMO thin films from transport data. The adiabatic small polaron model and the variable range hopping model were employed [21]. Figure 3-5 clearly shows the transport of LPCMO thin films can well fitted with the adiabatic small polaron model [23]. The activation energy does not show a huge variation among the thin films (inset of Figure 3-4). The activation energy is in 133.5 $\pm$ 0.5 meV for the films showing metal-insulator transition. Insulating films

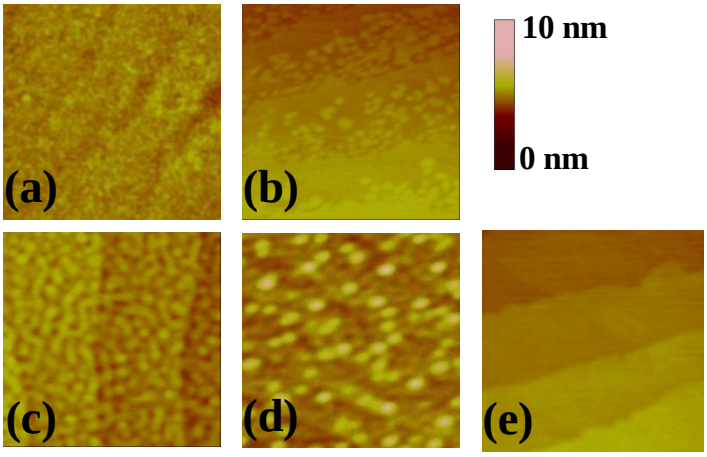

Figure 3-6. 1 μm $\times$ 1 μm AFM images of LPCMO thin films on treated NGO substrates grown under (a) 100 mTorr, (b) 125 mTorr, (c) 150 mTorr, and (d) 175 mTorr. (e) Treated NGO substrate for (b).

grown under 100 mTorr have a higher activation energy ($\approx$144 meV). Hence, oxygen vacancies may increase the activation energy. Combined with the hampered double exchange interaction, this higher activation energy may lead to a stronger insulator and no insulator-metal transition in oxygen deficient samples. From the measurements and analysis above, it is noted the LPCMO thin film with atomic steps can be differentiated from the LPCMO thin film with 2D islands, since the film with atomics steps has lower coercive fields and sharper changes of magnetic moments near to coercive fields(Figure 3-3). These reflect the grain boundary effects, since the films follow island growth [65].

3.2.2 LPCMO on Treated NGO

We also confirmed similar trends in surface morphology, transport, XRD, and magnetization measurements in LPCMO thin films on treated NGO substrates. It is noted that the atomic steps on LPCMO thin films followed the atomic steps on treated NGO substrates (Figure 3-6 (b) and (e)). This indicates that step edges on treated NGO provided energetically favorable sites for thin film growth [61]. The trends of max. TCR and T_P are similar in both LPCMO thin films on treated and as-received substrates (Inset of Figure 3-7). However, the optimal oxygen pressure for step flow growth mode

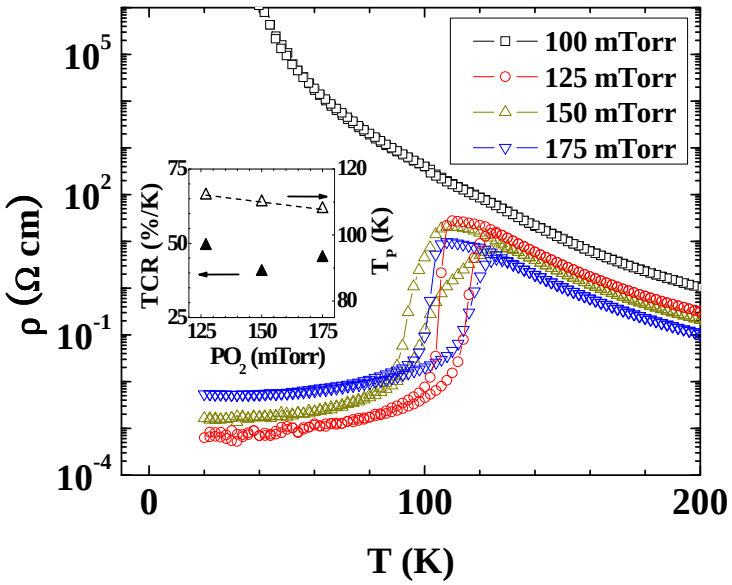

Figure 3-7. $\rho(T)$ of the LPCMO thin films. Inset: Max. TCR and T_P as a function of P_{O2}. A dotted line is guided for eyes.

is shifted down to 125 mTorr for the treated substrates. The windows for optimal oxygen pressure are rather narrow, since we got insulating thin films grown under 100 mTorr. The activation energy of LPCMO showing metal insulator transition is about 135.5 $\pm$ 1.5 meV. LPCMO grown under 100 mTorr has an activation energy of about 140 meV (Inset of Figure 3-4). We also observed a diffuse and lower angled LPCMO peak in XRD and lower magnetization in insulating LPCMO thin films grown under 75 mTorr. When the optimal films are compared, the best film on treated substrate showed no resistivity upturn at low temperature unlike the best film on the as-received substrate. Hence the film on the treated substrate is more metallic at low temperature. With the fact that the metallic phase in LPCMO thin films on NGO is favored, it reflects LPCMO thin films on treated substrates conform better than LPCMO thin films on untreated substrates [3].

3.3 Summary

We successfully grew atomically flat, epitaxial, and stoichiometric LPCMO thin films by tuning oxygen pressure. Surface morphology and transport measurements are critical measurements to optimize this LPCMO thin film [63], since transport and

magnetization measurements are not enough to characterize the thin films. Disorder in thin films is reduced when treated substrates with singly terminated atomically smooth substrate are used.

CHAPTER 4
SINGLE DOMAIN TO MULTI-DOMAIN TRANSITION DUE TO IN-PLANE MAGNETIC ANISOTROPY IN PHASE SEPARATED LPCMO THIN FILMS[1]

The coupling between structure, transport, and magnetism in hole-doped manganites leads to phenomena such as colossal magnetoresistance (CMR), colossal electroresistance (CER), photo-induced metal-insulator transition, and colossal piezoresistance (CPR) [1–5]. While these properties could lead to future applications in devices such as bolometers and cryogenic memories, manganites are already providing a unique insight into the effect of competing phases on the physical properties of materials [7, 66]. It is now widely accepted that phenomena such as CMR are consequences of the competition among different phases with similar free energy. Such competition leads to phase coexistence among three distinct phases, *viz.* cubic ferromagnetic metallic (FMM), pseudo-tetragonal (more precisely orthorhombic) antiferromagnetic charge ordered insulating (AFM-COI), and pseudo-cubic paramagnetic insulating (PMI) phases, in materials such as $(La_{1-y}Pr_y)_{1-x}Ca_xMnO_3$ [6, 25, 26]. In addition to well-known effects such as CMR and CER, the coexistence of the three magnetic phases also leads to phenomena such as temperature dependent magnetic domain transition and ellipsoidal growth of the FMM phase, which have been observed using Lorentz microscopy in very narrow temperature ranges [27]. Due to the same coupling between crystal structure, transport, and magnetism, manganite thin films have shown properties distinct from bulk behavior such as substrate strain induced metal-insulator transition and anisotropic transport due to strain fields from substrates [51, 53]. The effect of strain on the transport properties of manganites has been widely studied and it is accepted that multiphase coexistence and percolation play a significant role [3, 25, 26]. However, the effect of strain on the magnetism of phase separated manganites is more subtle and

[1] E-printed with permission from Hyoungjeen Jeen and Amlan Biswas, Phys. Rev. B, **83**, 064408, (2011). Copyright 2011, American Physical Society.

is still being debated. One such problem is the distinction between intrinsic magnetic properties and extrinsic effects on magnetic properties of manganite thin films. For example, when $La_{0.77}Ca_{0.33}MnO_3$ thin films were grown on single crystalline $NdGaO_3$ substrates, Mathur *et al.* concluded that the in-plane magnetic anisotropy originated not from stress anisotropy but from magnetocrystalline anisotropy [67]. Here, we report that substrate induced stress plays an integral role in determining the magnetic properties of manganite thin films. We observe that in-plane stress anisotropy leads to an in-plane magnetic anisotropy and a magnetic domain transition as a function of *temperature* in phase separated $(La_{1-y}Pr_y)_{1-x}Ca_xMnO_3$ (x = 0.33 and y = 0.6) thin films grown on (110) $NdGaO_3$ substrates with anisotropic in-plane strain. Our data show that while anisotropic stress has a profound effect on the magnetism, the in-plane resistivity of the films remains virtually isotropic. By comparing our results for the films on anisotropic NGO to those grown on isotropic (001) $SrLaGaO_4$ (SLGO) substrates, we conclude that anisotropic strain can be used to control the magnetic "hardness" i.e. the coercive field in a mixed phase manganite. Such control could play an important role in the design of nanomagnetic devices.

4.1 Experimental Details

$(La_{1-y}Pr_y)_{1-x}Ca_xMnO_3$ (LPCMO, x = 0.33 and y = 0.6) thin films of two different thicknesses (30 nm and 20 nm) were grown on orthorhombic (110) $NdGaO_3$ (NGO) substrates by pulsed laser deposition (PLD) (KrF, λ = 248 nm). The substrate temperature during growth was 780°C, O_2 partial pressure was 130 mTorr, laser energy density was about 0.5 J/cm^2, and growth rate was kept at about 0.4 Å/s. Step flow growth has been consistently observed under these conditions in the LPCMO thin films up to 60 nm thickness. The magnetic response reported in this work was observed in four different films. The thickness was controlled by deposition time and then confirmed by atomic force microscopy [68]. The lattice mismatch strains in the two in-plane directions of LPCMO thin films grown on NGO substrates (LPCMO//NGO) are $\delta_{1\bar{1}0} = 0.49\%$ and

$\delta_{001} = 0.26\%$ due to different in-plane lattice parameters of the NGO substrates ($d_{1\bar{1}0}$ = 3.863 Å, d_{001} = 3.854 Å, d_{LPCMO} = 3.844 Å) [69, 70], where $\delta(\%) \equiv \frac{d_{substrate}-d_{film}}{d_{film}} \times 100$. We also grew 30-nm-thick LPCMO thin films on (001) tetragonal $SrLaGaO_4$ (SLGO) substrates (LPCMO//SLGO) using the same growth parameters given above. Since the substrate induced strain on LPCMO//SLGO thin films is negligible due to well matched in-plane lattice parameters of SLGO (d = 3.842 Å), the films grown on the two different substrates can be used to isolate the effect of anisotropic strain on the magnetism and transport of LPCMO. The structure of the films was characterized by conventional $\theta - 2\theta$ x-ray diffraction using a Philips APD 3720 diffractometer. Magnetic properties were measured using a Quantum Design 5 T Superconducting Quantum Interference Device (SQUID) magnetometer. Since LPCMO thin films show thermal hysteresis in both magnetic and transport properties, thermal demagnetization was executed by heating up to 150 K (a temperature higher than the hysteretic region and the magnetic Curie temperature, $T_C \approx 130$ K) before each measurement. Field demagnetization of the superconducting magnet was also performed at 150 K. For measuring the magnetic moment as a function of temperature ($M(T)$), a 100 Oe field was applied to minimize magnetic field induced phase change of the LPCMO films [71]. Two different methods were used to remove the background paramagnetic signal from the NGO substrates and obtain the magnetic moments of LPCMO films. The first method was direct subtraction for which magnetic moment measurements as a function of applied field ($M(H)$) were carried out at different temperatures for the bare NGO substrates before film deposition. $M(T)$ was also measured for the same substrates in a field of 100 Oe. After deposition of the LPCMO films on the substrates, $M(H)$ and $M(T)$ curves were acquired under the same conditions as the magnetization measurements of bare NGO substrates. The $M(H)$ and $M(T)$ curves of the substrates were then subtracted from the corresponding $M(H)$ and $M(T)$ curves of the film plus substrate to obtain the magnetic moments of the LPCMO thin films. The second method was based on linear background fitting. The

raw $M(H)$ data of LPCMO films have signals both from the ferromagnetic films and the paramagnetic NGO substrates. Since the paramagnetic signal is linear at low fields, the background signal can be obtained by fitting a linear function to the data from 700 Oe to 2000 Oe (i.e. magnetic fields greater than the coercive field), and then subtracted from the raw data to obtain the magnetic moments of LPCMO films. The linear background fitting procedure can be used only for the $M(H)$ measurements. Background subtraction was not required for LPCMO films grown on non-magnetic SLGO substrates. A Digital Instruments Multimode scanning probe microscope was used in the tapping atomic force microscope mode to check the surface morphology and thickness of the thin films [68]. Resistivity as a function of temperature ($\rho(T)$) was measured in a helium cryostat equipped with a Janis variable temperature insert.

4.2 Results and Discussion

4.2.1 Structure and Transport

The surfaces of our LPCMO thin films on both NGO and SLGO substrates are smooth on an atomic scale (insets of Figure 4-1(a) and 4-1(b)). The r.m.s. roughness of the LPCMO//NGO films is about 2 Å. The films on NGO usually show step-flow growth mode with unit cell step height as shown for the 20 nm-thick film (inset of Figure 4-1(a)). The step height is about 4 Å, which is comparable to the lattice constant of bulk LPCMO. The r.m.s. roughness of a 30-nm-thick LPCMO//SLGO film is about 4 Å and step-flow growth was not observed. Resistivity measurements of the LPCMO//NGO films show sharp transitions at the insulator-metal transition temperature (T_{IM}, obtained while cooling) and metal-insulator transition temperature (T_{MI}, obtained while warming) whereas, the LPCMO//SLGO thin films show a more gradual transition and narrower thermal hysteresis (Figure 4-1(b)) [72]. The T_{MI} of the 20-nm-thick LPCMO//NGO thin film was about 92 K, which is 16 K higher than that of the 30-nm-thick film, while the T_{IM} are within 4 K (60 K for the 20-nm-thick film and 56 K for the 30-nm-thick film). The large variation of T_{MI} with thickness is related to the strain-induced static phase separated

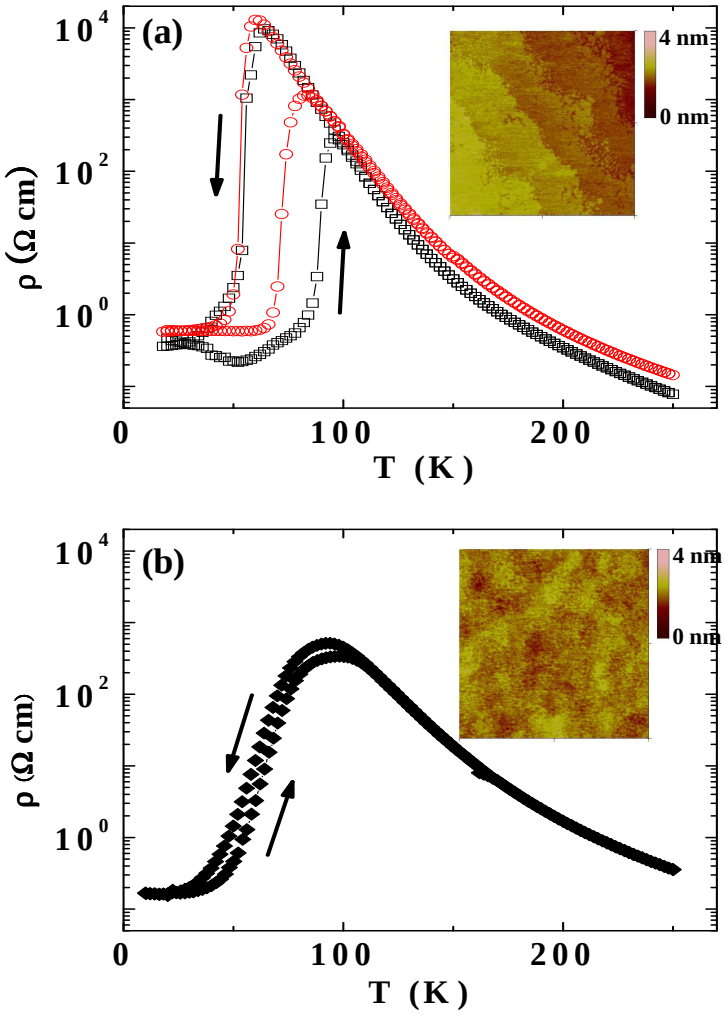

Figure 4-1. (a) $\rho(T)$ of a 30-nm-thick (circle) and 20-nm-thick (square) LPCMO films on (110) NGO substrates. The inset shows a 2 μm $\times$ 2 μm AFM image of a 20-nm-thick LPCMO thin film grown on NGO. (b) $\rho(T)$ behavior of a 30-nm-thick LPCMO thin film on an SLGO substrate. The inset shows a 2 μm $\times$ 2 μm AFM image of a 30-nm-thick LPCMO thin film on SLGO.

(SPS) state at low temperatures and we are currently performing experiments to study this effect in detail [3]. $\theta - 2\theta$ x-ray diffraction pattern of the 30-nm-thick LPCMO//NGO film did not show any individual LPCMO peaks due to the similar lattice parameters of LPCMO and (110) NGO in the out-of-plane direction, while the x-ray diffraction pattern of the LPCMO//SLGO film clearly shows sharp LPCMO peaks (Figure 4-2). Thus, all the LPCMO films were grown with a single chemical phase and were highly ordered along

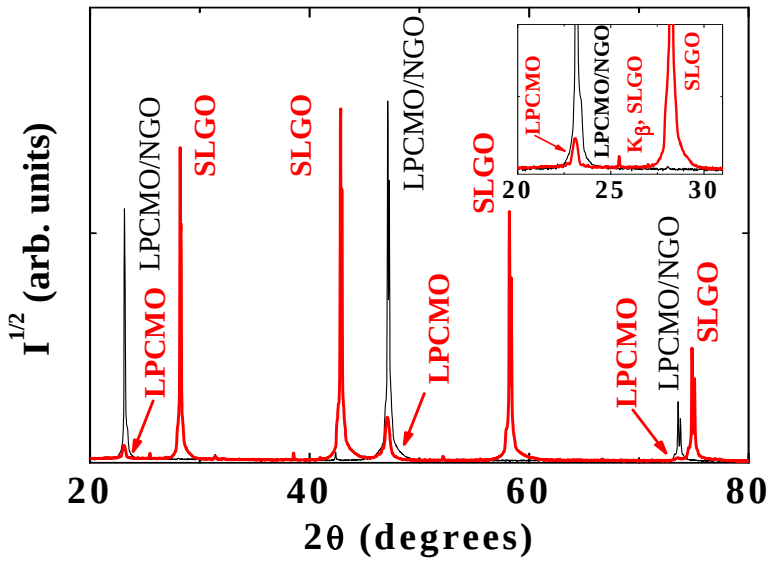

Figure 4-2. $\theta - 2\theta$ x-ray diffraction patterns of the 30-nm-thick LPCMO thin film grown on an SLGO substrate (thick line) and the 30-nm-thick LPCMO thin film grown on an NGO substrate (thin line). The inset shows the low angle region in detail.

perpendicular direction to the substrate surface. The films are smooth on an atomic scale and show sharp resistivity transitions at T_{IM} and T_{MI}.

4.2.2 Magnetic Properties

Figure 4-3 shows $M(T)$ curves of a 30 nm-thick LPCMO//NGO thin film, taken under field cooling (FC) and field cooled warming (FCW) in a field of 100 Oe applied parallel to the [$1\bar{1}0$] NGO direction. We will show in section 4.2.4 that the [$1\bar{1}0$] NGO direction is the easy axis for the LPCMO//NGO films. We used the direct subtraction method to get the magnetic moments of the LPCMO//NGO films only. Due to the background subtraction, the zero field cooled (ZFC) $M(T)$ data is accompanied by a large relative error and hence is not shown here. The $M(T)$ behavior is similar to previous results obtained for bulk LPCMO (x = 0.375 and y =0.600) [73]. The paramagnetic to ferromagnetic transition occurs at approximately 130 K. Although the entire film does not become ferromagnetic at 130 K since these films show multiphase coexistence, we define the T_C to be approximately 130 K, at which M

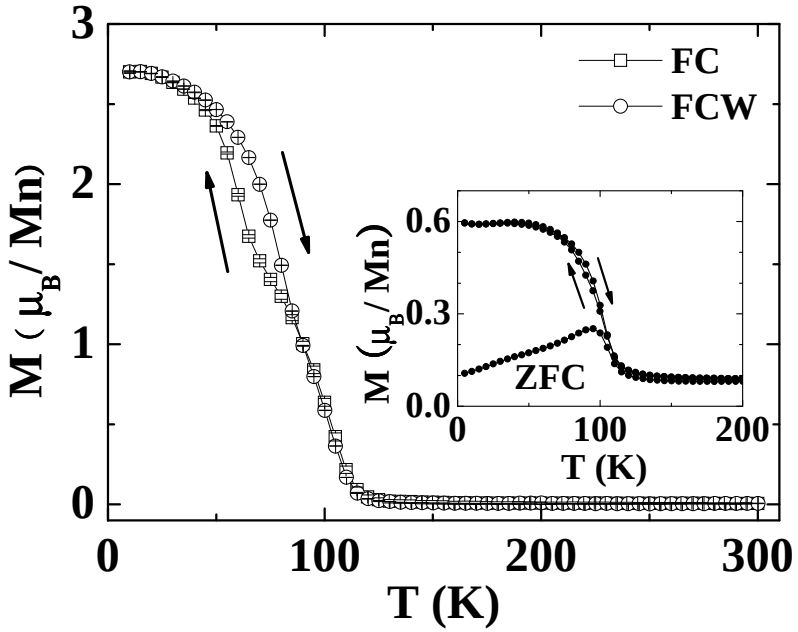

Figure 4-3. $M(T)$ of the 30-nm-thick LPCMO thin film on NGO under field cooling (FC) (square) and field cooled warming (FCW) (circle) runs in a 100 Oe field along the $[1\bar{1}0]$ NGO direction. The inset shows $M(T)$ behavior of the 30-nm-thick LPCMO film on SLGO under zero field cooling (ZFC), field cooling (FC), and field cooled warming (FCW) in an in-plane 100 Oe field.

becomes a measureable non-zero value [74]. While this definition of T_C is not robust, it approximately marks the temperature at which the ferromagnetic regions are first nucleated. The $M(T)$ graph shows thermal hysteresis in the FC and FCW runs at similar temperatures where we observed hysteresis in the $\rho(T)$ behavior. This hysteresis is due to the fluid phase separated (FPS) state transforming into the glassy static phase separated (SPS) state at low temperatures [3, 71]. The magnetic moment saturates below 30 K as the LPCMO//NGO film enters the SPS region. In the SPS state the FMM regions are frozen in space and hence the magnetic moment is constant with a reduction in temperature [3, 71]. The transition from the FPS to SPS state also leads to a unique behavior of the coercive field as a function of temperature to be described in the next section. $M(T)$ behavior of the LPCMO//SLGO film is shown in the inset of Figure 4-3, which shows magnetic thermal hysteresis and saturation of the magnetic moment (0.6 μ_B/Mn) below 30 K, similar to the LPCMO//NGO film.

4.2.3 Variation of Coercive Field with Temperature

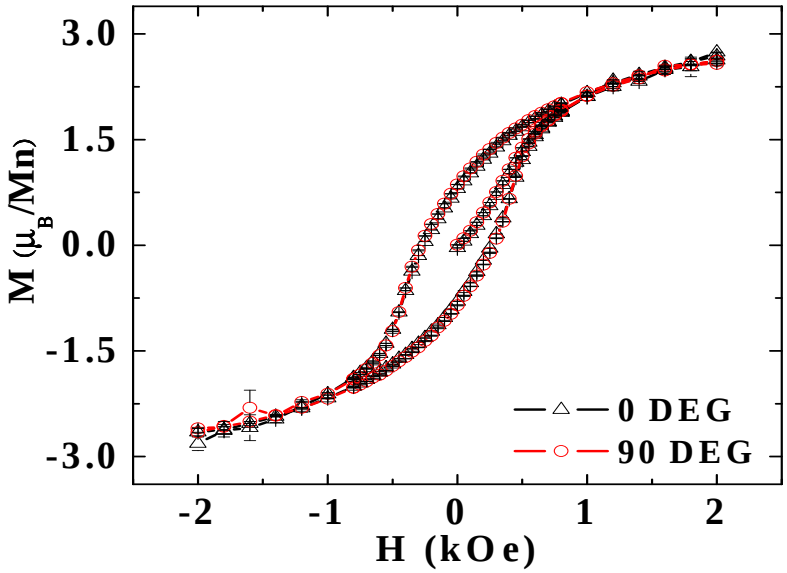

Figure 4-4. In-plane zero field cooled (ZFC) magnetization hysteresis loops of the 30-nm-thick LPCMO thin film grown on SLGO along the two orthogonal in-plane directions at 50 K.

We will now discuss the effect of anisotropic strain on the magnetic properties of phase separated manganites. Previous studies have shown that in-plane anisotropic strain leads to uniaxial magnetic anisotropy in the plane of the thin film [57, 67]. However, these studies were performed on purely ferromagnetic manganites. In a phase separated manganite, we expect that the magnetic anisotropy may lead to anomalous behavior of the submicrometer sized ferromagnetic regions [26]. Magnetic hysteresis loops of the thin films were measured in the zero field cooled (ZFC) state to study the pure unmagnetized state at each temperature. The magnetic moments of LPCMO//SLGO films could be directly measured, since SLGO substrate is non-magnetic. NGO substrates are paramagnetic, which necessitates a careful background subtraction to obtain the magnetization of LPCMO//NGO films. The $M(H)$ data were measured along two in-plane directions of the SLGO substrate, *viz.* [100] and [010]. Magnetic hysteresis loops in the two directions show that there is negligible magnetic anisotropy at all measured temperatures in terms of remanences

and coercive fields as shown in Figure 4-4 for $T = 50$ K. The significance of these isotropic hysteresis loops will be discussed in section 4.2.4. The $M(H)$ loops also show that the remanences are much lower than magnetic moments at 2 kOe (Figure 4-4), which suggests weak interaction among ferromagnetic regions in the LPCMO//SLGO films [75]. Due to the large paramagnetic signals from the NGO substrates we used two different methods *viz.*, direct subtraction and linear background fitting to get ZFC magnetic hysteresis loops of the LPCMO//NGO films. The magnetic field is applied parallel to the $[1\bar{1}0]$ direction of the NGO substrates which is also the magnetic easy axis of the films on NGO (sectoin 4.2.4). As shown in Figure 4-5, the $M(H)$ loops obtained using direct subtraction and linear background fitting show similar results. For example, at 50 K direct subtraction gives a coercive field of 230 $\pm$ 4 Oe and a remanence of 2.4 $\pm$ 0.1 μ_B/Mn while linear background fitting gives a coercive field of 230 $\pm$ 5 Oe and a remanence of 2.3 $\pm$ 0.1 μ_B/Mn. The two background subtraction methods show similar results throughout the temperature range investigated. Compared to the LPCMO//SLGO films, the LPCMO//NGO films show rectangular $M(H)$ loops i.e. their saturation magnetization is comparable to their remanence. The sharp change of the magnetic moment at the coercive field supports domain wall motion by either nucleation model or pinning model, and the rectangular shape of hysteresis loops implies a strongly developed uniaxial anisotropy in the LPCMO thin films on NGO substrates, as discussed in section 4.2.4 [75].

The T_C of the LPCMO//NGO film is approximately 130 K (Figure 4-3). From 130 K down to 80 K, the observed coercive fields are less than the field step size. While such small H_c could be due to small single domain (SD) FMM regions in a matrix of PMI and/or COI phases, we believe that the remanent field in the superconducting magnet in a SQUID magnetometer gives rise to the observed hysteresis in this temperature range [76]. Hence, we assume that $H_c \approx 0$ and that the film is in a super-paramagnetic state from 130 K down to 80 K. Below 80 K, the H_c first increases sharply to about

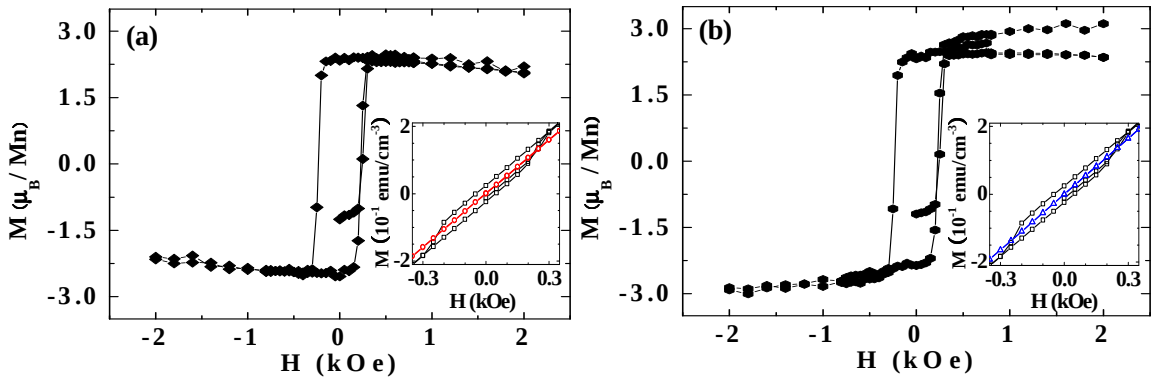

Figure 4-5. (a) ZFC magnetization hysteresis loop of the 30-nm-thick LPCMO thin film grown on NGO, at 50 K with the field applied along [$1\bar{1}0$] direction of the NGO substrate after using direct subtraction (DS). The inset shows $M(H)$ behavior of the substrate before deposition (circle) and the film plus substrate after deposition (square). (b) ZFC magnetization hysteresis loop of the 30-nm-thick LPCMO thin film grown on NGO, at 50 K with the field applied along [$1\bar{1}0$] direction of the NGO substrate after using linear background fitting. The inset shows $M(H)$ behavior of LPCMO and NGO (square) and the fitted paramagnetic background (triangle).

300 Oe at 60 K and then decreases gradually to about 190 Oe at 30 K (Figure 4-6(a)). However, M_r increases monotonically as the temperature is decreased from 80 K to 30 K (inset, Figure 4-6(a)). The behavior of H_c and M_r as a function of temperature shows that the FMM regions grow in the same temperature range in which the coercive field shows non-monotonic behavior. The growth of the FMM regions with lowering temperature is supported by magnetic force microscopy, Lorentz microscopy, transport measurements, and other magnetic measurements [25–27]. The non-monotonic behavior of H_c as a function of temperature along with the monotonic increase of M_r strongly suggests an SD to multidomain (MD) transition as a function of temperature. SD FMM regions are nucleated below T_C and grow down to 60 K. Further growth of the FMM regions below 60 K results in MD behavior and hence, a decrease in H_c. Such magnetic domain transition is typically observed in ferromagnetic fine particles as a function of particle size [77]. Here we observe an SD to MD transition with

decreasing temperature due to an increase in size of FMM regions embedded in a non-ferromagnetic AFM-COI/PMI matrix.

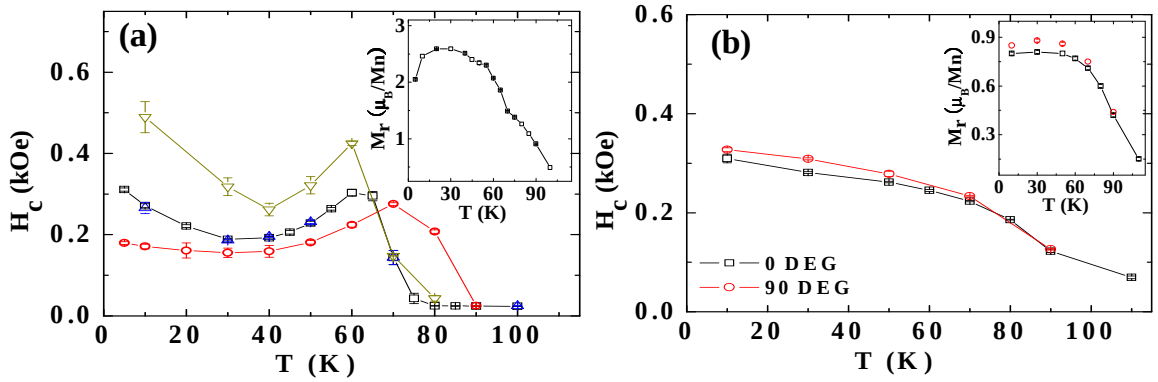

Figure 4-6. (a) $H_c(T)$ for a 20-nm-thick LPCMO thin film grown on NGO from ZFC $M(H)$ curves with H along [1$\bar{1}$0] NGO using linear background fitting (inverted triangle) and a 30-nm-thick LPCMO thin film grown on NGO from ZFC $M(H)$ curves with H along [1$\bar{1}$0] NGO using linear background fitting (square) and direct subtraction (triangle) and 10 kOe FC $M(H)$ curves with field along [1$\bar{1}$0] NGO using linear background fitting (circle). The inset shows M_r(T) for the 30-nm-thick LPCMO thin film grown on NGO from ZFC $M(H)$ curves with H along [1$\bar{1}$0] NGO using linear background fitting. (b) $H_c(T)$ for a 30-nm-thick LPCMO film grown on SLGO from ZFC $M(H)$ curves with H applied along two orthogonal in-plane directions. The inset shows M_r(T) for the 30-nm-thick LPCMO thin film grown on SLGO from ZFC $M(H)$ curves with H applied along two orthogonal in-plane directions.

Below 30 K down to 5 K, the coercive field increases again (Figure 4-6(a)). To explain this unexpected increase in H_c, we have to go back to Figure 4-3, which shows that below 30 K LPCMO is in the SPS state [3]. As a result, the size and distribution of the ferromagnetic regions remain constant below 30 K and the increase of coercive field may be due to the reduction of thermal energy in the multidomain ferromagnetic regions of constant size. To confirm this hypothesis we fit the $H_c(T)$ curve from 5 K to 30 K to the equation $H_c(T)/H_{c0} = [1-(T/b)^q]$, where b is related to the spin flip energy barrier at zero magnetic field, H_{c0} is the coercive field at 0K, and q is the exponent of temperature, since it has been observed that the coercive fields of multidomain nanoparticles show a $T^{2/3}$ dependence [78, 79]. From fitting, it is estimated that q

is 0.68 $\pm$ 0.02 ($H_{c0} \approx 360$ Oe and $a = E_0/k_B \approx 88$ K) which confirms our hypothesis. The magnetic behavior of LPCMO in the low temperature region is also different from spin glass materials such as the CuMn system, where displaced hysteresis loops are observed after FC [80]. When we measured magnetic hysteresis loops after FC to 10 K in a magnetic field of 10 kOe, we could not observe any significant difference in the positive and negative coercive fields (data not shown). When FC is carried out in a field of 10 kOe (which is higher than all the coercive fields measured at different temperatures), it increases the FMM phase of the thin film so that the domain transition sets in at the higher temperature of 70 K (Figure 4-6(a)). In the LPCMO//SLGO films, all the magnetic quantities (H_c, M_r) show gradual increase as the temperature is reduced (Figure 4-6(b)). In particular, the magnetic domain transition observed in LPCMO//NGO films was not observed in the LPCMO//SLGO films. We thus conclude that the domain transition is due to substrate induced anisotropic in-plane stress coupled with phase coexistence in LPCMO thin films. We now present a detailed description of the magnetic anisotropy in LPCMO thin films.

4.2.4 Strain Induced Magnetic Anisotropy

We measured $M(H)$ curves of the LPCMO//NGO films along two perpendicular in-plane directions *viz.*, [1$\bar{1}$0] and [001] directions of the NGO substrates to check for possible strain induced magnetic anisotropy. From Figure 4-7(a), it is clear that the [001] NGO direction is the magnetic hard axis, while the [1$\bar{1}$0] NGO direction is the magnetic easy axis of the LPCMO//NGO films. As discussed earlier, when the magnetic field is applied along the easy axis the films show magnetic hysteresis loops below T_C. Since we measured approximately square shaped thin films (6 mm $\times$ 6 mm) which are chemically in a single phase, we could neglect the in-plane shape anisotropy from the film geometry. Also, when we measured $(La_{1-y}Pr_y)_{1-x}Ca_xMnO_3$ (x = 0.33 and y = 0.5) thin films on (110) NGO at 10 K, in fully ferromagnetic state, we still observed an in-plane magnetic anisotropy similar to the anisotropy of ferromagnetic $La_{0.77}Ca_{0.33}MnO_3$

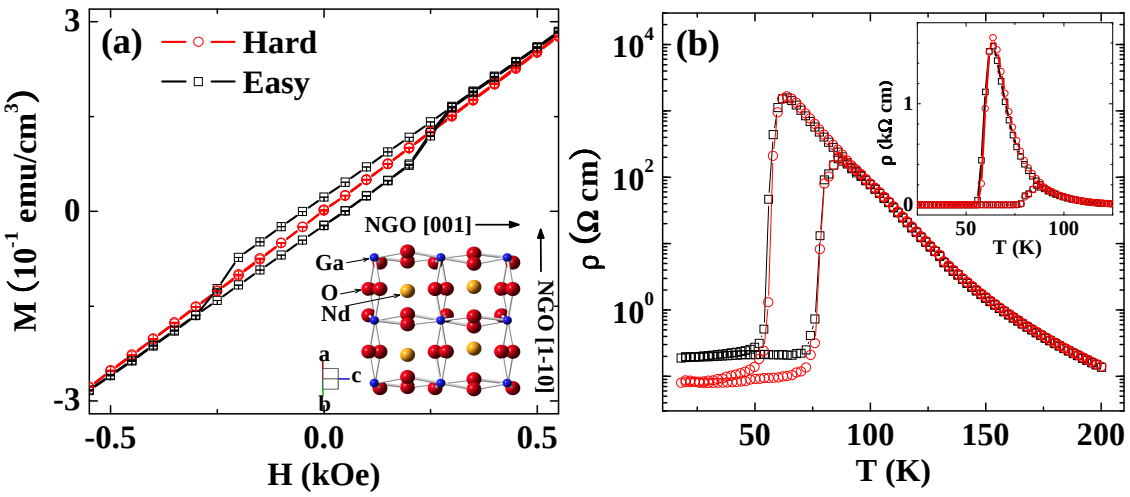

Figure 4-7. (a) $M(H)$ of the 30-nm-thick LPCMO thin film grown on NGO with H along hard axis (circle) and easy axis (square) at 60 K. The inset shows atomic structure of NGO ($d_{1\bar{1}0}$ = 3.863 Å and d_{001} = 3.854 Å) [18]. (b) $\rho(T)$ measured along the hard axis (circle) and easy axis (square). The inset shows $\rho(T)$ in a linear scale.

thin films grown on (001) NGO [3, 67]. Thus, we could neglect the shape anisotropy due to elongated or stripe-like FMM regions [27, 81]. Hence, there are two possible interpretations of this magnetic anisotropy *viz.*, magnetocrystalline anisotropy or stress anisotropy [75]. Murakami *et al.* suggested that magnetocrystalline anisotropy leads to a domain transition in single crystal $(La_{1-y}Pr_y)_{1-x}Ca_xMnO_3$ [27]. Hence, magnetocrystalline anisotropy could also be the reason behind the observed in-plane magnetic anisotropy in our thin films. However, stress anisotropy could also play a critical role due to the different in-plane lattice constants of (110) NGO substrates. Along the [001] NGO direction, the tensile strain on LPCMO is 0.26% and along the [$1\bar{1}0$] NGO direction the tensile strain is 0.49% (inset of Figure 4-7(a)). The magnetic easy axis was observed to be along the direction with larger tensile strain i.e. the [$1\bar{1}0$] NGO direction (Figure 4-7(a)). This result is consistent with experiments on $La_{0.67}Sr_{0.33}MnO_3$ thin films grown under anisotropic tensile stress [57]. Boschker *et al.* showed that the in-plane magnetization is due to the compression of the MnO_6 octahedra in the out-of-plane

direction caused by tensile strain and the uniaxial anisotropy is due to difference in in-plane tensile strains causing further distortion of the octahedra [57]. Through this mechanism it is possible that if a substrate has different in-plane lattice constants, the magnetic easy axis will be along the direction with higher tensile strain. To distinguish between these two possible origins of magnetic anisotropy, we measured the magnetic anisotropy of LPCMO thin films grown on SLGO substrates which exert negligible stress on LPCMO and there is no in-plane anisotropic stress. From Figure 4-4 and Figure 4-6(b) it is clear that the magnetic hysteresis loops, $M(T)$, $H_c(T)$, and $M_r(T)$ of the 30 nm-thick LPCMO//SLGO thin film are almost identical for applied fields along the [100] and [010] directions of the SLGO substrates, at all temperatures. So our observation is that the LPCMO//SLGO film has negligible in-plane magnetic anisotropy, while there is clear magnetic anisotropy in the LPCMO//NGO films. Hence, the main reason for magnetic anisotropy in the LPCMO thin films is the anisotropic stress exerted by the substrate.

While we observed clear in-plane strain induced magnetic anisotropy, we did not observe any significant in-plane anisotropy in the transport properties (Figure 4-7(b)) (we did observe a lower resistivity at low temperatures along the magnetic hard axis but that was due to a higher electric field in that direction since the distance between the voltage leads was shorter along the [001] direction [3]). In fact, in a linear scale (inset of Figure 4-7(b)) the $\rho(T)$ behavior appears identical in the two in-plane directions. The T_{IM} is 60 K in both directions and at that temperature the resistivity anisotropy ($\left|\frac{\rho_{NGO[001]}-\rho_{NGO[1\bar{1}0]}}{\rho_{NGO[1\bar{1}0]}}\right| \times 100$) is $\approx$ 15%. Thus, we believe that anisotropic in-plane properties due to substrate induced strain can be clearly observed in magnetic measurements, but not in transport measurements. Our observation is in contrast to Ward *et al.* who suggested that the difference in T_{IM} and maximum ρ observed along two perpendicular in-plane directions of LPCMO thin films grown on NGO substrates was due to anisotropic strain and was maximized as magnetic field was

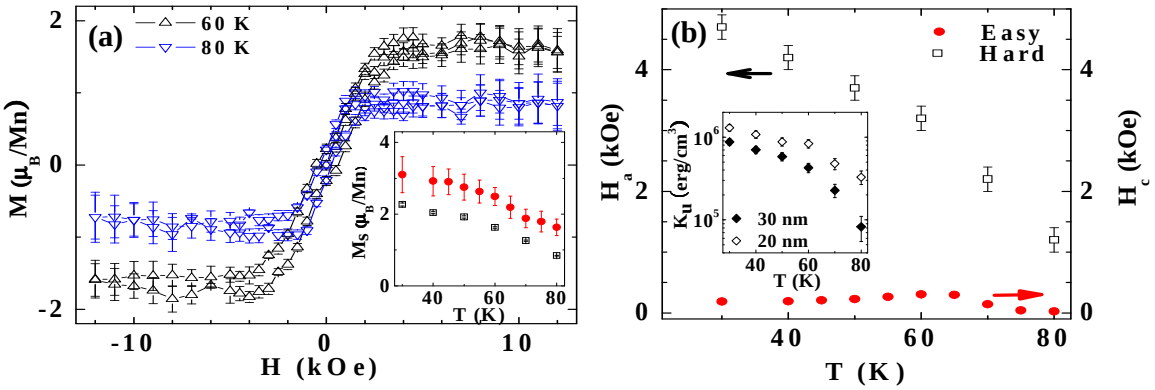

Figure 4-8. (a) $M(H)$ curves of the 30-nm-thick LPCMO thin film grown on NGO with H along [001] NGO obtained using linear background fitting. The inset shows M_s as a function of temperature for the easy axis (circle) and hard axis (square) directions. (b) H_a (square) and H_c (circle) as a function of temperature. The inset shows K_u of the 20-nm-thick (unfilled diamond) and the 30-nm-thick (filled diamond) thin films as a function of temperature.

lowered [53]. Such a strain induced resistivity anisotropy has also been predicted theoretically [82]. It is possible that such resistivity anisotropy can only be clearly observed when the resisitivity measurements are taken at the scale of phase separation i.e. in the micrometer scale, and requires further investigation.

Next, we ramped the magnetic field up to 12 kOe on the LPCMO//NGO films along the [001] NGO direction i.e. the hard axis. The removal of the background signal was more difficult due to the lack of hysteresis in the $M(H)$ curves. The linear background fitting method was carried out for field values above 5 kOe, since the magnetic moment saturates at a higher field along the hard axis as shown in Figure 4-8. Saturation magnetization values along the hard axis direction were slightly lower than those along the easy axis at all temperatures (inset of Figure 4-8(a)). Since the LPCMO//NGO films show strong in-plane uniaxial anisotropy, we could estimate the uniaxial anisotropic constant (K_u) as a function of temperature in the 20 nm-thick and the 30 nm-thick LPCMO films using saturation magnetization (M_s) values, anisotropic fields (H_a) and the relation $K_u = M_s H_a/2$ (inset of Figure 4-8(b)) [75]. As expected, the thinner film

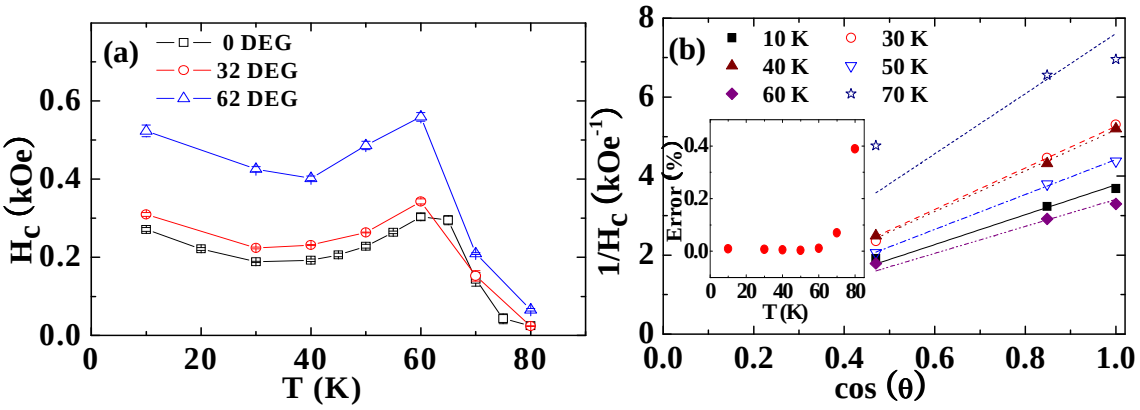

Figure 4-9. (a) $H_c(T)$ behavior of the 30 nm-thick LPCMO film grown on NGO for three different values of θ, where θ is the angle between the applied field H and the easy axis. (b) H_c^{-1} as a function of cos(θ) at different temperatures. The inset shows standard error of the slope of the H_c^{-1} vs. cos(θ) graph at each temperature

shows higher K_u values due to larger substrate induced strain effects. These values are comparable to that of $La_{0.7}Ca_{0.3}MnO_3$ thin films on NGO substrates (3.6×10^5 erg/cm^3 at 77 K) and higher than that of a $La_{0.7}Sr_{0.3}MnO_3$ thin film on $SrTiO_3$ (8.4×10^4 erg/cm^3 at room temperature) [67, 83]. As the temperature was reduced, a gradual monotonic increase of the uniaxial anisotropic constants, saturation magnetization values, and anisotropic fields was observed unlike the non-monotonic behavior of the coercive fields due to the magnetic domain transition. Using the uniaxial anisotropic constant at 60 K and exchange stiffness value (A) from Lorentz microscopy, we calculated the critical diameter for domain transition assuming a spherical domain [27, 84]. We obtain a value of 85 nm for the critical radius (r_c).

When the anisotropic field and coercive field are compared, differences not only in trends from temperature variation but also in magnitudes can be easily identified (Figure 4-8(b)). The anisotropic fields are larger by an order of magnitude or more than the coercive fields along the easy axis. This difference in magnitude implies that Stoner & Wohlfarth's magnetic reversal mechanism may not be valid [85, 86]. There are two main mechanisms for magnetic switching behavior *viz.*, Stoner & Wohlfarth's

coherent rotation model and a nucleation & propagation mechanism [75]. A direct way to check which model is applicable in our case is a measurement of coercive fields as a function of the angle between the magnetic easy axis of sample and external magnetic fields, since each model predicts a specific behavior. The nucleation & propagation mechanism leads to the Kondorsky law, ($H_c(\theta) = H_c(0)/\cos(\theta)$) [85, 87, 88]. We set [$1\bar{1}0$] NGO (easy axis) as θ = 0° and [001] NGO (hard axis) as θ = 90°. $M(H)$ curves were taken at two intermediate angles, θ = 32° ± 2° and θ = 62° ± 2°. Figure 4-9(a) shows coercive fields as a function of temperature for three different angles. It is clear that the coercive field increases with the angle θ between the easy axis and the applied magnetic field. When the inverse of coercive fields is plotted as a function of $\cos(\theta)$, the Kondorsky law is obeyed between 10 K and 60 K (Figure 4-9(b)). This behavior is also observed in other manganite systems grown on artificially miscut substrates [89]. At the higher temperatures of 70 K and 80K (data not shown for 80 K), the Kondorsky law is not obeyed (inset of Figure 4-9(b)). We believe that this deviation from Kondorsky law may be due to the spatial motion of the FMM, AFM-COI, and PMI phases in the FPS state and possible contribution of other reversal mechanisms [3].

4.3 Summary

In-plane anisotropic stress leads to uniaxial magnetic anisotropy in manganite thin films. We have shown that when such magnetic anisotropy is induced in phase separated manganites it leads to a single domain to multidomain transition as a function of temperature. The domain transition is similar to that observed in ferromagnetic fine particles as a function of particle size. In phase separated manganites the size of the ferromagnetic metallic regions embedded in a non-ferromagnetic (charge-ordered antiferromagnetic or paramagnetic) matrix increases as the temperature is decreased. Due to the stress induced uniaxial magnetic anisotropy the increase in size of the ferromagnetic regions results in the temperature dependent domain transition. The variation of the coercive field with temperature is a signature of the domain transition.

The temperature dependence of the coercive field is a feature which could make it possible to use manganites as cryogenic magnetic memory, since magnetic information can be written at a temperature with low coercive field and stored at a lower temperature with higher coercive field.

CHAPTER 5
ANISOTROPIC TRANSPORT IN LPCMO THIN FILMS

The interface region between two perovskite materials is a subject of recent interest since this region has properties not observed in the bulk form of either of the constituent materials [90–93]. The most well-known system is the interface between the insulators $LaAlO_3$ (LAO) and $SrTiO_3$ (STO) which becomes metallic and sometimes even superconducting, possibly due to charge transfer between the two materials. The charge transfer occurs to avoid a ”polar catastrophe” in ultra-thin (few monolayers) films of the polar perovskite LAO grown on the non-polar perovskite STO [91]. Recent developments in pulsed laser deposition (PLD) thin film growth technology such as in-situ high pressure reflection high energy electron diffraction (RHEED), have enabled researchers to perform such experiments by growing oxides thin films one atomic layer at a time [94]. Such high level of control even allows selection of the top termination layer of the thin film. While we do not have an in-situ RHEED in our PLD apparatus, we have been able to verify the high quality of our thin film interfaces using post-deposition techniques such as cross section transmission electron microscopy (TEM) and x-ray reflectivity (XRR). We are interested in studying the interface between phase separated LPCMO and NGO because the role of magnetic ions such as Mn and strain at the interface is still poorly understood. When we started research on this particular topic, our intent was to study the influence of strain and magnetism on the fluid and static phase separation at and near the interface. Hence, our experiments have been focused on two different categories: (1) effect of an electric field on phase separation at the interface and (2) the combined effect of electric and magnetic fields at the interface. We have thus observed signatures of a unique version of the magnetoelectric effect at the interface of phase separated manganites.

5.1 LPCMO (*y* = 0.6) Thin Films

LPCMO thin films (*y* = 0.6) were characterized using TEM. Cross sectional TEM can provide important information, *viz.* thickness of a thin film, crystallographic relation between a thin film and a substrate, and variation in composition of a thin film along film normal. In order to prepare a sample for cross sectional TEM, dual beam focus ion beam (FIB) milling was used. Dual beam FIB uses energetic Gallium (Ga) ions for fast processing and an electron beam as imaging probe to minimize damage by Ga ions. Carbon layers were coated on LPCMO thin films to reduce charging. Charging results in failure of imaging. On top of carbon coating, 12 μm (length) $\times$ 2 μm (width) $\times$ 1.5 μm (thickness) of Platinum (Pt) was deposited in the FIB to protect surfaces of thin films. After depositing Pt, series of milling operations with different ion beam currents were conducted to create a slab of sample consisting of layers of Pt, carbon, LPCMO, and NGO. The process consists of creating trenches, thinning, undercutting, further thinning, creating a wedge, and finally cutting the side walls. Just before final thinning, thickness of the slab is approximately 150 nm. The wedge shaped slab, which was made with one side is thinner than the other, increased the chance to observe TEM images in electron transparent region (Figure 5-1 (a)).

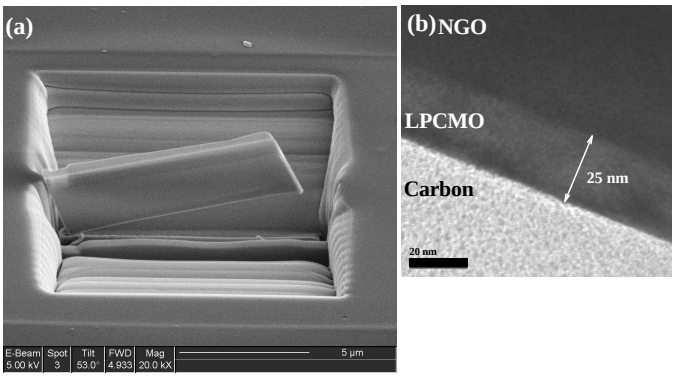

Figure 5-1. (a)Scanning electron microscope image of LPCMO (y = 0.6) thin film on NGO prepared for transmission electron microscopy (TEM). (b)TEM image of LPCMO//NGO (300 $\times$)

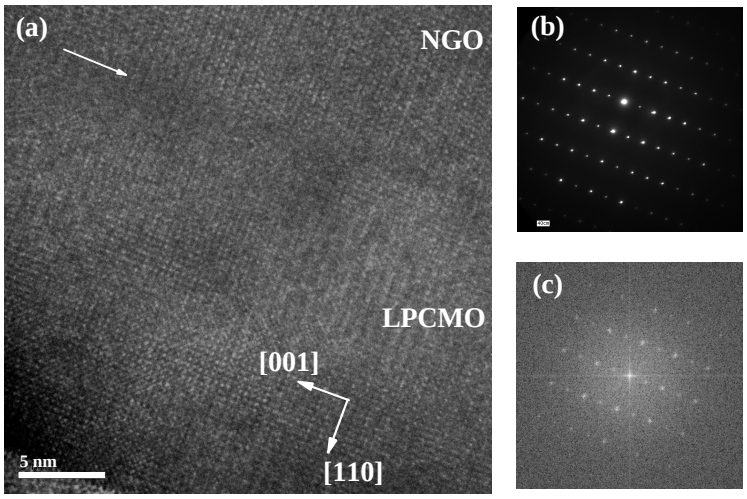

Figure 5-2. (a) TEM image of LPCMO (y = 0.6) thin film on NGO (600k $\times$). An arrow indicates possible interface between film and substrate. (b) Selected area diffraction (SAD) pattern of LPCMO and NGO (300 $\times$). (c) Fast flourier transformation (FFT) of LPCMO region.

In low magnification (Figure 5-1 (b)), clear distinction of each layer was seen (carbon, LPCMO, and NGO). Also, thickness of the LPCMO thin film is observed t be about 25 nm. The thickness from AFM measurement was 30 nm [68]. In high magnification, we observed clear lattice images. Due to extensive bombarding of Ga ions during TEM sample preparation, non-uniform surfaces and/or amorphous layers were created, so that some portions do not show clear lattice images (Figure 5-2 (a)). From intensity profile of lattices, the lattice constant is about 0.4 nm. However, clear interface has not been observed either due to amorphous layer or close lattice matching between the thin film and the substrate. We also performed selected area diffraction (SAD), which covered all areas including carbon, LPCMO, and NGO layers (Figure 5-2 (b)). Fast fourier transformation (FFT) of LPCMO region has same pattern as SAD results (Figure 5-2 (c)). This indicates that the film and the substrate have specific orientation relations, *viz.* LPCMO [110] // NGO [110] and LPCMO [001]//NGO[001] [95].

We also performed x-ray energy dispersive spectroscopy (EDX) in TEM apparatus. This option uses emission of characteristic energy from elements in the sample. The beam spot size is theoretically less than 1 nm and practically a few nm. The EDX

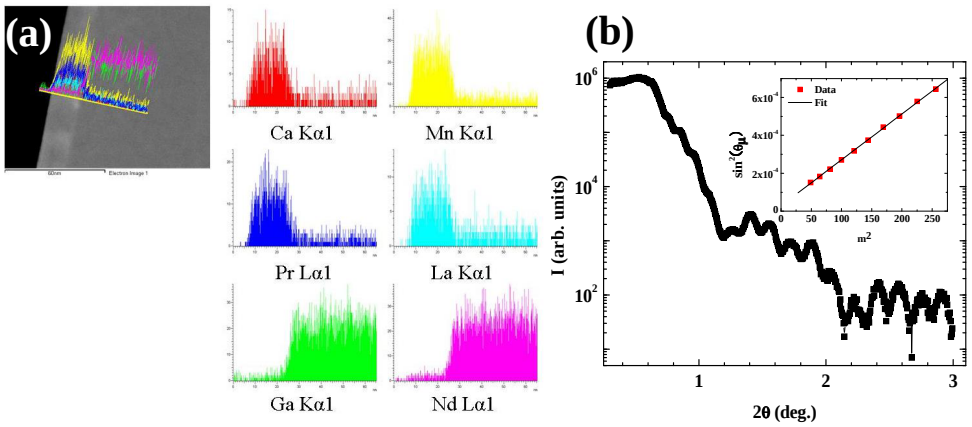

Figure 5-3. (a) X-ray energy dispersive spectroscopy on a LPCMO thin film. Depth profile of main elements in the thin film and the substrate are displayed. (b) X-ray reflectivity of a 60-nm-thick thin film. Inset shows plot $sin^2(\alpha_\mu)$ vs. μ^2.

in TEM can thus be used as a local probe of chemical composition. EDX line scan shows chemically sharp interface between LPCMO and NGO (Figure 5-3 (a)). We also performed spot analysis to check for small variations of chemical composition. We performed this spot analysis of three different spots: two spots in LPCMO region and a spot in NGO region. One spot in LPCMO is the middle of LPCMO layer, and another spot in LPCMO is near the interface between LPCMO and NGO. The spot in NGO is just below the interface. In the two spots in LPCMO, we do not detect significant change of composition (Table 5-1, 5-2, and 5-3). We also observed abundance of Nd and Ga in NGO region, so that it is unlikely that there is intermixing at the interface between thin film and substrate.

Table 5-1. Ideal composition and ratio of LPCMO

La	Pr	Ca	Mn	La/Mn	Pr/Mn	Ca/Mn	Pr/La	Sum
0.268	0.402	0.33	1	0.268	0.402	0.33	1.5	1

Table 5-2. Composition of LPCMO at the middle of the thin films

La	Pr	Ca	Mn	La/Mn	Pr/Mn	Ca/Mn	Pr/La	Sum
7.16	9.91	6.83	21.73	0.33	0.42	0.31	1.38	1.10

Table 5-3. Composition of LPCMO near the interface

La	Pr	Ca	Mn	La/Mn	Pr/Mn	Ca/Mn	Pr/La	Sum
6.58	9.16	7.05	21.75	0.30	0.42	0.32	1.39	1.05

We measured x-ray reflectivity (XRR) of a 60-nm-thick LPCMO (y = 0.6) thin film (Figure 5-3 (c)). XRR can give layer thickness, density, and roughness [96]. Initially, our aim was to find the thickness of our thin film. XRR result shows two different types of Kiessig fringes, which indicates that our film is an electronically distinct double layer system. Recently, it was reported that even high quality $La_{1-x}Sr_xMnO_3$ thin films can have electronically distinct double layers from various spectroscopic methods [97]. To find the thickness, we used the following formula.

$$2t\sqrt{sin^2(\theta_\mu) - sin^2(\theta_c)} = \mu\lambda, \tag{5–1}$$

where t is thickness, μ is an integer, θ_c is the critical angle for total external reflection in the layer, λ is the wavelength of x-rays (λ = 1.541837 Å). We plotted $sin^2(\theta_\mu)$ vs. μ^2, then applied least square fitting (inset of Figure 5-3 (c)). We get 49.5 nm as the thickness from smaller oscillations. We estimate that an approximately 10-nm-thick layer is formed near the interface between the thin film and the substrate using the same method on the broader oscillations. This electronically distinct layer near the interface is consistent with polarized neutron reflectivity measurements on our thin films [98].

5.2 Electric Field Induced Anisotropic Transport

Near insulator-metal transition temperature, reduction of resistivity due to electric fields was reported in the LPCMO system [3, 99]. Two possible models were proposed: dielectric breakdown model and dielectrophoresis model [100, 101] (Figure 5-4). Dielectric breakdown model suggests an electric field induced conversion of the insulating phase to metallic phase, while dielectrophoresis model proposes an electric field induced realignment of the metallic phase along the electric field direction. In LPCMO, the dielectric breakdown model predicts an isotropic decrease of resistivity

and increase of magnetization, since the reduction in the amount of the insulating phases should result in an increase of FMM phase. However, dielectrophoresis model predicts no change in magnetization and anisotropic transport, in which resistivity along electric field decreases while resistivity perpendicular to electric field increases. We fabricated 100 μm $\times$ 250 μm cross structures out of 20-nm-thick LPCMO thin films. Micrometer-scale phase separation is seen in LPCMO, so anisotropic resistance measurements need to account for non-uniform equipotentials. One way to reduce the effect of non-uniform equipotentials is to perform the experiments on a sub-millimeter cross structure. By defining transverse and longitudinal directions in the cross structure, we can clearly detect possible anisotropic transport. 5-5 (a) shows optical microscopy image of actual cross structure of LPCMO. This structure was created by photolithography and wet etching. Also, Figure 5-5 (b) shows the definition of transverse direction (EG leg) and longitudinal direction (FH leg). Along longitudinal direction (FH), high dc voltage was applied. It is noted that both legs experience different substrate stresses, since each leg is parallels to each crystallographic direction of NGO, e.g. $(1\bar{1}0)$ and (001).

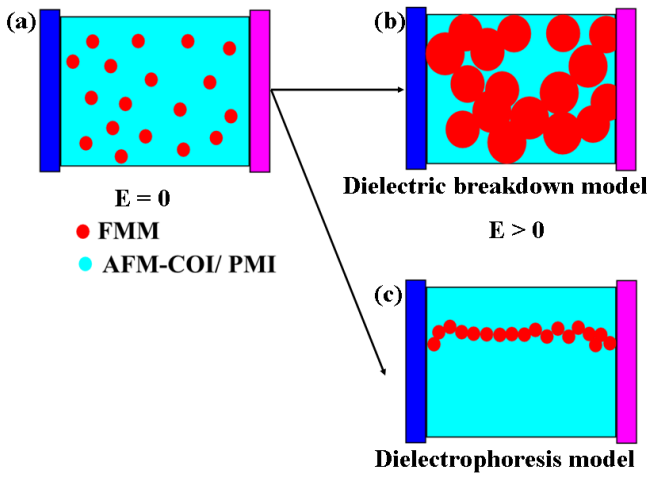

Figure 5-4. Proposed models for colossal electroresistance (CER) effect. (a) State with no electric fields. Under electric fields, (b) Isotropic conduction due to dielectric breakdown model and (c) Anisotropic conduction due to dielectrophoresis model.

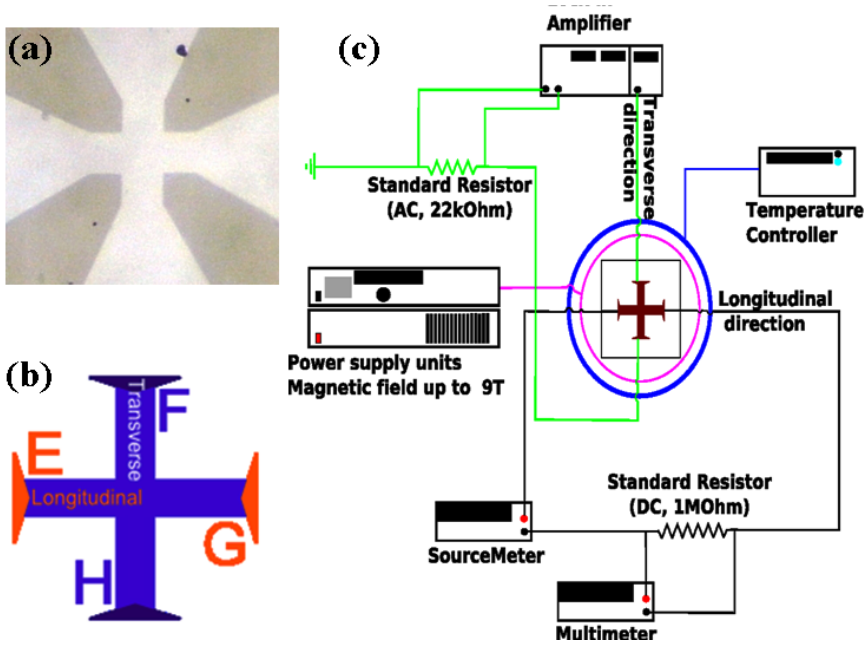

Figure 5-5. (a) Optical microscopy image of 100 μm $\times$ 250 μm cross structure of LPCMO thin films. (b) Schematic diagram of the cross structure (c) sequential transport measurements set-up.

We performed resistance measurements of the both legs on the cross structure (EG and FH) using voltage sourced resistance measurements. Figure 5-6 (a) shows R(T) of both legs have similar features. Especially, the transition temperatures are same. In order to detect transverse resistance under high electric fields, we used a small ac voltage with low frequency. Small driving voltage (less then 1 V_{rms}) reduces possible electric field effects along transverse direction. AC source can also reduce the effect of irregular equipotential. Low frequencies (f=5.657 Hz and 18.647 Hz) were used to avoid capacitive effects. The dc- and ac- transport measurements match each other. At low voltage (up to 5 V), we could not observe colossal electroresistance (CER) effects (Figure 5-6 (b)). To measure the CER effect at high voltage, we measured dc resistance as a function of temperature with 5 V and 60 V along EG. This shows clear breakdown of resistance along the longitudinal direction near insulator-metal transition (Inset of Figure 5-6 (b)).

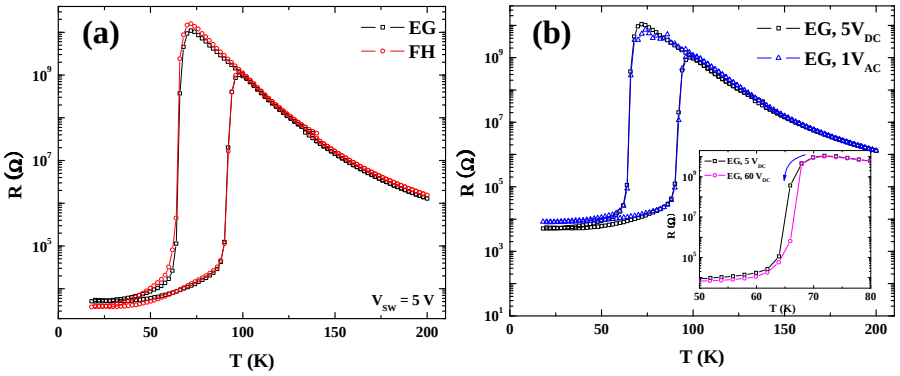

Figure 5-6. (a) Resistance as a function of temperature (R(T)) of both legs. (b) R(T) by dc source and ac source along leg EG. Inset: R(T) along leg EG with two different dc voltages.

We performed two different isothermal sequential transport measurements along longitudinal and transverse directions (EG and FH): resistance as a function of elapsed time (R(t)) and resistance as a function of applied voltage (R(V)) (Figure 5-5 (c) and 5-7 (a)). ”Sequential” means we put time gap (t_d) between longitudinal and transverse measurements to minimize an interference effect of transverse ac voltage on longitudinal resistance measurements. After each isothermal transport measurement, we warm up the LPCMO above insulator to metal transition temperature (130 K), since the electric field effect on LPCMO is irreversible [3].

First, we measured R(t) near insulator-metal transition temperature (T_{IM} = 65 K), since we can possibly monitor dynamics of either dieletrophoretic motion or dielectric breakdown motion in time domain. All the measurements were done at 69.5 K. For figure 5-7 (b), 45 V_{dc} was applied along longitudinal direction, and 1.0 V_{rms} (f = 5.657 Hz) was applied only for 1 second (t_1 = 0.80 s, t_2 = 0.18 s, and t_d = 0.02 s) out of each cycle of the measurements (2 seconds). We observed longitudinal resistance showed smaller oscillation behavior at the beginning. After drop of resistance in transverse direction, huge modulation of longitudinal resistance starts. The transverse resistance then starts to increase again (figure 5-7 (b)). We further optimized t_1, t_2, and t_d to minimize oscillating feature, since the oscillation of longitudinal resistance is only

observed at which ac voltage is on (data not shown). This reflects it may not be from manganites but from measurement scheme. We could remove the oscillation feature in following condition (t_1 = 2 s, t_2 = 1 s, and t_d = 0.50 s) (figure 5-7 (c)). 25 V_{dc} was applied along longitudinal direction, and 0.5 V_{rms} (f = 5.657 Hz) was applied along transverse direction at 69.5 K. Both transport data are qualitatively similar except oscillating feature in figure 5-7 (b). In figure 5-7 (c), breakdown of the transverse resistance is shown after about 1800 seconds, while longitudinal resistance increases. About 900 seconds later, huge longitudinal resistance drop was observed, while transverse resistance increases. The first breakdown along transverse direction is mainly caused by transverse ac voltage, which creates non-uniform electric field for dielectrophoresis. The second breakdown along longitudinal direction is mainly driven by dc-voltage. Since phase separated manganites itself can create non-uniform electric field, the dc-voltage assists dielectrophoresis along longitudinal direction [101]. In fact, we could control breakdown time by changing ac voltage and dc-voltage. These two dielectrophoretic motions are clear signature spatial realignment of metallic phase in the sample. It is noted that we observed, when dc-voltage is applied along EG direction, longitudinal breakdown time is shorter (Figure 5-7 (d)). This shorter longitudinal breakdown time has been observed in several LPCMO samples, when longitudinal direction is magnetic easy axis. Also the missing of transverse breakdown due to dielectrophoresis(data not shown), when dc voltage is along magnetic easy axis, may be indication of elongated electric regions along the easy axis.

Second, we performed isothermal R(V) measurements (Figure 5-8). We measured both resistances, while sweeping dc voltage along longitudinal direction (EG). We put 0.5 s as t_d. We observed two to three orders of magnitude drop in longitudinal resistance, while we only observed equal or less than an order of magnitude drop in transverse resistance (Figure 5-8). To clarify our observation, we calculate anisotropic resistance ratio (ARR (%) $\equiv \frac{R_{EG}-R_{FH}}{R_{EG}} \times 100$). This ARR showed clear decrease of

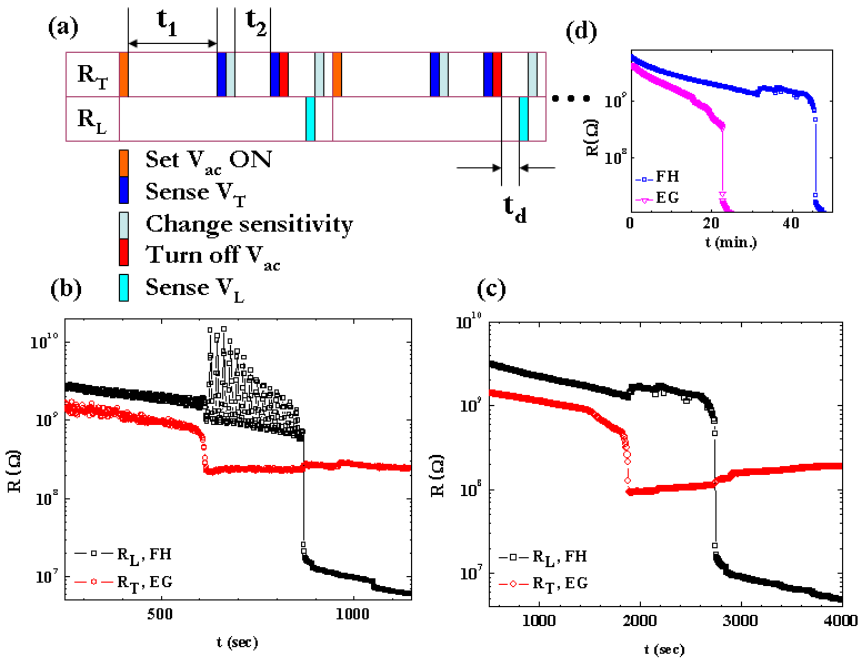

Figure 5-7. (a) Scheme of sequential measurements. Isothermal sequential resistances as a function of elapsed time (R(t)). (a) R(t)s at 69.5 K under 45 V_{dc} as an applied voltage and alternating 1.0 V_{rms} perpendicular to the applied voltage. (b) R(t)s at 69.5 K and under 25 V_{dc} and alternating 0.5 V_{rms}. (d) R(t) along longitudinal direction. (d) Longitudinal R(t) along EG and FH. 25 V_{dc} was applied.

resistance along EG. This anisotropic transport in R(V) supports the dielectrophoresis model. However, we could not detect clear upturn of transverse resistance, which was theoretically predicted [101].

5.3 Effects of Electric Fields and Strains on Magnetotransport

We have found that LPCMO thin films on (110) NGO substrates show stress induced magnetic anisotropy. This anisotropy causes single domain to multidomain transition in phase separated LPCMO thin films, but does not cause in-plane anisotropic transport in zero magnetic field [8]. Also, we observe that electric fields affect transport properties of these LPCMO thin films as discussed in the previous section. In this section, we will show what the effects of strain and electric fields are on magnetotransport properties.

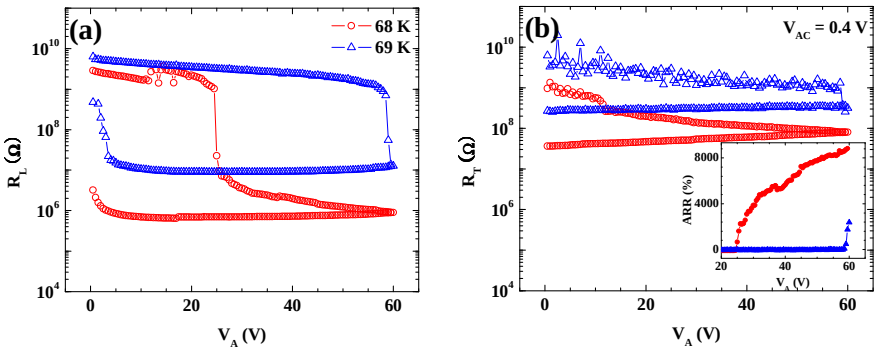

Figure 5-8. Isothermal sequential resistance as a function of applied voltage (R(V)) measurements. (a) R(V) along applied fields (EG). (b) R(V) perpendicular to applied fields (FH). Inset shows anisotropic resistance ratio at 68 K and 69 K.

We first fabricate a 100 μm $\times$ 250 μm cross structure of LPCMO from a 30-nm-thick thin film. We then checked resistance as a function of temperature (R(T)) without magnetic fields. In contrast to experimental results from Ward *et al.*, we observed no difference in R(T) along two different directions: [1$\bar{1}$0] and [001], which are the magnetic easy and hard axes, respectively [8, 53] (Figure 5-10). The T_{IM} are about 68 K for both directions. We have defined T_{IM} as maximum resistance (dR/dT = 0) while cooling to compare this T_{IM} with T_{IM} under magnetic fields.

T_{IM} under magnetic fields (H = 8 T) is moved up to a higher temperature of 148 K, when the magnetic field is in out-of-plane direction (Figure 5-10 (b) and Figure 5-11 (a)). This increase of T_{IM} is due to melting of insulating phases in magnetic fields [1, 25, 102]. When magnetic field is in plane, T_{IM} is moved up further in between 151 K and 159 K (Figure 5-10 (c)-(d) and Figure 5-11 (b)-(c)). Spread of T_{IM} for in-plane magnetic fields will be explained in the section 5.3.2. We still observed small hysteresis showing 2 K difference in T_{IM} and T_{MI} in all configuration which indicated that the LPCMO thin film is still in phase coexistence state. The possible reasons of increase in T_{IM} along in-plane direction are the combined effect of demagnetization factor, phase coexistence, and evolution of each phase. At a glance, this increase of critical temperature and lower

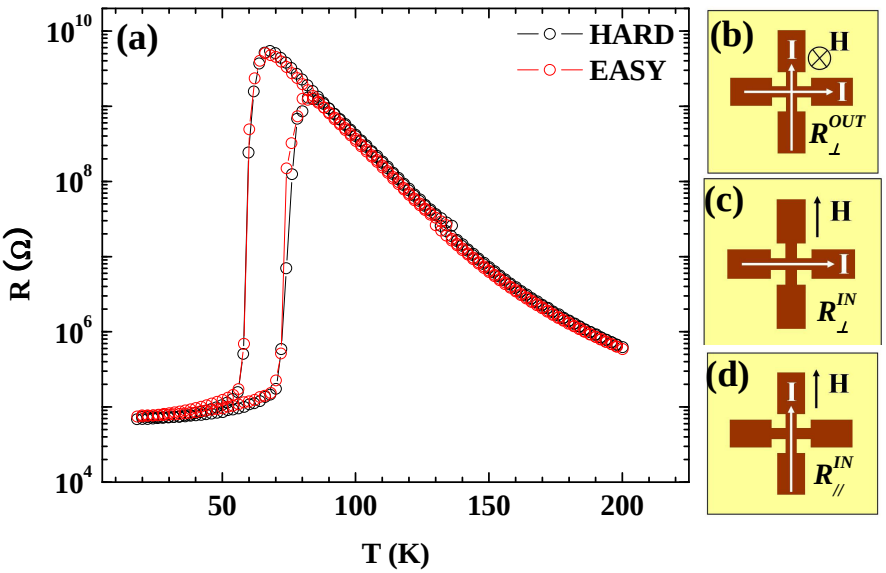

Figure 5-9. (a) Zero field R(T) of LPCMO thin films. Schematic diagrams of different magnetotransport: (b) Magnetic fields (H) is out of plane and perpendicular to currents. (c) H is in-plane but perpendicular to currents. (d) H is in-plane and parallel to currents.

breakdown magnetic fields along in-plane could be explained by demagnetization factor from film geometry, since actual fields inside the sample is much higher than for in-plane case for the same applied magnetic field [75]. However, demagnetization factor for an out-of-plane field is nearly 1 in homogeneous magnetic thin films. Thus, it is obviously not true for our case because we deal with phase separated manganite thin films grown under anisotropic tensile strains. Also, it was reported that substrate strains can control magnetic easy axis. Especially, the $La_{0.67}Sr_{0.33}MnO_3$ is grown on $LaAlO_3$, easy axis of the film is along out-of-plane direction [103–105]. In our case, the LPCMO thin films experience in-plane tensile strains, so that we can rule out that possibility for the substrate strains effects on anisotropic magnetotransport. We believe this anisotropic magnetotransports are due to magnetic phase separation and evolution of each phases in temperature. Breakdown magnetic fields (H_B) are determined from $dR/dH \approx 0$ at 60 K (Figure 5-12). Then, we found that out-of-plane H_B (1.17 T) is four times larger than in-plane $H_{B,hard}$ (0.29 T) at 60 K, while out-of-plane H_B (5.23 T) is only 1.03 times larger

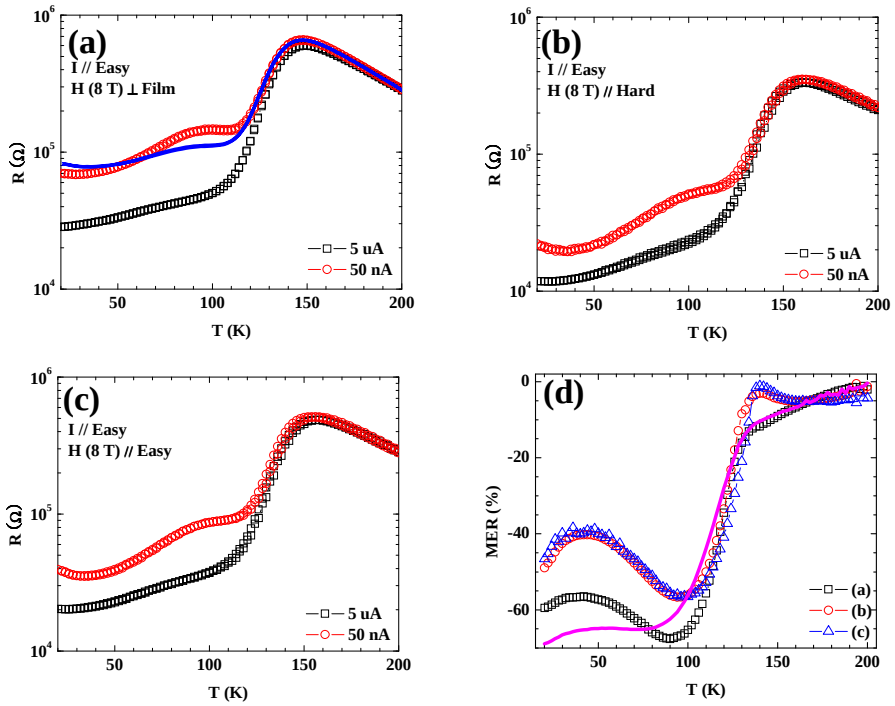

Figure 5-10. Current effects on magnetotransport, when current (I) is along magnetic easy axis and (a) magnetic field (H) is out of plane (Blue line is magnetoresistance in hard axis), (b) H is along hard axis (in-plane), (c) H is along easy axis (in-plane). (d) Magnetoelectric resistance (MER) of (a), (b), and (c). Magenta line is the MER, when I is along hard axis and H is along out-of-plane direction.

than in-plane $H_{B,hard}$ (4.03 T) at 100 K, when current is along magnetic hard axis. This indicates, when FMM increases in cooling, demagnetization factor from FMM shape comes into play.

5.3.1 Current Effects on Magnetotransport

Since electric field effects were observed, we measured magnetoresistance with different currents about three different magnetic field directions (Figure 5-10 (b)-(d)) [3]. It is noted that we observed a hump after insulator-metal transition at around 80 K, and upturn of resistance at low temperature (30 K) with low sensing current (50 nA). This upturn feature can be explained, since below 30 K the sample is entering the static phase separation (SPS) region. When we applied 5μA and measured magnetoresistance, the upturn and hump features disappeared. Also, significant

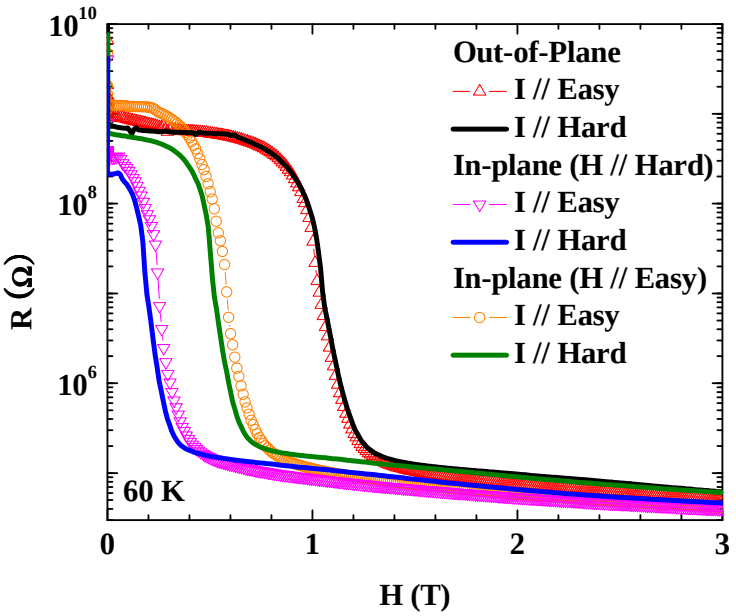

Figure 5-11. R(H) in three different magnetic field directions at 60 K. Solid lines is R(H) in current along hard axis.

decrease of resistance below T_{IM} was observed, which clearly indicates current effects in magnetoresistance. Magnetoelectric resistance (MER) is defined as relative change of magnetoresistances to low current magnetoresistance (MER(%) = $\frac{(R_{I,HIGH}-R_{I,LOW})}{R_{I,LOW}}$ $\times$ 100). When we calculated MER, we observed distinct increases of MER in two temperature ranges (Figure 5-11 (d)). We also calculated two other in-plane MER (Figure 5-11 (d)). In-plane MER is negligible above ferromagnetic Curie temperature (T_C), but out-of-plane MER linearly increase with decrease of temperature above T_C. Also, at low temperature, out-of-plane MER is more pronounced than in-plane MER.

5.3.2 Strain Effects on Magnetotransport

We have found several evidence of strain effects on magnetotransport, *viz.* MER(T), R(H), insulator-metal transition temperature in different magnetic field direction, and anisotropic magnetoresistance (AMR). We calculated MER(T) of two different current directions, while magnetic fields are parallel to film normal (Figure 5-11 (d)). The magenta line is the result from currents along hard axis. This clearly shows low temperature anisotropic MER due to substrate strain. We measure R(H) for three

different magnetic field directions. As expected, breakdown of resistance is seen at higher fields, when the magnetic field is along out-of-plane direction (Figure 5-12). For magnetic field along two in-plane directions, the breakdown of resistance requires higher magnetic field along magnetic easy axis. It does not depend on angle between currents and magnetic fields. However, as shown in Figure 5-12, after the breakdown, resistance along magnetic easy axis is always lower. It is noted Figure 5-11 (a) showed magnetoresistance (MR) along easy axis has lower resistance than MR along hard axis (blue line) in low temperature. This indicates substrate induced strain effects also contribute to magnetotransprot. We get insulator to metal transition temperature on two different current directions (Figure 5-13 (a)). In contrast to Ward *et al.*, effects of magnetic field direction outweigh effects of substrate strain effect. The T_{IM} for I along hard axis are always lower than T_{IM} for I along easy axis by 2 K. However, this is equivalent to sweeping temperature step.

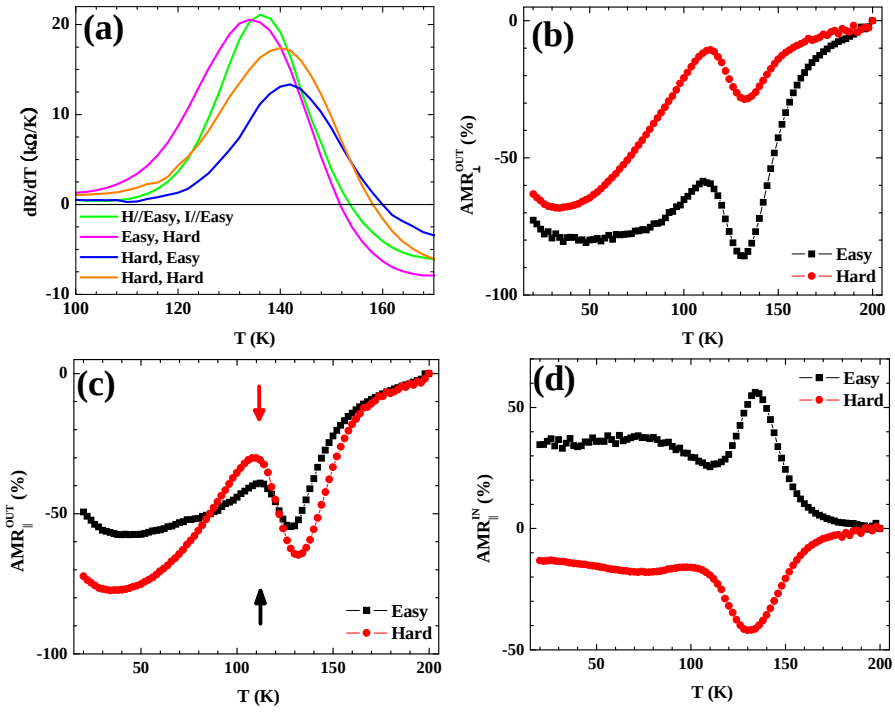

Figure 5-12. (a) dR/dT of R(T) under 8 T. Three different anisotropic magnetoresistances as a function of temperature: (b), (c), and (d).

Before we discuss AMR, we will define three different AMR, then we will discuss difference in them and strain effects in each AMR. The resistances are all normalized to the value at 200 K. The definition of $R_{\perp}^{OUT}$, $R_{\perp}^{IN}$, and $R_{//}^{IN}$ can be found at Figure 5-10 (b)-(d).

$$AMR_{//}^{IN}(\%) \equiv \frac{R_{//}^{IN} - R_{\perp}^{IN}}{R_{ave}} \times 100, where R_{ave} is \frac{1}{3}R_{//}^{IN} + \frac{2}{3}R_{\perp}^{IN}, \tag{5–2}$$

$$AMR_{//}^{OUT}(\%) \equiv \frac{R_{//}^{IN} - R_{\perp}^{OUT}}{R_{ave}} \times 100, where R_{ave} is \frac{1}{3}R_{//}^{IN} + \frac{2}{3}R_{\perp}^{OUT}, \tag{5–3}$$

$$AMR_{\perp}^{OUT}(\%) \equiv \frac{R_{\perp}^{IN} - R_{\perp}^{OUT}}{R_{ave}} \times 100, where R_{ave} is \frac{1}{3}R_{\perp}^{IN} + \frac{2}{3}R_{\perp}^{OUT}, \tag{5–4}$$

In all AMR measurements, we observed peaks at around 130 K. It is near to ferromagnetic Curie temperature (T_C) [8]. We clearly see AMR does not go to zero above T_C. This peak and non-zero AMR above T_C prevent to adopt the AMR theories for ferromagnetic metals, as it was argued in other hole doped manganite system [106]. In ferromagnetic metals above T_C, AMR goes to zero. In Figure 5-13 (b), the sign in $AMR_{\perp}^{OUT}$ can show type of substrate strain [107]. This AMR particularly remove contribution of Lorentz magnetoresitance (Lorentz MR), so that only contribution from magnetocrystalline anisotropy can be involved. It is noted our calculation has opposite sign from that of Li *et al.*, since we intentionally switch to $R_{//}^{IN}$-$R_{\perp}^{IN}$ from $R_{\perp}^{IN}$-$R_{//}^{IN}$ for this AMR calculation [107]. This way makes it possible to compare $AMR_{\perp}^{OUT}$ to $AMR_{//}^{OUT}$. Li *et al.* proposed thin films with different substrate strains, *viz.*, compressive strain and tensile strains, show different sign in $AMR_{\perp}^{OUT}$. In our case, both $AMR_{\perp}^{OUT}$ show negative sign, which manifest LPCMO is under in-plane tensile strains as expected. Also, The difference in magnitude of $AMR_{\perp}^{OUT}$ suggested more drastic changes along magnetic easy axis, where LPCMO is under more tensile strain. This axis also provides the longest Mn-O distance due higher tensile strains. Since $AMR_{\perp}^{OUT}$ does not include Lorentz MR, it is interesting to see effects of Lorentz MR. We measured $AMR_{//}^{OUT}$ (Figure 5-13 (c)). Between $AMR_{//}^{OUT}$ and $AMR_{\perp}^{OUT}$, only $AMR_{//}^{OUT}$ has no cancellation of Lorentz MR by measuring $R_{//}^{IN}$. Along easy axis, the $AMR_{//}^{OUT}$ is reduce to about half of

the values, while along hard axis the AMR is increase twice. Arrows indicate Lorentz MR affects differently in different directions.

We also measured in-plane AMR ($AMR^{IN}_{//}$) (Figure 5-13 (d)). In this case, both Lorentz and magnetocrystalline components contributes as well. We observed opposite sign of this in-plane AMR. This should be further investigated. It is noted these different signs have been observed in Ag doped $LaMnO_3$ thin film [108]. Infante *et al.* explained this with the theories for AMR of ferromagnetic metals. He/she concluded these differences are due to temperature dependent spin-orbit coupling and spin dependent scattering effects. This also could be due to different degrees of substrate strain effects, since Infante *et al.* grew thin films on (110) $SrTiO_3$ substrates, which provide anisotropic in-plane strains.

5.4 Summary

Proximity to an interface affects phase separation in manganite mainly through substrate induced strain. Electric and magnetic fields modulate the phase separation especially, in the fluid phase separated (FPS) state. Such modulation gives rise to an alternate form of the magnetoelectric effect. Theoretical simulation of a FPS state in electric and magnetic field will lead to a clear understanding of the phenomena.

CHAPTER 6
OPTIMIZATION OF BMO THIN FILMS AND PHYSICAL CHARACTERIZATION[1]

Multiferroic materials are unique in that they exhibit both ferromagnetism and ferroelectricity simultaneously. [31] Such materials may be used to fabricate devices such as magnetic tunnel junctions with electrically tunable tunneling magnetoresistance and multiple state memory elements.[12] The recent interest in multiferroics is fueled both by the potential device applications and questions about the underlying physical principles leading to multiferroism.[9, 10, 13–15] Bulk multiferroic materials are rare, possibly due to conflicting requirements for ferromagnetism (FM) and ferroelectricity (FE). $BiMnO_3$ is perhaps the most fundamental multiferroic and has been referred to as the "hydrogen atom" of multiferroics.[32] In $BiMnO_3$ (BMO), as in $BiFeO_3$, the $6s^2$ lone pair on the Bi-ion leads to the displacement of that ion from the centrosymmetric position at the A-site of a perovskite unit cell. The resultant distortion leads to an FM interaction between the Mn-ions at the B-site in $BiMnO_3$.[37, 38] In bulk form $BiMnO_3$ has been observed to be both FM and FE.[33] Polycrystalline $BiMnO_3$ can be grown under high pressure and within a very narrow range of growth conditions. While thin films of $BiMnO_3$ have been grown by various groups, few such films have shown magnetic properties similar to bulk $BiMnO_3$ and high enough resistivities i.e. low leakage currents to allow clear measurement of FE properties.[109–111] A possible reason for the low resistivities of $BiMnO_3$ thin films is the substrate induced strain which exacerbates the growth of a highly distorted perovskite structure. Additionally, recent electron and neutron diffraction data have cast doubt over the purported non-centrosymmetry of the $BiMnO_3$ crystal structure[34] and centrosymmetric structures have also been predicted using density functional theory calculations[35]. Since a non-centrosymmetric crystal

[1] E-printed with permission from Hyoungjeen Jeen, Guneeta Singh-Bhalla, Patrick R. Mickel, Kristin Voigt, Chelsey Morien, Sefaattin Tongay, A. F. Hebard, and Amlan Biswas, J. Appl. Phys. **109**, 074104 (2011). Copyright 2011, The American Institute of Physics.

structure is essential for ferroelectricity, the observed ferroelectric behavior of $BiMnO_3$ may be due to strain and/or ordered oxygen vacancies.[112, 113]

6.1 Optimization of BMO

$BiMnO_3$ (BMO) has a distorted perovskite-type structure with a = c = 3.935 Å(α = γ = 91.4°) and b = 3.989 Å(β = 91°).[114] Figure 6-1 shows the larger monoclinic unit cell of BMO viewed from different directions [37]; we have used the monoclinic notation to index the x-ray diffraction data of our thin films. Since cubic $SrTiO_3$ (STO) and tetragonal $SrLaGaO_4$ (SLGO) have a lattice parameter of 3.905 Åand 3.844 Årespectively, BMO grows with an (111) orientation on STO (001) and SLGO (001) substrates under a compressive strain due to a lattice mismatch of 1.14% and 2.68% respectively. It is still unclear whether this strain is responsible for the difference in the magnetic and electrical properties between thin films and polycrystalline BMO. A saturation magnetization M_{sat} of about 3.6 μ_B/Mn at 5 K and a ferromagnetic Curie temperature (T_C) of 105 K has been observed in polycrystalline BMO along with an electric remnant polarization of 62 nC/cm^2 at 87 K, while in thin films an M_{sat} of about 2.2 μ_B/Mn and a T_C of about 100 K has been reported.[33, 109, 114, 115] $P-E$ measurements on BMO thin films have been reported occasionally, and a remnant polarization of about 16 μC/cm^2 has been observed.[111] The strain may also influence the ferroelectric domain wall motion which coupled with the low resistance of the thin films have made it a challenge to confirm the FE nature of BMO thin films leading to the controversial situation presented in the introduction. To address such issues, we have optimized the growth of BMO thin films on STO and SLGO. We have obtained stoichiometric, epitaxial thin films of BMO on STO which have a high resistivity at low temperature thus facilitating the measurement of $P-E$ loops confirming the multiferroic nature of our films.

The BMO thin films were grown using pulsed laser deposition (PLD). An off-stoichiometric (Bi-rich) target with composition $Bi_{2.4}MnO_3$ was ablated using a KrF excimer laser (λ = 248 nm). The high Bi content of the target allowed us to use relatively high substrate

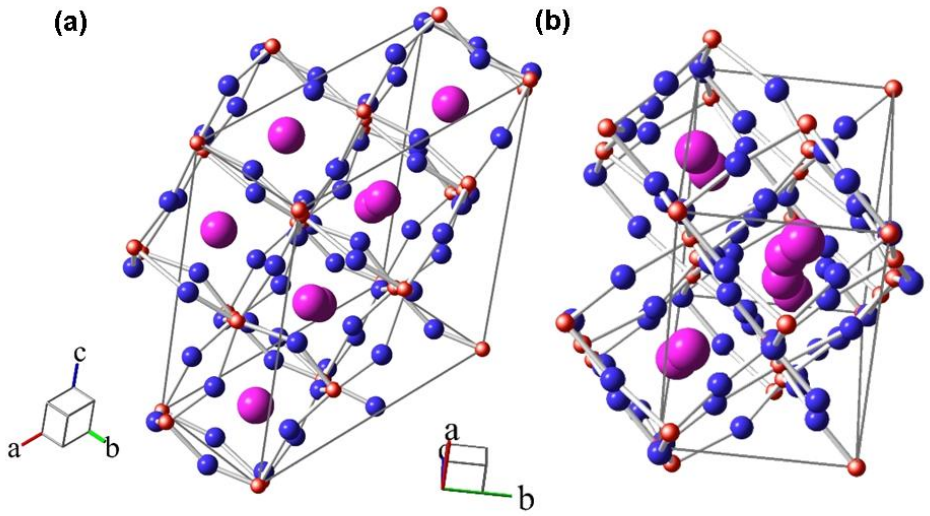

Figure 6-1. The monoclinic unit cell of $BiMnO_3$ viewed (a) along (111) direction and (b) along $(20\bar{3})$ direction.

temperatures (T_s) and still get the right Bi content for stoichiometric BMO films. The film quality was extremely sensitive to the cooling rate, still sensitive to the T_s and the oxygen pressure, while it was independent of the growth rate within the range used. The laser energy density was kept at 1.0 $\pm$ 0.2 J/cm^2. The optimum flowing oxygen pressure and T_s were 35 mTorr and 634°C, respectively. The deposition rate was 0.05 nm/s. The films were cooled in an O_2 atmosphere of 680 Torr at a rate of 20°C/min and higher (up to 40°C/min). Here, we present results from one 60 nm-thick BMO thin films. We obtained similar results from the other thin films in the thickness range of 30 nm to 60 nm.

Figure 6-2 (a) shows the x-ray diffraction data for 60-nm-thick BMO thin films grown under fixed oxygen pressure (about 40 mTorr) but different temperature. The inset shows that the BMO mainly grows with a (111) orientation. We also find other BMO peaks corresponding to other orientations than (111) BMO as well as small peak corresponding to Mn_2O_3 impurities. Especially, $(20\bar{3})$ orientation of BMO as expected from the structure of BMO at 2θ = 28.76 degrees, since it is another face in perovskite

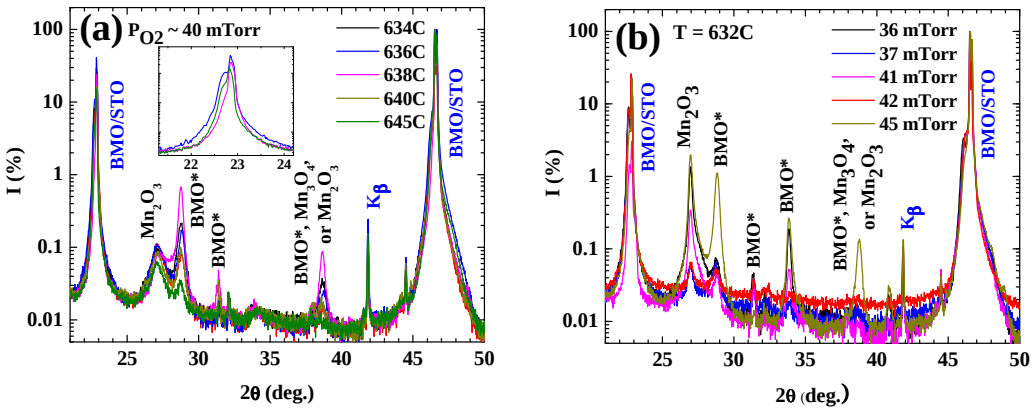

Figure 6-2. $\theta - 2\theta$ diffraction patterns of $BiMnO_3$ thin films on $SrTiO_3$. (a) Temperature effects on diffraction patterns of BMO in fixed pressure (about 40 mTorr). The inset shows the BMO (111) peak in detail. (b) Oxygen pressure effects on diffraction patterns of BMO in fixed temperature (632°C).

unit cell(Figure 6-1 and Figure 6-2). We find (111) BMO peak gets smaller T_s above 638°C, while other peaks still exist. Also, we do not find out consistent change of each peak. Figure 6-2 (b) shows the x-ray diffraction data for 60-nm-thick BMO thin films grown under fixed temperature (about 632°C) but different oxygen pressures. In all oxygen pressure we used, multiple orientation peaks and impurity peak exist. Higher oxygen pressure (45 mTorr) lowered sample quality. We still do not find any consistent change in peaks due to oxygen pressures. To remove these impurities, we increased the post-deposition rate of T_s up to 40°C /min in an O_2 atmosphere of 680 Torr. It was reported bulk BMO can decomposed above 600°C from high temperature x-ray diffraction results [116]. Also, post annealing at 460°C in 200 Torr after low temperature deposition preserves Bi content and crystallize BMO [117]. Figure 6-3 (a) shows the x-ray data for 60-nm-thick films grown using different cooling rates, which confirm that the impurity peaks have been successfully removed using the modified growth condition. The inconsistent change of relative peak intensities in Figure 6-2 can be explained by Bi re-evaporation after deposition. Rapid quenching technique is the best way among three parameters, *viz.* temperature, oxygen pressure, and cooling rate to remove Mn_2O_3

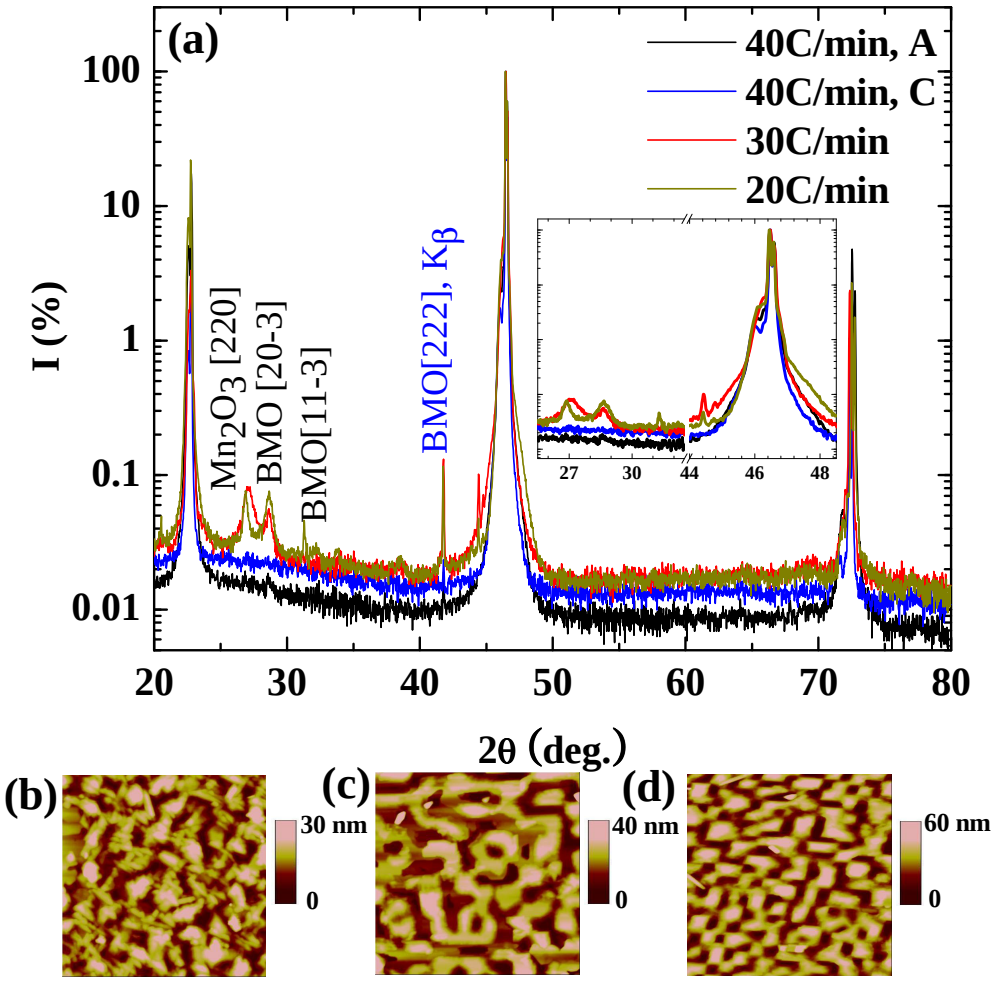

Figure 6-3. (a) $\theta - 2\theta$ diffraction patterns of BMO thin films on STO in different cooling rate. The inset shows impurity peaks and (222) BMO. 2 μm by 2 μm AFM images of the surface of BMO cooled in (b) 20°C /min, (c) 30°C /min, and (d) 40°C /min.

impurity phase and stabilize (111) orientation of BMO along out-of-plane direction. Figure 6-3 (b) - (d) shows the surface morphology of samples with different cooling rates. The surface roughness gets worse in this fast cooling. The r.m.s. roughness of samples is 4.7 nm for 20°C /min, 5.5 nm for 30°C /min, and 7.85 nm for 40°C /min. All the thin films show 3-D island growth mode with different r.m.s. roughness.

The chemical properties of the films were characterized with Auger electron spectroscopy (AES) using a Perkin-Elmer PHI 660 scanning Auger multiprobe instrument. To confirm the stoichiometry of the samples we performed Auger electron

spectroscopy (AES) measurements at 300K in ultra high vacuum (UHV) conditions. Derivative AES surface spectra were taken using 5 keV primary electron beam from kinetic energies of 50 eV to 1500 eV at incident angles from 30° to 60°. Depth profiling was performed by taking surface spectra with the parameters given above followed by an *in-situ* repeated 3 keV Ar-ion sputtering. Surface spectra of the BMO films displayed three manganese (Mn) peaks located at 548 eV, 595 eV, 645 eV, two bismuth (Bi) peaks at 106 eV, 254 eV and one oxygen (O) peak at 518 eV together with residue carbon (C) peak at 273 eV with concentrations less than 1%. After six seconds of Ar sputtering on the surface, the C peak disappeared and Bi, Mn and O concentrations are found to be 23.3%, 24.1% and 52.6% respectively with about a 2% error. These concentrations imply that the BMO stoichiometry is consistent with the measured BMO x-ray peaks from $\theta - 2\theta$ measurements. Moreover, the sensitivity factor for oxygen is based on an MgO matrix and since there is no matrix parameter in the atomic percentage calculations, this could account for the slightly lower than stoichiometric oxygen concentrations.

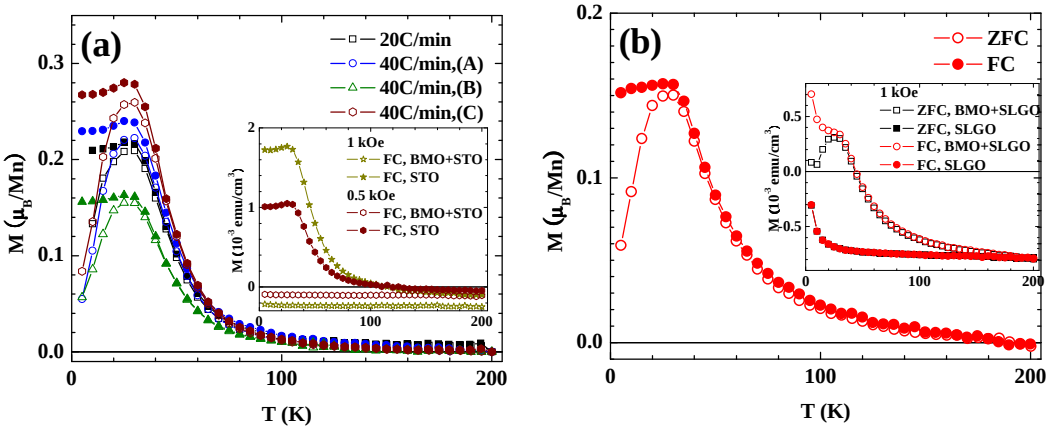

Figure 6-4. (a) Magnetization as a function of temperature (M - T) plot for BMO thin films on STO in an in-plane field of 500 Oe. The inset shows raw M - T of the films and bare STO. The full symbols and open symbols are the zero field cooled and field cooled data respectively. (b) M - T plot for BMO thin films on $SrLaGaO_4$ in an in-plane field of 1000 Oe. The inset shows raw M - T of the films and bare SLGO.

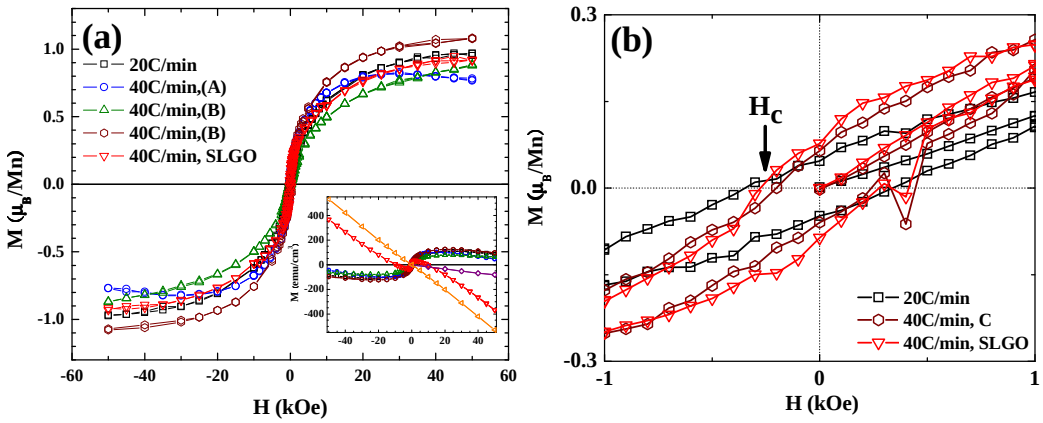

Figure 6-5. (a) Magnetization as a function of magnetic field (M - H) plot for BMO thin films on STO and SLGO at 10 K. The inset shows raw M - H of the films, bare STO, and bare SLGO. (b) Zoom of the M - T plot in low magnetic fields.

The magnetic properties of BMO are closely related to its unique crystal structure. BMO is similar to the compound $LaMnO_3$ (LMO) but due to the 6*s* lone pair the Bi ion moves away from the centrosymmetric position at the B-site of a perovskite structure. LMO is an A-type antiferromagnet due to antiferromagnetically stacked ferromagnetic layers.[118] In BMO the distortion caused by the Bi-ion leads to an FM interaction between the layers.[37, 38] Hence, BMO has an overall magnetic moment that has been measured to be as high as 3.6 μ_B/Mn in polycrystalline samples, which is close to maximum possible magnetization of 4 μ_B/Mn.[114] In thin films the magnetic moment is reduced quite likely due to the substrate induced strain. The T_C in thin films is also lower than the value of about 105 K obtained in polycrystalline samples.[38, 114] Figure 6-4 and 6-5 show the $M - T$ and $M - H$ curves of 60-nm-thick BMO thin films. The magnetic field was applied in the plane of the film for the magnetic measurements. The $M - T$ plot reveals a T_C of about 85 $\pm$ 5 K. A saturation magnetization of about 1 μ_B/Mn is obtained at 10 K in a field of 50 kOe. Figure 6-5 (b) shows the hysteresis in the $M - H$ plot and a coercive field of about 300 Oe. The hysteresis of the M - H curves and the magnetic moment become negligible at about 80 K which is closed to the estimated T_C, confirming that the observed magnetization is associated with magnetic ordering which

happens at a temperature lower than the corresponding T_C of bulk BMO [33] (data not shown). The reduced magnetic moment of our thin films compared to bulk BMO is not due to the presence of the non-magnetic impurities since all the samples have similar saturation magnetization and coercive fields (Figure 6-5). It is noted magnetic properties are very sensitive to oxygen stoichiometry. Sundaresan *et al.* suggested stoichiometric BMO is orthormbic and canted antiferromagnetic. It is going to antiferromagnetic below 30 K [39]. However, Belik *et al.* showed oxygen deficient BMO is hard to be grown by direct high pressure and high temperature method. Their stochiometric BMO is monoclinic and ferromagnetic [42]. Based on the magnetization results from the reports, our thin film is stoichiometric or slightly oxygen rich (less than 5%) [39, 42]. Since the structure of BMO is closely related to that of antiferromagnetic LMO, the non-uniform strain distribution could be responsible for both the reduced values of T_C and saturation magnetization. It has been shown that 3-D island growth leads to non-uniform strain resulting in high values of strains at the island edges [51, 119].

We also measured the electrical polarization using an interdigital capacitance geometry and a Precision LC ferroelectric tester from Radiant Technologies. A low leakage current and hence high resistivity is a requirement for polarization vs. electric field ($P - E$) measurements in BMO thin films. Our optimized thin films have a room temperature resistivity of about 10 Ω-cm, which is lower than values reported by other groups.[15, 110] However, by 140 K (below 140 K the resistance is too high to measure with our instrumentation) the resistivity increases to about 1 MΩ-cm and it was possible to make direct polarization vs. electric field ($P - E$) measurements at temperatures below 100 K using an interdigital capacitance geometry (Figure 6-6 (a)). The capacitor is composed of alternating $V+/V-$ electrodes uniformly spaced on the film surface (Figure 6-6 (b)). This structure leads to equipotential planes intersecting the film between each pair of electrodes, resulting in a capacitance between the projected areas of each electrode within the film. The projected areas were calculated using conformal

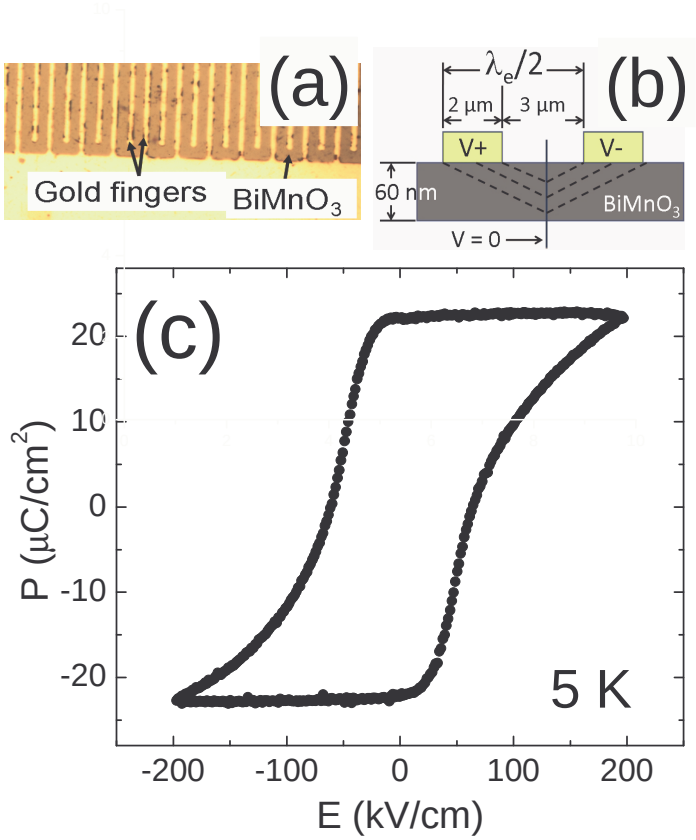

Figure 6-6. (a) The interdigital capacitance geometry deposited on the film surface. (b) Schematic of the electrode configuration for the $P-E$ measurements. (c) Remnant polarization vs. electric field ($P-E$) data of a 60 nm-thick BMO thin film on STO taken at 5 K.

mapping and equating the capacitor thickness to half the electrode spatial wavelength (λ_e = 10μm).[120] Figure 6-6 (c) shows the remnant hysteresis loop for sample with 20°C/min. at 5 K (similar results were obtained for the sample with 40°C/min.). The polarization in a hysteresis loop is calculated by integrating the total transferred charge during application of a bipolar triangular voltage waveform. This polarization includes contributions from leakage current, capacitance and ferroelectric domain switching. The polarization in the remnant hysteresis loop is calculated by isolating the transferred charge from only the domain-switching. This is done by subtracting two hysteresis loops that are preceded by poling pulses. In one loop, all of the domains are pre-switched so that no domain-switching charge is transferred during the loop, and in the other loop all the domains are set unswitched with charge transfer from domain-switching beginning

at the coercive field. The leakage current and capacitance contributions from the two loops cancel, leaving only transferred charge from domain-switching, or equivalently, the remnant charge. Dividing the remnant charge by the projected area we find a remnant polarization of $P \approx 23$ μC/cm^2 at 5K, with a coercive field $E_C \approx 60$ kV/cm.

The clear observation of a ferroelectric $P - E$ loop in BMO on STO appears to be in conflict with the centrosymmetric structure suggested by Belik *et al.*.[34] If the crystal structure of BMO is indeed centrosymmetric, then the possible reasons for the ferroelectric behavior of BMO thin films are: (1) structural distortions due to oxygen vacancies,[34] (2) a centrosymmetric to non-centrosymmetric transition below T_C i.e. below 100 K,[34] and (3) substrate induced strain.[112] Although, the AES measurements on our thin films reveal an oxygen deficiency which could lead to the ferroelectric behavior, we cannot rule out the role of substrate induced strain. If the film is uniformly strained, the lattice mismatch which is -1.14% (compressive), is not enough to break the centrosymmetry as shown by Hatt *et al.*.[112] However, it has been shown that compressive lattice mismatch strain could lead to a non-unifrom strain distribution in the thin film due to island formation and the strain at the island edges could far exceed the average lattice mismatch strain.[51, 119] The growth morphology of our thin films (inset Figure 6-3(b)-(d)) suggests that such non-uniform strain distribution is also a possible mechanism for the appearance of ferroelectricity. In addition, since we measured the $P - E$ loops upto 85 K, the ferroelectric behavior could be due to a structural change below T_C.

6.2 Structural Study

Here, we performed detailed structural study of BMO thin films on STO and SLGO. In previous section, we showed growth of impurity-free BMO thin films. High resolution x-ray diffraction technique can elucidate structural relation of BMO thin films and substrates in detail. First, we performed $\theta - 2\theta$ X-ray diffraction and grazing incidence x-ray diffraction (GIXD) of a 60-nm-thick BMO thin film on STO (Figure 6-7). We find

(111) BMO orientation and confirm negligible impurity phases. Also, $\omega - 2\theta$ rocking curve has been performed about (111) BMO peak. Due to rough surface, we could not find oscillation around BMO peak. Also, we observed shoulder peak in between BMO peak and STO peak. We measured several rocking curves of bare STO substrate, this shoulder peak is not from BMO but from STO substrates, which may be due to imperfection of commercially available STO substrates.

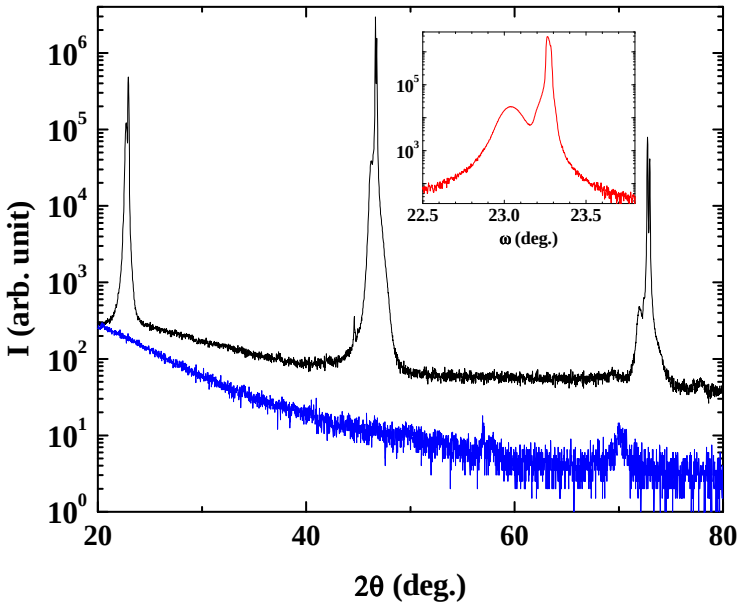

Figure 6-7. $\theta - 2\theta$ diffraction pattern and GIXD of a BMO thin film on STO. Inset: ω scan of (111) BMO peak.

To show in-plane relationship between the thin film and the substrate, we create pole figures of BMO and STO. 2θ angle is fixed at 57.78° degrees corresponding to (211) STO, and ψ angle is 65° - 70°. We observed two sets of eight peaks: $\{211\}$ and $\{121\}$. Pole figure for (110) BMO (cubic notation) showed four distinct peaks (2θ = 32° and ψ = 45° (Figure 6-8 (a)). It is noted ψ value is 0° right in center and 90° at the edge of the circles. Since $\{110\}$ BMO peaks fall in between $\{121\}$ and $\{211\}$ peaks. We conclude our BMO thin films grown on STO with a cube-on-cube orientation. We also performed mesh scan at around (113) STO (2θ = 81.03°) (Figure 6-8 (b)). The result indicates BMO and STO has matched lattice constant along in-plane, while BMO

is elongated in out-of-plane direction. This mesh scan shows epitaxial relationship between BMO and STO. Ratio of in-plane lattice constant to out-of-plane lattice constant shows about 1% elongation along out-of-plane. However, in theory, this ratio should be about 4%, if the volume of unit cell is conserved. This indicates volume may not be conserved under compressive strain.

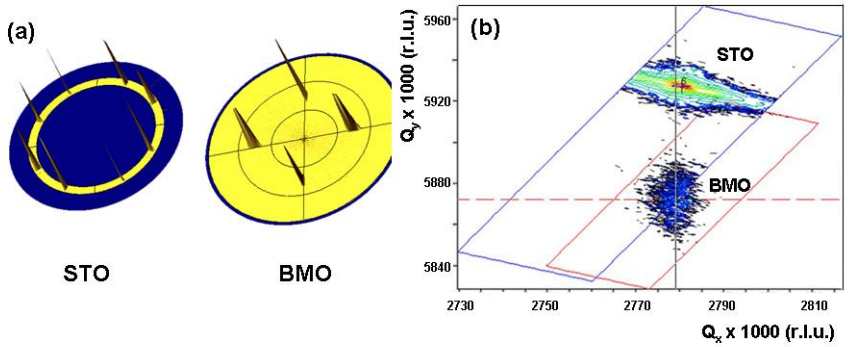

Figure 6-8. (a) Pole figure of $\{211\}$ STO and $\{110\}$ BMO (b) Reciprocal space map of the BMO thin film on STO.

To confirm thickness of our thin films, x-ray reflectivity (XRR) measurements were performed (Figure 6-9). A BMO thin film on SLGO showed oscillations corresponding to about 60 nm. This oscillation indicates the BMO thin film on SLGO has lower surface roughness. Actually inset of Figure 6-9 shows the BMO thin film on SLGO has lower roughness.

We measured $\theta - 2\theta$ diffraction showing distinct BMO peaks in a BMO thin film on SLGO (Figure 6-10). GIXD also showed negligible impurity phase. We also performed ϕ scans of SLGO (105) (2θ = 42.68°) and BMO (113) peaks. Those show two neighboring peaks are 45° away each other, which indicate cube on square growth mode. It is noted width of BMO peak are wide. It indicated in-plane mosaicity on the BMO thin film on SLGO with ω scan.

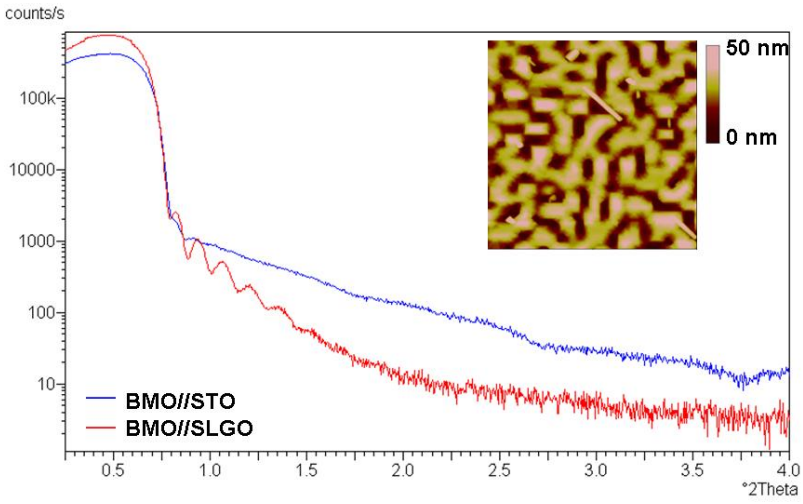

Figure 6-9. X-ray reflectivity of BMO thin films on SLGO and STO. Inset: An AFM image of the BMO on SLGO.

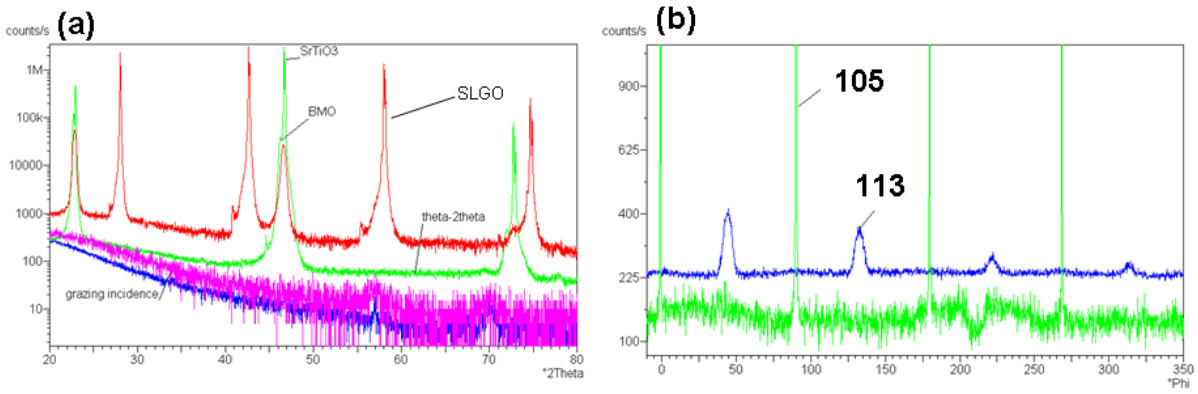

Figure 6-10. (a) $\theta - 2\theta$ patterns (red) and GIXD (magenta) of a BMO thin film on SLGO are shown. Also, $\theta - 2\theta$ patterns (green) and GIXD (blue) of a BMO thin film on STO are shown. (b) ϕ-scan of BMO (113) and SLGO (105).

6.3 Magnetoelectric Effects

BMO is multiferroic. However, it is predicted low magnetoelectric coupling [16, 17]. Here, we used interdigital electrodes to apply in-plane electric fields (up to 50 kV/cm for 100 V). We used conventional photolithography to put the electrode pattern on BMO thin films. We sputtered 50-nm-thick Pd-Au on BMO thin films. We used lift-off to removed region. This pattern consists of two different distant electrodes: 20 μm and 90 μm. We used 5 T SQUID magnetometer in B20, NPB with an electric field probe. This electric

probe has electric ports at both ends by putting connecting electrical connection from sample to a port and from other port to source meter. We put 1 MΩ standard resistor in series at outside of SQUID machine, so that we can avoid possible damage due to "burst of current" [2] (Figure 2-4).

To measure change of magnetization under electric fields, we applied 1 kOe of magnetic fields. We measured magnetization as a function of temperature (M(T)) of a BMO thin film with 30 V and -30 V respectively. We expect 15 kV/cm in the shorter electrodes and about - 3 kV/cm in the longer electrodes by apply 30 V. Before each measurement, we ran a degauss sequence at 150 K. Electric fields were applied below 145 K for 30 V case. Current in circuit was monitored and used to calculate resistance in the BMO film. Resistance could not be measured below 90 K and current went to 0 A. Here, we only discuss about results below 90 K in order to avoid possible artifact due to leakage current [121]. Difference (M_{30V} - M_{-30V}) between two M(T) curves shows linear decrease of magnetization down to low temperature. We observed a change of sign in the difference at around 60 K. When we normalized this difference to average of two magnetic moments (ratio$(\%) = \frac{100\times(M_{30V}-M_{-30V})}{0.5\times(M_{30V}-M_{-30V})}$), we observed decrease of the ratio down to about 60 K. Blow 60 K, we got constant negative. This is consistent with disappearance of magnetoelectric effects from ferroelectric measurements [122]. The system is under freezing below 50 K, so that magnetoelectric effect is reduced below 50 K from electric polarization measurement under magnetic fields.

6.4 Summary

First, we have grown thin films of epitaxial $BiMnO_3$ (111) on $SrTiO_3$ (001) substrates. The films have the in-plane alignment and stoichiometry. The ferromagnetic T_C is 85±5 K with a saturation magnetization of about 1 μ_B/Mn at 10 K. A remnant polarization of 23 μC/cm^2 was measured at 5 K with a coercive field of 60 kV/cm. Non-uniform strain distribution may be responsible for the appearance of ferroelectricity in these BMO thin films. Second, we also grow $BiMnO_3$ (111) on SLGO (001) substrates. These

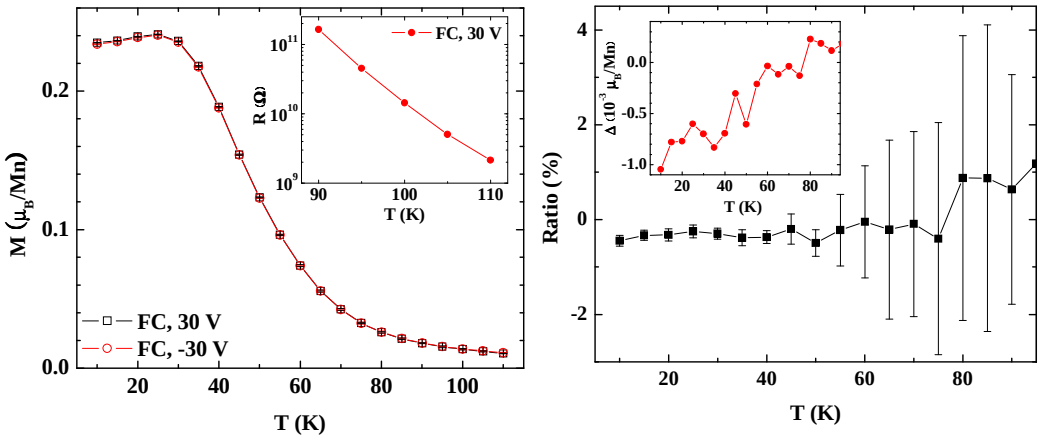

Figure 6-11. (a) Magnetic moments as a function of temperature (M(T)) under electric fields ($\pm$30 V) of a BMO thin film on STO. Inset: Resistances a function of temperature (R(T))under 30 V. (b) The ratio of difference in magnetic moments to average magnetic moments as a function of temperature. Inset: The difference of magnetic moments under $\pm$30 V

films show clear ferromagnetism, however, high resolution XRD results indicate this $BiMnO_3$ film has mosaicity. This could be the origin of disappearance of ferroelectricity due to possible strain relaxation and randomly orientated spontaneous polarization. Third, we observed magnetoelectric effects in a BMO thin film on STO with interdigital electrodes. This effect is small but show clear decrease down to 60 K. Below 60 K, The effect is saturated, which is slightly different results from P(E) measurements under high magnetic fields.

CHAPTER 7
CONCLUSION AND FUTURE WORK

Atomically flat hole doped manganite thin films, especially $(La_{1-y}Pr_y)_{1-x}Ca_xMnO_3$ (LPCMO) thin films have been successfully grown. AFM and XRD data show that in optimal oxygen pressure, LPCMO thin films follow step flow growth mode and are epitaxial. EDX in TEM and high angle annular dark field (HAADF) imaging have confirmed clear interface between substrate and LPCMO thin films. High resolution Z-contrast lattice images could not be achieved due to high electron noise. Z-contrast lattice images will give more clear information of our LPCMO thin films such as interface sharpness, structural perfection and chemical homogeneity [43].

Single domain to multi-domain transition in LPCMO has also been confirmed in thin film form. However, the temperature range of the transition to double domain from single domain is wider than the case in bulk samples. The strong in-plane anisotropy in the phase separated material may be the origin of this transition. Peak in coercive field map is shifted to higher temperature in thicker films, which suggests critical single domain radius is smaller in the thicker films.

Anisotropic transport properties under high electric fields in LPCMO thin films show that CER effect originates due to dielectrophoresis. Magnetization measurements under electric fields (about 0.5 kV/cm) do not show clear evidence of change in magnetization. Magnetization measurement of arrayed LPCMO thin films in high electric fields will be an interesting experiment to confirm our finding and be performed in the near future.

The combined effect of electric and magnetic fields on magnetotransport properties in LPCMO thin films were also investigated. We observed that high currents (5 μA) can decrease resistance below T_{IM} in the presence of a magnetic field, which clearly indicates current effects on magnetoresistance (MR). This current effects in the SPS region indicates tunneling process across insulating phases is more active under high currents. Also, in this low temperature region, we observed anisotropic

magnetoelectric resistance (MER) due to substrate strains. In thicker films, magnetic anisotropy is lowered. This strain field dependent MER is a unique version of the magnetoelectric effect at the interface of phase separated manganites. The difference in magnitude of $AMR_{\perp}^{OUT}$ suggests more drastic changes along magnetic easy axis, where LPCMO experiences higher tensile strain. Angle dependent magnetotransport measurements will help to understand this anisotropic AMR and electric field effect on magnetotransport.

Impurity-free and epitaxial $BiMnO_3$ thin films were successfully grown and characterized using various techniques. Magnetization data showed clear ferromagnetism below about 85 K. The highest magnetization at 10 K was about 1 μ_B/Mn. Ferroelectricity was also observed in the low temperature range with a saturation polarization of 23 $\mu C/cm^2$ at 5 K. The ferroelectric hysteresis loop closed at around 85 K. The similar critical temperatures for ferromagnetism and ferroelectricity suggests a coupling of the two order parameters. We are currently optimizing the thin films to lower the surface roughness through the following steps: In-situ post-annealing, adjustment of set-temperature for fast cooling (increase from 475°C), and immediate start of fast cooling. In order to reduce oxygen content in BMO, it is possible that fast cooling without oxygen quenching may be necessary.

REFERENCES

[1] S. Jin, T. H. Tiefel, M. McCormack, R. A. Fastnacht, R. Ramesh, and L. H. Chen, Science **264**, 413 (1994).

[2] A. Asamitsu, Y. Tomioka, H. Kuwahara, and Y. Tokura, Nature **388**, 50 (1997).

[3] T. Dhakal, J. Tosado, and A. Biswas, Phys. Rev. B **75**, 092404 (2007).

[4] K. Miyano, T. Tanaka, Y. Tomioka, and Y. Tokura, Phys. Rev. Lett. **78**, 4257 (1997).

[5] J. Tosado, T. Dhakal, and A. Biswas, J. Phys.: Condens. Mat. **21**, 192203 (2009).

[6] K. H. Ahn, T. Lookman, and A. R. Bishop, Nature **428**, 401 (2004).

[7] H. T. Yi, T. Choi, and S. W. Cheong, Appl. Phys. Lett. **95**, 063509 (2009).

[8] H. Jeen and A. Biswas, Phys. Rev. B **83**, 064408 (2011).

[9] M. Fiebig, J. Phys. D: Appl. Phys. **38**, R123 (2005).

[10] N. A. Spaldin and M. Fiebig, Science **309**, 391 (2005).

[11] R. Ramesh and N. A. Spaldin, Nat. Mater. **6**, 21 (2007).

[12] M. Gajek, M. Bibes, S. Fusil, K. Bouzehouane, J. Fontcuberta, A. Barthelemy, and A. Fert, Nat. Mater. **6**, 296 (2007).

[13] C. N. R. Rao and C. R. Serrao, J. Mater. Chem. **17**, 4931 (2007).

[14] W. Prellier, M. P. Singh, and P. Murugavel, J. Phys.: Condens. Mat. **17**, R803 (2005).

[15] W. Eerenstein, N. D. Mathur, and J. F. Scott, Nature **442**, 759 (2006).

[16] T. Kimura, S. Kawamoto, I. Yamada, M. Azuma, M. Takano, and Y. Tokura, Phys. Rev. B **67**, 180401 (2003).

[17] S.-W. Cheong and M. Mostovoy, Nat Mater **6**, 13 (2007).

[18] T. C. Ozawa and S. J. Kang, J. Appl. Cryst. **37**, 679 (2004).

[19] P. Schiffer, A. P. Ramirez, W. Bao, and S.-W. Cheong, Phys. Rev. Lett. **75**, 3336 (1995).

[20] C. Zener, Phys. Rev. **82**, 403 (1951).

[21] M. B. Salamon and M. Jaime, Rev. Mod. Phys. **73**, 583 (2001).

[22] C. Kittel, *Introduction to Solid State Physics* (Wiley, New York, NY, 1995).

[23] M. Ziese and C. Srinitiwarawong, Phys. Rev. B **58**, 11519 (Nov 1998).

[24] J. M. D. Coey, M. Viret, L. Ranno, and K. Ounadjela, Phys. Rev. Lett. **75**, 3910 (1995).

[25] M. Uehara, S. Mori, C. H. Chen, and S. W. Cheong, Nature **399**, 560 (1999).

[26] L. Zhang, C. Israel, A. Biswas, R. L. Greene, and A. de Lozanne, Science **298**, 805 (2002).

[27] Y. Murakami, H. Kasai, J. J. Kim, S. Mamishin, D. Shindo, S. Mori, and A. Tonomura, Nat. Nanotechnol. **5**, 37 (2010).

[28] A. Moreo, M. Mayr, A. Feiguin, S. Yunoki, and E. Dagotto, Phys. Rev. Lett. **84**, 5568 (2000).

[29] G. Wachtel, D. Orgad, and D. I. Golosov, Phys. Rev. B **78**, 184433 (2008).

[30] A. J. Millis, P. B. Littlewood, and B. I. Shraiman, Phys. Rev. Lett. **74**, 5144 (1995).

[31] H. Schmid, Ferroelectrics **162**, 317 (1994).

[32] N. A. Hill and K. M. Rabe, Phys. Rev. B **59**, 8759 (1999).

[33] A. M. dos Santos, S. Parashar, A. R. Raju, Y. S. Zhao, A. K. Cheetham, and C. N. R. Rao, Solid State Commun. **122**, 49 (2002).

[34] A. A. Belik, S. Iikubo, T. Yokosawa, K. Kodama, N. Igawa, S. Shamoto, M. Azuma, M. Takano, K. Kimoto, Y. Matsui, and E. Takayama-Muromachi, J. Am. Chem. Soc. **129**, 971 (2007).

[35] P. Baettig, R. Seshadri, and N. A. Spaldin, J. Am. Chem. Soc. **129**, 9854 (2007).

[36] I. V. Solovyev and Z. V. Pchelkina, New J. Phys. **10**, 073021 (2008).

[37] T. Atou, H. Chiba, K. Ohoyama, Y. Yamaguchi, and Y. Syono, J. Solid State Chem. **145**, 639 (1999).

[38] A. M. dos Santos, A. K. Cheetham, T. Atou, Y. Syono, Y. Yamaguchi, K. Ohoyama, H. Chiba, and C. N. R. Rao, Phys. Rev. B **66**, 064425 (2002).

[39] A. Sundaresan, R. V. K. Mangalam, A. Iyo, Y. Tanaka, and C. N. R. Rao, J. Mater. Chem. **18**, 2191 (2008).

[40] E. Ohshima, Y. Saya, M. Nantoh, and M. Kawai, Solid State Commun. **116**, 73 (2000).

[41] D. P. Kozlenko, A. A. Belik, S. E. Kichanov, I. Mirebeau, D. V. Sheptyakov, T. Strässle, O. L. Makarova, A. V. Belushkin, B. N. Savenko, and E. Takayama-Muromachi, Phys. Rev. B **82**, 014401 (2010).

[42] A. A. Belik, T. Kolodiazhnyi, K. Kosuda, and E. Takayama-Muromachi, J. Mater. Chem. **19**, 1593 (2009).

[43] J. H. Lee, L. Fang, E. Vlahos, X. Ke, Y. W. Jung, L. F. Kourkoutis, J.-W. Kim, P. J. Ryan, T. Heeg, M. Roeckerath, V. Goian, M. Bernhagen, R. Uecker, P. C. Hammel, K. M. Rabe, S. Kamba, J. Schubert, J. W. Freeland, D. A. Muller, C. J. Fennie, P. Schiffer, V. Gopalan, E. Johnston-Halperin, and D. G. Schlom, Nature **466**, 954 (2010).

[44] V. Leca, Ph.D. thesis, University of Twente (2003).

[45] K. M. Rabe, C. H. Ahn, and J.-M. Triscone, *Physics of Ferroelectrics: A Modern Perspective* (Springer, Berlin, 2007).

[46] M. Kareev, S. Prosandeev, J. Liu, C. Gan, A. Kareev, J. W. Freeland, M. Xiao, and J. Chakhalian, Appl. Phys. Lett. **93**, 061909 (2008).

[47] G. Koster, B. L. Kropman, G. J. H. M. Rijnders, D. H. A. Blank, and H. Rogalla, Appl. Phys. Lett. **73**, 2920 (1998).

[48] T. Venkatesan, X. D. Wu, A. Inam, and J. B. Wachtman, Appl. Phys. Lett. **52**, 1193 (1988).

[49] *Nanotechnology measurement handbook* (Keithley, Cleveland, OH, 2007).

[50] S. H. Yun, T. Dhakal, D. Goswami, G. Singh, A. Herbard, and A. Biswas, J. Appl. Phys. **103**, 07E317 (2008).

[51] A. Biswas, M. Rajeswari, R. C. Srivastava, Y. H. Li, T. Venkatesan, R. L. Greene, and A. J. Millis, Phys. Rev. B **61**, 9665 (2000).

[52] Y. Suzuki, H. Y. Hwang, S.-W. Cheong, T. Siegrist, R. B. van Dover, A. Asamitsu, and Y. Tokura, J. Appl. Phys. **83**, 7064 (1998).

[53] T. Z. Ward, J. D. Budai, Z. Gai, J. Z. Tischler, L. Yin, and J. Shen, Nat. Phys. **5**, 885 (2009).

[54] W. S. Choi, Z. Marton, S. Y. Jang, S. J. Moon, B. C. Jeon, J. H. Shin, S. S. A. Seo, T. W. Noh, K. Myung-Whun, H. N. Lee, and Y. S. Lee, J. Phys. D: Appl. Phys. **42**, 165401 (2009).

[55] W. Prellier, P. Lecoeur, and B. Mercey, J. Phys.: Condens. Matter **13**, R915 (2001).

[56] Z. Marton, S. S. A. Seo, T. Egami, and H. N. Lee, J. Cryst. Growth **312**, 2923 (2010).

[57] H. Boschker, M. Mathews, E. P. Houwman, H. Nishikawa, A. Vailionis, G. Koster, G. Rijnders, and D. H. A. Blank, Phys. Rev. B **79**, 214425 (2009).

[58] A. Bhattacharya, S. J. May, S. G. E. te Velthuis, M. Warusawithana, X. Zhai, B. Jiang, J.-M. Zuo, M. R. Fitzsimmons, S. D. Bader, and J. N. Eckstein, Phys. Rev. Lett. **100**, 257203 (2008).

[59] H. L. Ju, J. Gopalakrishnan, J. L. Peng, Q. Li, G. C. Xiong, T. Venkatesan, and R. L. Greene, Phys. Rev. B **51**, 6143 (1995).

[60] W. Prellier, M. Rajeswari, T. Venkatesan, and R. L. Greene, Appl. Phys. Lett. **75**, 1446 (1999).

[61] H. M. Christen and G. Eres, J. Phys.: Condens. Matter **20**, 264005 (2008).

[62] A. Urushibara, Y. Moritomo, T. Arima, A. Asamitsu, G. Kido, and Y. Tokura, Phys. Rev. B **51**, 14103 (1995).

[63] P. Orgiani, R. Ciancio, A. Galdi, S. Amoruso, and L. Maritato, Appl. Phys. Lett. **96**, 032501 (2010).

[64] H. Y. Hwang, S.-W. Cheong, N. P. Ong, and B. Batlogg, Phys. Rev. Lett. **77**, 2041 (1996).

[65] T. Taniyama, M. Yamasaki, and Y. Yamazaki, Appl. Phys. Lett. **81**, 4562 (2002).

[66] A. Goyal, M. Rajeswari, R. Shreekala, S. E. Lofland, S. M. Bhagat, T. Boettcher, C. Kwon, R. Ramesh, and T. Venkatesan, Appl. Phys. Lett. **71**, 2535 (1997).

[67] N. D. Mathur, M. H. Jo, J. E. Evetts, and M. G. Blamire, J. Appl. Phys. **89**, 3388 (2001).

[68] For thickness measurement, the thin films were partially dipped in the etching solution (H_2O + KI + 10% HCl) for 10 - 40 seconds. And then, the step, created by etching solution, were measured with atomic force microscope.

[69] J. A. Collado, C. Frontera, J. L. Garca-Muoz, C. Ritter, M. Brunelli, and M. A. G. Aranda, Chem. Mater. **15**, 167 (2003).

[70] L. Vasylechko, L. Akselrud, W. Morgenroth, U. Bismayer, A. Matkovskii, and D. Savytskii, J. Alloys Compd. **297**, 46 (2000).

[71] P. A. Sharma, S. B. Kim, T. Y. Koo, S. Guha, and S.-W. Cheong, Phys. Rev. B **71**, 224416 (2005).

[72] T_{IM} and T_{MI} were defined as the maximum or minmum change of resistivity as a function of temperature.

[73] L. Ghivelder and F. Parisi, Phys. Rev. B **71**, 184425 (2005).

[74] With direct subtraction, the zero field cooled (ZFC) warming mangetization measurement showed a negative at low temperature. However, when the LPCMO was at near to Ferromagnetic to Paramagnetic transition, the rise and decrease of magnetic moments were observed at the same temperature.

[75] *Introduction to Magnetic Materials*, edited by B. D. Cullity and C. D. Graham (Wiley-IEEE Press, Hoboken, NJ, 2008).

[76] *Remant Fields in MPMP Superconducting Magnets*, 1014-208 (Quantum Design, San Diego, CA, 2001).

[77] E. F. Kneller and F. E. Luborsky, J. Appl. Phys. **34**, 656 (1963).

[78] R. Das, Ph.D. thesis, University of Florida (2010).

[79] R. Skomski, J. Phys.: Condens. Mat. **15**, R841 (2003).

[80] K. Binder and A. P. Young, Rev. Mod. Phys. **58**, 801 (1986).

[81] W. Wu, C. Israel, N. Hur, S. Park, S.-W. Cheong, and A. de Lozanne, Nat. Mater. **5**, 881 (2006).

[82] S. Dong, S. Yunoki, X. Zhang, C. Şen, J.-M. Liu, and E. Dagotto, Phys. Rev. B **82**, 035118 (2010).

[83] Y. Suzuki, H. Y. Hwang, S.-W. Cheong, and R. B. van Dover, Appl. Phys. Lett. **71**, 140 (1997).

[84] C. Kittel, Rev. Mod. Phys. **21**, 541 (1949).

[85] D. Givord, P. Tenaud, and T. Viadieu, IEEE T. Magn. **24**, 1921 (1988).

[86] D. Elbaz, D. Givord, S. Hirosawa, F. P. Missell, M. F. Rossignol, and V. Villas-Boas, J. Appl. Phys. **69**, 5492 (1991).

[87] E. Kondorsky, J. Phys. (USSR) **2**, 161 (1940).

[88] S. Reich, S. Shtrikman, and D. Treves, J. Appl. Phys. **36**, 140 (1965).

[89] Z.-H. Wang, G. Cristiani, and H. U. Habermeier, Appl. Phys. Lett. **82**, 3731 (2003).

[90] A. Ohtomo, D. A. Muller, J. L. Grazul, and H. Y. Hwang, Nature **419**, 378 (2002).

[91] A. Ohtomo and H. Y. Hwang, Nature **427**, 423 (2004).

[92] J. Mannhart and D. G. Schlom, Science **327**, 1607 (2010).

[93] S. Smadici, P. Abbamonte, A. Bhattacharya, X. Zhai, B. Jiang, A. Rusydi, J. N. Eckstein, S. D. Bader, and J.-M. Zuo, Phys. Rev. Lett. **99**, 196404 (2007).

[94] G. J. H. M. Rijnders, G. Koster, D. H. A. Blank, and H. Rogalla, Appl. Phys. Lett. **70**, 1888 (1997).

[95] J. Kobayashi, Y. Tazoh, and S. Miyazawa, J. Cryst. Growth **131**, 138 (1993).

[96] U. Pietsch, V. Holy, and T. Baumbach, *High-Resolution X-ray Scattering* (Springer, Berlin, 2004) p. 145.

[97] J.-S. Lee, D. A. Arena, P. Yu, C. S. Nelson, R. Fan, C. J. Kinane, S. Langridge, M. D. Rossell, R. Ramesh, and C.-C. Kao, Phys. Rev. Lett. **105**, 257204 (2010).

[98] S. Singh and M. Fitzsimmons, (private communication).

[99] G. Garbarino, C. Acha, P. Levy, T. Y. Koo, and S.-W. Cheong, Phys. Rev. B **74**, 100401 (2006).

[100] P. D. Beale and P. M. Duxbury, Phys. Rev. B **37**, 2785 (1988).

[101] S. Dong, H. Zhu, and J.-M. Liu, Phys. Rev. B **76**, 132409 (2007).

[102] Y. Tomioka, A. Asamitsu, H. Kuwahara, Y. Moritomo, and Y. Tokura, Phys. Rev. B **53**, R1689 (1996).

[103] F. Tsui, M. C. Smoak, T. K. Nath, and C. B. Eom, Appl. Phys. Lett. **76**, 2421 (2000).

[104] J. C. Jiang, E. I. Meletis, and K. I. Gnanasekar, Appl. Phys. Lett. **80**, 4831 (2002).

[105] J. Dho, Y. N. Kim, Y. S. Hwang, J. C. Kim, and N. H. Hur, Appl. Phys. Lett. **82**, 1434 (2003).

[106] M. Egilmez, M. M. Saber, A. I. Mansour, R. Ma, K. H. Chow, and J. Jung, Appl. Phys. Lett. **93**, 182505 (2008).

[107] Q. Li, H. S. Wang, Y. F. Hu, and E. Wertz, J. Appl. Phys. **87**, 5573 (2000).

[108] I. C. Infante, V. Laukhin, F. Sánchez, J. Fontcuberta, O. Melnikov, O. Y. Gorbenko, and A. R. Kaul, J. Appl. Phys. **99**, 08C502 (2006).

[109] W. Eerenstein, F. D. Morrison, J. F. Scott, and N. D. Mathur, Appl. Phys. Lett. **87**, 101906 (2005).

[110] M. Gajek, M. Bibes, A. Barthelemy, K. Bouzehouane, S. Fusil, M. Varela, J. Fontcuberta, and A. Fert, Phys. Rev. B **72**, 020406 (2005).

[111] J. Y. Son and Y.-H. Shin, Appl. Phys. Lett. **93**, 062902 (2008).

[112] A. J. Hatt and N. A. Spaldin, Eur. Phys. J. B **71**, 435 (2009).

[113] H. Yang, Z. H. Chi, J. L. Jiang, W. J. Feng, J. F. Dai, C. Q. Jin, and R. C. Yu, J. Mater. Sci. **43**, 3604 (2008).

[114] H. Chiba, T. Atou, and Y. Syono, J. Solid State Chem. **132**, 139 (1997).

[115] A. F. M. dos Santos, A. K. Cheetham, W. Tian, X. Q. Pan, Y. F. Jia, N. J. Murphy, J. Lettieri, and D. G. Schlom, Appl. Phys. Lett. **84**, 91 (2004).

[116] H. Faqir, H. Chiba, M. Kikuchi, Y. Syono, M. Mansori, P. Satre, and A. Sebaoun, J. Solid State Chem. **142**, 113 (1999).

[117] S. Havelia, S. Wang, M. Skowronski, and P. A. Salvador, J. Appl. Phys. **106**, 123509 (2009).

[118] J. B. Goodenough, Phys. Rev. **100**, 564 (1955).

[119] Y. Chen and J. Washburn, Phys. Rev. Lett. **77**, 4046 (1996).

[120] R. Igreja and C. J. Dias, Sens. Actuator A- Phys. **112**, 291 (2004).

[121] W. Eerenstein, F. D. Morrison, F. Sher, J. L. Prieto, J. P. Attfield, J. F. Scott, and N. D. Mathur, Philos. Mag. Lett. **87**, 249 (2007).

[122] P. R. Mickel and A. F. Hebard, (private communication)

BIOGRAPHICAL SKETCH

Hyoung Jeen was born in Pusan (now, Busan), South Korea as a son of Kangja Lee and Gwangsoo Jeen. Before he entered high school, he was more interested in sports, *viz.* taekwondo, basketball, and baseball. In high school, his interests got shifted to Chemistry and Physics. He was also influenced by his father, who is a Physics professor in Pusan National University (PNU). He went to PNU and majored Physics as his father did. After one year in the college, he became a drill sergeant in Korean Army Training Center for his national duty. After getting back from the duty, he had various chances to learn condensed matter physics and met excellent physicists. Then, he decided to study abroad. He got into Department of Physics, University of Florida at Fall, 2005. He luckily joined Dr. Biswas group at July, 2008. While working in his group, he has learned many things not only for science but also for life from Dr. Biswas and his students. He also met many nice colleagues and professors in the school and professional conferences, so that he can expand his knowledges.